

Transformation of Surface Oxides during Vacuum Heat Treatment of a Powder Metallurgical Hot Work Tool Steel

by

Sebastian Brust

Diploma work No. 109/2013

at Department of Materials and Manufacturing Technology
CHALMERS UNIVERSITY OF TECHNOLOGY
Gothenburg, Sweden

Diploma work in the master program Materials Engineering

Performed at: Department of Materials and Manufacturing Technology
Chalmers University of Technology, SE - 412 96 Gothenburg

Examiner and Supervisor: Assoc. Professor Eduard Hryha
Department of Materials and Manufacturing Technology
Chalmers University of Technology, SE - 412 96 Gothenburg

Transformation of Surface Oxides during Vacuum Heat Treatment of a Powder Metallurgical Hot Work Tool Steel

© Sebastian Brust, 2013.

Diploma work no 109/2013
Department of Materials and Manufacturing Technology
Chalmers University of Technology
SE-412 96 Gothenburg
Sweden

Transformation of Surface Oxides during Vacuum Heat Treatment of a Powder Metallurgical Hot Work Tool Steel

Sebastian Brust
Department of Materials and Manufacturing Technology
Chalmers University of Technology

SUMMARY

Characteristics of surface oxide in case of gas atomized Hot Work Tool Steel powder X40CrMoV5-1 in as-atomized condition and after heat treatment at different temperatures in vacuum conditions are discussed. Reduction of surface oxides on steel powder prior to consolidation is mandatory to achieve strong inter-particle connections in the final product. The efficient reduction requires knowledge concerning processes of the surface chemistry changes during heat treatment and sintering. Changes in powder surface composition was studied by X-ray Photoelectron Spectroscopy (XPS) for different temperatures after the heat treatment performed in a furnace attached to the XPS system in ultra-high vacuum (UHV). Morphology, chemistry and distribution of oxides on the powder particle surface were additionally analyzed by Scanning Electron Microscopy (SEM) combined with Energy Dispersive X Ray Analysis (EDX).

The results show the presence of a heterogeneous oxide layer on the as-received powder surface, formed by a homogeneous iron oxide layer with a thickness of ~ 7 nm and particulate oxides rich in chromium, manganese, silicon and vanadium. The iron oxide layer is almost completely reduced after heat treatment at 600 °C. However, this leads to growth of Cr-, Mn-, Si- and V-rich oxides and segregation of sulfides on the powder surface. The reduction of chromium oxides starts around 700 °C, but further enrichment in Mn, Si and V is observed. Considerable decrease in the oxygen signal was found after heat treatment at 800 °C, indicating significant reduction in oxide amount. An almost fully oxide-free powder surface was detected after heat treatment at 900 °C. Only some vanadium compounds and sulfides were still observed on the powder particle surface. The amount of sulfides increases with increasing annealing temperature. The results indicate that high temperature vacuum annealing of the X40CrMoV5-1 powder before consolidation seems to be feasible to reduce surface oxides and thus improve the inter-particle bonding between the powder particles during further consolidation.

Keywords: Hot Work Tool Steel, Surface Oxides, Powder Metallurgy, Vacuum Annealing, Surface Analysis

Contents

NOMENCLATURE.....	I
ABSTRACT.....	III
1. INTRODUCTION.....	1
2 THEORETICAL BACKGROUND	3
2.1 HOT WORK TOOL STEELS	3
2.2 POWDER METALLURGY	4
2.2.1 Steel powder production.....	4
2.2.2 Sintering and Hot Isostatic Pressing.....	6
2.3 OXIDES ON POWDER SURFACES	8
2.3.1 Thermodynamic description of oxide reduction.....	9
2.3.2 Previous investigations on X40CrMoV5-1.....	12
2.4 MATERIAL AND EXPERIMENTAL TECHNIQUES	13
2.4.1 Material and sieve analysis.....	13
2.4.2 X-ray Photoelectron Spectroscopy.....	13
2.4.3 Scanning Electron Microscopy	18
2.4.4 Thermogravimetry Analysis	20
2.4.5 Residual Gas Analysis.....	21
2.4.6 Differential Thermal Analysis	22
2.4.7 Dilatometry	23
2.4.8 Thermodynamic calculations	23
3 RESULTS.....	26
3.1 ANALYSIS OF THE AS-RECEIVED STATE	26
3.1.1 Scanning Electron Microscopy	26
3.1.2 X-ray Photoelectron Spectroscopy.....	31
3.2 ANALYSIS AFTER HEAT TREATMENT.....	42
3.2.1 Scanning Electron Microscopy	42
3.2.2 X-ray Photoelectron Spectroscopy.....	52
3.3 THERMOANALYTICAL INVESTIGATIONS.....	65
3.3.1 Thermogravimetry Analysis	65
3.3.2 Residual Gas Analysis.....	66
3.3.3 Differential Thermal Analysis	67
3.3.4 Dilatometry	68
3.3.5 Calculation of phase transformations	69
4 DISCUSSION.....	70

5	CONCLUSION AND FUTURE WORK.....	79
	REFERENCES.....	81
	APPENDIX.....	87

Nomenclature

Symbols

E_B	Characteristic binding energy	[eV]
E_K	Kinetic Energy	[eV]
G	Gibbs free energy	[J]
h	Planck constant	[Js]
K	Equilibrium constant	
p	Pressure	[mbar]
R	Universal gas constant	[J·mol ⁻¹ ·K ⁻¹]
S	Entropy	[J·K ⁻¹]
T	Temperature	[°C]
U	Internal energy	[J]
v	Specific volume	[m ³ ·kg ⁻¹]
W_s	Spectrometer work function	[J]
x	Molar fraction	
ϑ	Frequency	[s ⁻¹]
Ω	Interaction parameter	
λ	Electron inelastic mean free path	[m]

Acronyms

bcc	body-centered cubic
BE	Backscattered Electrons
CALPHAD	CALculations of PHase Diagrams
CWS	Cold Work Tool Steel
DIL	Dilatometry
DTA	Differential Thermal Analysis
DTG	Differential Thermal Gravimetry
EDX	Energy Dispersive X-ray spectroscopy
ESCA	Electron Spectroscopy for Chemical Analysis
fcc	face-centered cubic
FEG	Field Emission Gun
HIP	Hot Isostatic Pressing
HSS	High Speed Tool Steel
HWS	Hot Work Tool Steel
Wt.-%	Weight percentage
OPS	Oxide Polishing Suspension
PE	Primary Electrons
PM	Powder Metallurgy
RGA	Residual Gas Analysis
SE	Secondary Electrons
SEM	Scanning Electron Microscopy
TGA	Thermogravimetry Analysis
UHV	Ultra-High Vacuum
Vol.-%	Volume percentage
XPS	X-ray Photoelectron Spectroscopy
X32	X32CrMoCo3-3-3 (1.2885)
X40	X40CrMoV5-1 (1.2344)

Abstract

The main advantage of Powder Metallurgy (PM) compared to conventional metallurgy for tool steels is increased mechanical properties by fine dispersion of hard phases, smaller grain sizes and prevention of macro segregations. However, for Hot Work Tool Steels (HWS) toughness is a major concern as the materials are subjected to thermal shock during service. But toughness of PM steels can be reduced by thermodynamically stable oxide phases present on the powder particle surface. These oxides are formed by alloying elements with high oxygen affinity such as chromium, vanadium and manganese which can create a network of oxides in the compact.

This thesis deals with surface analysis of gas atomized HWS powder X40CrMoV5-1 after heat treatment at different temperatures in vacuum conditions. Efficient reduction of surface oxides requires knowledge concerning processes of the surface chemistry changes during heat treatment and sintering. Therefore, X-ray Photoelectron Spectroscopy (XPS) was used to analyze the changes of the surface composition for different heat treatments. The heat treatment was performed in a furnace attached to the XPS system in ultra-high vacuum (UHV) conditions. Afterwards the samples were analyzed by Scanning Electron Microscopy (SEM) combined with Energy Dispersive X Ray Analysis (EDX) to investigate morphology, chemistry and distribution of oxides on the powder particle surface. Additionally, thermoanalytical techniques were used to study the interaction with the surrounding vacuum.

The results show the presence of a heterogeneous oxide layer on the as-received powder surface, formed by a homogeneous iron oxide layer and particulate oxides rich in chromium, manganese, silicon and vanadium. The iron oxide layer is almost completely reduced after heat treatment at 700 °C. However, this leads to growth of Cr-, Mn-, Si- and V-rich oxides and segregation of sulfides on the powder surface. The reduction of chromium oxides starts around 700 °C but further enrichment in Mn, Si and V is observed. Considerable decrease in the oxygen signal was found after heat treatment at 800 °C, indicating significant reduction in oxide amount. An almost fully oxide-free powder surface was detected after heat treatment at 900 °C. Only some vanadium compounds and sulfides were observed on the powder particle surface. The amount of sulfides increases with increasing annealing temperature.

The results indicate that high temperature vacuum annealing of the X40CrMoV5-1 powder before consolidation seems to be feasible to reduce surface oxides and thus improve the metallic bonding between the powder particles during further consolidation.

1. Introduction

This thesis deals with investigations of oxide phases on a Hot Work Tool Steel (HWS) powder. HWS are basically used for the hot-forming of work pieces made of metal. For high performance applications Powder Metallurgy (PM) is often chosen as the way of production for tool steels. As it is an established way of production for Cold Work Tool Steels (CWS) and High Speed Tool Steels (HSS), it is not yet a developed method for HWS [1, 2].

The main benefits of PM for tool steels, compared to conventional metallurgy, are increased mechanical properties by fine dispersion of hard phases, smaller grain size and prevention of macro segregations [3]. However, in opposite to CWS and HSS, Hot Work tool Steels do contain very low amounts of hard phases and toughness is a major concern as the materials are subjected to thermal shock during service [4]. But toughness of PM steels can be reduced by oxide phases and further contaminations on the powder particles due to the presence of alloying elements with high oxygen affinity such as chromium, vanadium and manganese. Thermodynamically stable oxide phases, present on the particle surface, reduce the sintering activity since they act as diffusion barriers [5]. Furthermore, they weaken the inter-particle connections developed as they create a network of oxides after sintering which reduces the toughness similar to networks of carbides on grain boundaries in wrought steels [1, 2].

Thus, it is believed that if a proper way to reduce surface oxides before the HIP process can be found, the metallic bonding between the particles will increase and so toughness will be enhanced and PM production of HWS could be established. One solution to implement such a reduction process into the HIP process could be to perform vacuum annealing of the powder in the HIP capsule before it is sealed.

The aim of this thesis is to analyze the surface of the X40CrMoV5-1 HWS powder and the processes that take place on the surface during vacuum sintering. This knowledge can be used to better understand possible ways of controlling the surface chemistry by heat treatment of the powder in vacuum before HIP and how this process has to be designed to remove the surface oxides and hence, improve the metallic bonding between the powder particles.

High resolution techniques, such as X-ray Photoelectron Spectroscopy (XPS) and Scanning Electron Microscopy (SEM) combined with Energy Dispersive X-ray Spectroscopy (EDX), are used to investigate the chemical composition and state of the powder surface and the morphology, distribution and composition of contaminants. To

observe the change in the surface chemistry by annealing, a furnace attached to the XPS vacuum system is used for heat treatments. Furthermore, thermal analyzing techniques such as Dilatometry (DIL), Differential Thermal Analysis (DTA), Residual Gas Analysis (RGA) and Thermogravimetry Analysis (TGA) are applied.

Dilatometry is used to compare the sintering behavior of the loose powder mass, whereas DTA provides information about the phase changes that take place while heating the powder up. The RGA and TGA measurements give information about the surface interaction of the powder with the vacuum.

2 Theoretical background

2.1 Hot Work Tool Steels

Tool steels are mostly used to process metals and plastics [4]. According to EN ISO 4957 [6] forgeable tool steels can basically be classified into three groups:

Cold Work Tool Steels (CWS) own the highest hardening capacity among the tool steels and can contain a high fraction of carbides to improve the wear resistance. They are used to temperatures up to ~ 250 °C. In Hot Work Tool Steels (HWS) precipitation hardening is used to increase the creep resistance as they are used for work piece temperatures from about 400 to 1200 °C. High Speed Tool Steels (HSS) are a combination of both former mentioned steels. They contain carbides in a creep-resistant and hardened matrix [4].

The main application field of HWS is the hot-forming of work pieces made of metal. The group of HWS itself can be divided into three subgroups as well. Steels with low secondary hardening such as e.g. 56NiCrMoV7 are used for forging dies. The second group contains steels with a significant secondary hardening. For example, the steel X40CrMoV5-1 (X40) is used for casting molds and pressure casting dies for aluminum alloys. Therefore it is quenched and tempered to strengths of about 1450 - 1600 MPa. HWS of the third group are used for very high temperature applications. It is based on oxidation resistant austenitic steels and nickel-base alloys. Both are used because they undergo less diffusion induced creep due to their denser atomic packaging in the face-centered cubic lattice [4].

The durability of HWS mostly depends on the wear resistance and fracture toughness. The wear resistance is important to decrease abrasion and depends, amongst other things, on the hardness and the content and distribution of carbides. Contrary to CWS and HSS, in Hot Work Tool Steels high fracture toughness is very important as well to delay cracks. This is due to temperature changes during service. These induce plane stresses by thermal expansion and contraction of the surface. At non-metallic inclusions and carbides this leads to micro plastic deformations and that again initiates cracks. By penetration of the work piece into these cracks, parts of the work piece stick to the tool and thus the cracks can be driven even deeper into the tool due to the wedge effect and eventually fracture the tool. The higher the fracture toughness of the tool material, the deeper the crack can penetrate before breakdown [4, 7].

2.2 Powder Metallurgy

Powder Metallurgy (PM) is concerned with the processing of powders into useful engineering components. The principle of all PM methods is to densify powder material by using temperatures below the liquidus temperature of the main component and in some cases additional pressure [5].

There are some key attributes for the use of powder metallurgy:

- For high performance applications the main reason to use PM is the possibility to achieve superior mechanical properties compared to cast products. This is due to lower grain and carbide sizes, prevention of macro-segregation and isotropic material properties. This makes powder metallurgy very attractive for tool steels [4, 5].
- PM can be used for achieving properties which cannot be achieved by conventional production techniques at all, like e.g. filtering materials by not completely densifying the powder [4, 5].
- PM enables the economical production of complex parts, like components for the automotive industry, e.g. valve seat, shock absorber components, etc. This area is dominated by concerns over productivity, tolerances and automation [5]. With choosing powder metallurgy as a way of production, a large production volume can be achieved with a near net shape. Hence, production steps are reduced and exploitation of raw material is increased to about 95% [8].
- PM enables the production of materials which would be hard or impossible to produce by other technique such as hard and high-temperature materials, ceramics, etc. [5].

2.2.1 Steel powder production

There is a close correlation between the quality of the powder and the properties of the finished product which gives the powder production a big weight in the whole PM production procedure. There are several ways to produce powders. It can be done mechanically without phase change like milling, or mechanically with phase change like atomization processes with water or gas. Other possibilities are to produce powder by electrolysis or reduction processes of e.g. oxides [8]. The powder investigated in this thesis was produced by atomization, thus this method will be explained in more details.

The production of metal powders by disintegration of molten material is generally regarded as the most economical method for alloys. Size, form and structure of the produced particles vary over a very broad range. These attributes depend on the amount of energy applied to the melt, the temperature and viscosity of the melt, the surface tension and the cooling rate. These factors also influence each other – for example, with increasing

temperature the viscosity decreases, etc. In general it can be said that with decreasing viscosity the particles become more spherical [8].

The solidification time of the metal droplets depends on their size and lies between 1 and 50 ms. This is equal to a cooling rate of 10^3 to 10^4 Ks⁻¹. Such high cooling rates inhibit strong segregations of elements in an alloy. So, it is enough to keep even those elements in solution in the matrix phase which otherwise would form coarse structural phases such as carbides in HSS. Even meta-stable states can appear in certain alloys. There are two methods that can reach such high cooling rates. One technique is the so called “splat quenching”. In this technique melt droplets impact on a cooled metal target. This leads mostly to flake-shaped powders. The other technique is the atomization by water or gas impact and cooling of the droplets by accelerated convection in gases or water. This is the most often used method in practice for prealloyed steels [8].

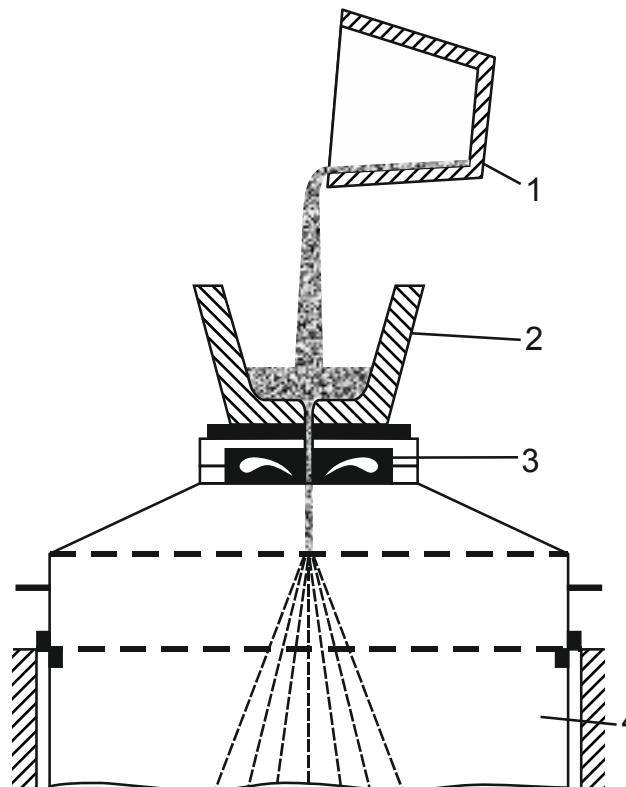


Figure 1: Schematic drawing of the atomization process of prealloyed powder; redrawn from [8]; 1.) Prealloyed melt; 2.) Gathering cup; 3.) Nozzles; 4.) Container

The principle of this technique is shown in figure 1. High pressure water or gas jets impact on the molten metal stream and disintegrate it into droplets which then solidify rapidly. Figure 2 shows a schematic comparison of spherical gas atomized and irregular water atomized powder. The differences in the shape developed due to the much higher cooling rate by water atomization of about 10^4 to 10^8 Ks⁻¹. Therefore the droplets have too short time to form spheres which would be the state with the lowest surface energy [3].

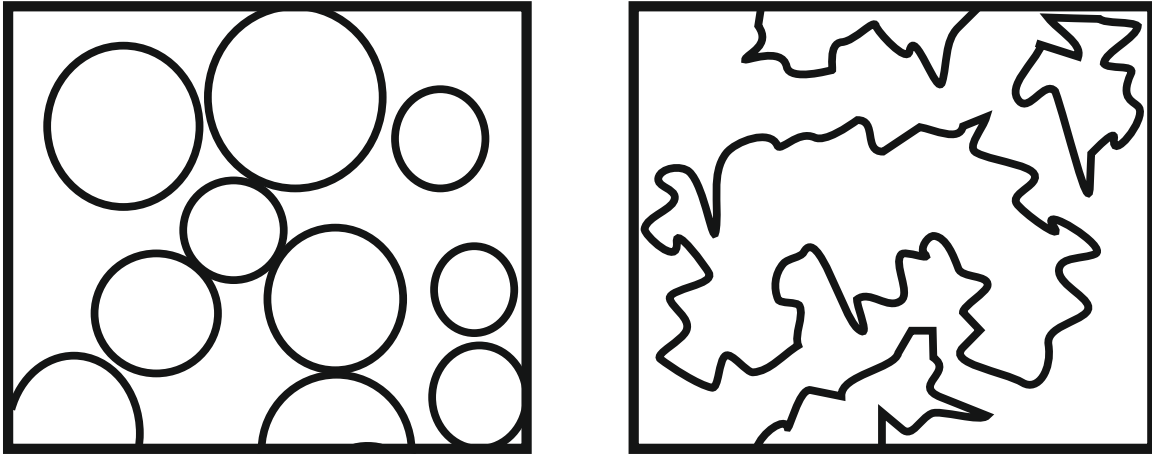


Figure 2: Schematic comparison of gas (spherical) and water (irregular) atomized steel powder, repainted from [9]

Both techniques, respectively powder shapes, have a few advantages and disadvantages. The water atomization produces irregular shaped powder and thus leads to a higher surface area. Therefore, the sintering activity is enhanced as the reduction of surface is the driving force for sintering (see chapter 2.2.2). Also, the irregular particles are easier to compact and the green strength is higher compared to spherical powder as the irregular particles tend to mechanically interlock. On the other hand, the spherical shape of the gas atomized powder leads to the highest settled apparent density. This is important for high alloyed steels as they are difficult to compress. In addition the oxide content in water atomized steels powder is much higher compared to the gas atomized because of the larger surface and the use of highly oxidizing water. Water atomizing is thus only used for elemental iron and low alloyed steels as some alloying elements form very stable oxides (see chapter 2.3) [5]. Hence, for atomization of high alloyed steels inert gases like argon, helium or nitrogen are used. Besides the low price for nitrogen, its main advantage is that it is soluble in steels (max. 2.8 wt.-% in pure γ -Fe [10]) contrary to argon and helium which have no solubility at all. Thus nitrogen gas inclusions from the atomization process can be removed afterwards, whereas this cannot be done for argon and helium inclusions [8].

2.2.2 Sintering and Hot Isostatic Pressing

In the conventional press and sintering route, previous to sintering the powder is usually mixed, compacted and shaped [5]. As in this thesis high alloyed powder is used, it cannot be processed in a conventional sintering route by pressing before sintering due to the high alloying content in the powder, resulting in high powder hardness and so very low compressibility. To achieve best possible properties of the tool, the powder is supposed to be processed by Hot Isostatic Pressing (HIP), which is an advanced technique of sintering. Therefore it is important to know how these techniques work and which factors are of importance during respective consolidation.

Solid state sintering

Sintering is a method to densify a loose or compacted powder by using elevated temperatures. The temperature reaches about $2/3$ to $3/4$ of the solidus temperature of the powder material. The driving force for the consolidation of the loose powder to a solid body is the reduction of free enthalpy by reducing inner and outer surfaces, such as the powder particle surfaces, pore channels and walls as well as grain boundaries [11]. The main parameters to control this process are temperature, time, particle size and the diffusion coefficient as this is a diffusion controlled process [8]. The emphasis of these factors depends on the time since they change during sintering [12].

A schematic drawing of the sintering process for two particles is shown in figure 3. The sintering process can be divided into three steps:

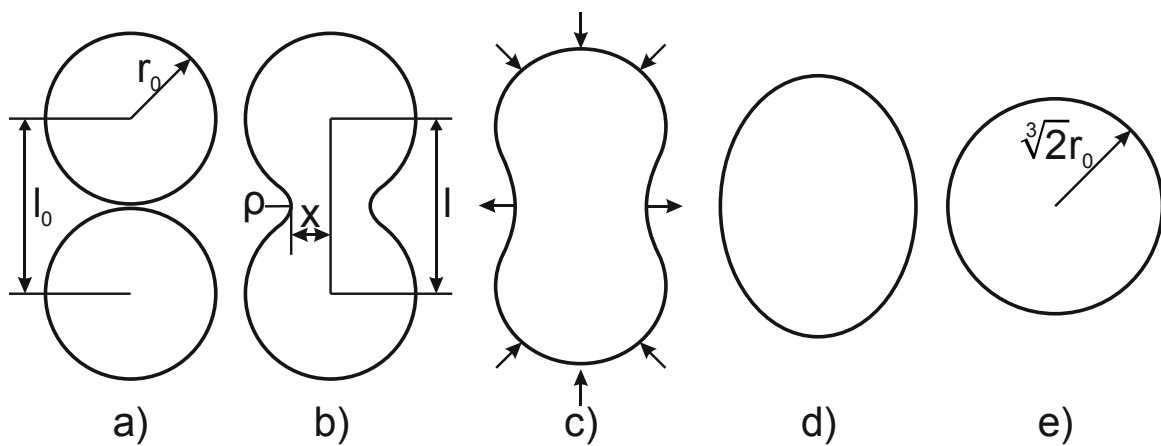


Figure 3: Sintering steps after Frenkel; repainted from [11]: a) Adhesion of particles; b) Sinter-neck building; c) Sinter-neck growth; d) Elliptical shape; e) Spherical shape

In the early stage the particles rearrange by adhesion and the sinter necks start to develop via gas and surface diffusion. Thereby the surface is reduced up to 50 %. However, the shrinkage is only about 3 % and the porosity is open. During following sinter holding the sinter necks grow. This leads to a further reduction of free surface and a strong shrinkage. Diffusion occurs mainly by grain boundary and lattice diffusion. Though, the porosity is still open. In the final stage only slight consolidation takes place, but the porosity transits to a closed one. Strong grain growth also occurs in this step [11, 12].

Hot Isostatic Pressing

Hot Isostatic Pressing (HIP) combines elevated temperatures with high isostatic pressure to compact loose powder. The temperatures typically ranges from 800 to 1500 °C, in special cases up to 2000 °C, and the applied pressure reaches from 100 to 3000 bar during a holding time of 1 to 4 h [8]. The driving force is, besides the already discussed reduction of the surface, the applied pressure. This leads to plastic deformation, dislocation creep and

viscous flow. Due to this second driving force, the applied temperature is lower compared to solid state sintering [5].

In the HIP technique the powder is filled in a capsule and this capsule is vacuum degassed and sealed. Afterwards the capsule is placed in the vessel. The isostatic pressure is applied by gas which is usually argon [8].

Compared to ordinary sintering, this method has a few advantages and disadvantages. The lower temperature leads to lower grain growth and by the use of pressure the densification increases. Thus, HIP is chosen if very high material properties are needed. Nevertheless, the whole process requires long cycling times and expensive and sensible molds. The product shape is also limited due to the encapsulation [8]. As the applied pressure is isostatic, the shear stresses on the particles are very low. This means that contaminations present on the particle surface are not going to be destroyed and network-like pattern can even be seen in the full-density state [5].

2.3 Oxides on powder surfaces

The powder surface is one of the main determining factors for the properties of PM products as it defines the connection between the powder particles. Therefore, it is mandatory to know how to control the powder surface chemistry and how it interacts with the surrounding atmosphere while sintering. There are two basic drawbacks by contamination of the powder surface. Firstly, the contaminations, e.g. oxide phases, act as a diffusion barrier due to the low diffusion through them, since they are mostly ceramic phases. This leads to a slower sintering process [3]. Secondly, the contaminations weaken the metallic bonding between the particles which leads to worse mechanical properties, especially ductility and fatigue [2, 7].

Weddeling et al [13] showed for gas atomized, high alloyed Mn-Cr austenitic steel powder that the surface is covered by a thin iron-oxide layer of about 4 nm thickness. Oxygen affine elements such as chromium, manganese and silicon form larger oxide particulates generating island-like pattern on the powder surface. Continulative investigations of Zumsande et al [14] revealed that removal of main parts of these surface oxides is possible by annealing in ultra-high vacuum conditions and high temperatures.

Although the X40CrMoV5-1 powder investigated in this work is differently alloyed, both materials contain considerable amounts of chromium, manganese and silicon and additionally vanadium in the X40. Thus it is expected that annealing under the same conditions can also remove main parts of the surface oxides covering the X40 powder.

2.3.1 Thermodynamic description of oxide reduction

Chemical reactions occur spontaneously when the difference in the Gibbs free energy ΔG of the reaction products and the reactants is negative:

$$\Delta G^0 = \Sigma G_{(\text{reaction products})}^0 - \Sigma G_{(\text{reactants})}^0 \quad (2.1)$$

Without any reducing agent the removal of oxides occurs by dissociation according to:



Me denotes the metal and Me_xO_y its oxide. Taking Formula (2.1) and (2.2) into account the change of the Gibbs free energy becomes equal to:

$$\Delta G_1^0 = \frac{2x}{y} G^0(\text{Me}) + G^0(\text{O}_2) - \frac{2}{y} G^0(\text{Me}_x\text{O}_y) \quad (2.3)$$

The equilibrium constant K can be defined which indicates the direction of a reaction:

$$\Delta G^0 = -RT \ln K \quad (2.4)$$

with the gas constant R ($8.314 \text{ J}\cdot\text{mol}^{-1}\cdot\text{K}^{-1}$) and the temperature T in Kelvin. The equilibrium constant K can be determined by dividing the activities of the reaction products by the activities of the reactants:

$$K = \frac{\left[a^{\frac{2x}{y}}(\text{Me}) \cdot a(\text{O}_2) \right]}{a^{\frac{2}{y}}(\text{Me}_x\text{O}_y)} \quad (2.5)$$

The activity is a measure of the “effective concentration” of an element in a mixture and is defined by the ratio of its vapor pressure in the mixture and the vapor pressure of the same element as a pure solid or liquid under the same environmental conditions. This means that the activity of an ideal gas is equal to its partial pressure. Therefore equation (2.5), assuming O_2 as an ideal gas, can be expressed as:

$$K = p(\text{O}_2) \quad (2.6)$$

Considering equation (2.4) and (2.6) the equilibrium oxygen partial pressure can be determined by

$$p(O_2) = \exp\left(-\frac{\Delta G_1^0}{RT}\right) \quad (2.7)$$

[15, 16]. By the use of thermodynamic software, which are based on thermodynamic databases, the temperature dependency of the oxygen partial pressure for all kinds of oxides can be calculated and plotted. Figure 4 shows such a diagram for some oxides of interest. For conditions above each line (high oxygen partial pressure, low temperature) the oxide is favored. Below the lines (low oxygen partial pressure, high temperature) the oxide gets reduced and the dissociated state is more stable [15, 17].

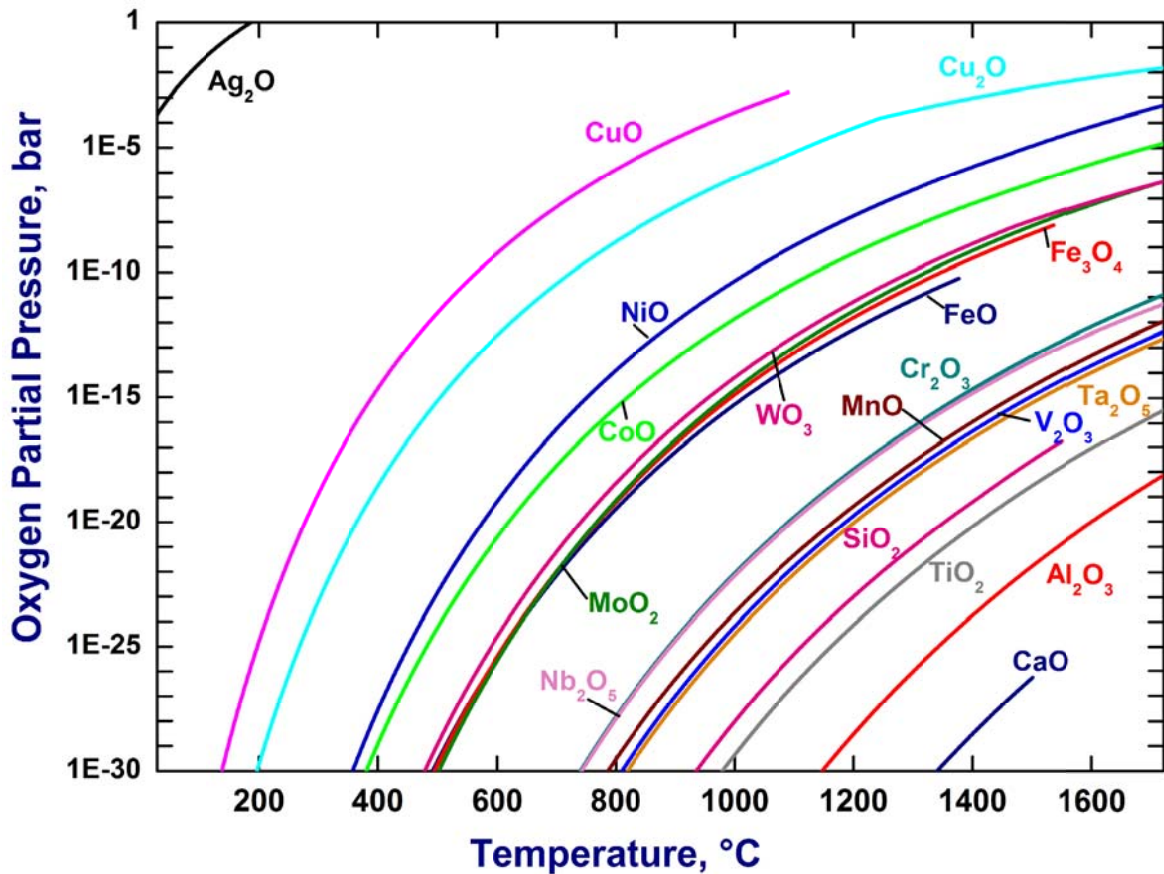


Figure 4: Equilibrium oxygen pressure as a function of temperature for some oxides of interest; redrawn from [17]

It can be seen that theoretically every oxide can be reduced. But, as the temperature is limited in the sintering process, the oxygen partial pressure must be very low to reduce highly stable oxides like MnO or SiO₂. As sintering in vacuum is quite expensive it is basically used for the production of high quality PM parts. In the most industrial applications reducing agents like hydrogen or carbon monoxide are used [8].

Carbon monoxide can evolve from the reaction of carbon in the steel with oxygen. This is called direct carbothermal reduction process and can be expressed according to the following equation:



The resulting carbon monoxide can then further react with oxide to form carbon dioxide:



This reaction is called indirect carbothermal reduction [15].

Another way to estimate the stability of oxides is to use an Ellingham-Richardson diagram. Figure 5 shows such a diagram with a plot of the Gibbs free energy for different oxides against the temperature. The lower the ΔG^0 line is located, the more stable is the oxide. In this way it is possible to compare the stability of the metallic oxides with CO and CO₂ and it can be estimated which temperatures have to be chosen to reduce an oxide [15, 16, 18].

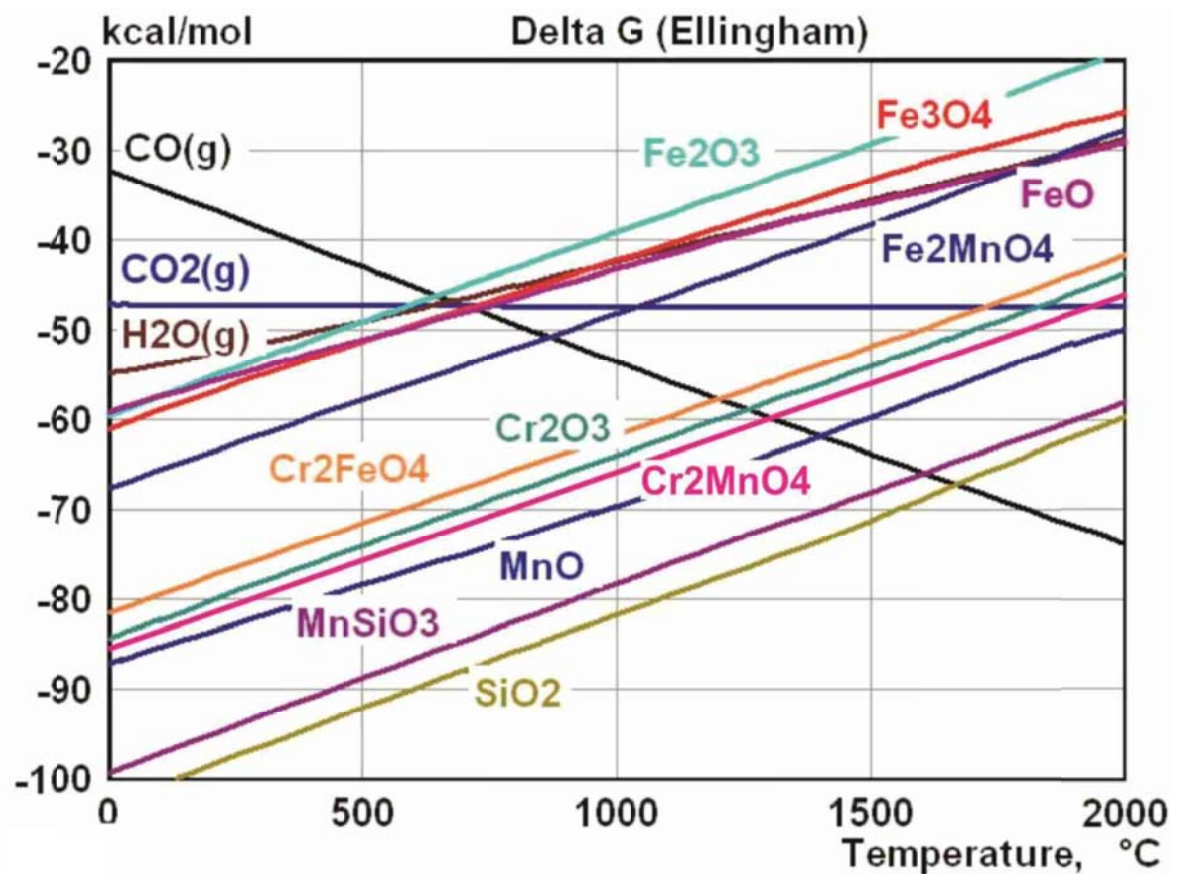


Figure 5: Ellingham-Richardson diagram for selected oxides, redrawn from [19]

Furthermore it can be seen that the Gibbs free energy lines of CO and CO₂ do also have an intersection point. This is due to the so called Boudouard reaction which favors the stability of CO above 720 °C [15, 16].

2.3.2 Previous investigations on X40CrMoV5-1

First attempts to produce X40CrMoV5-1 (X40) in a PM route by atomizing and HIP processing were done in the 1980's [20]. Recent investigation revealed, that HIPed material of the X40 shows less ductility compared to cast material [1, 2]. Both authors, Schneiders and Wendl, explain the less contraction of area by fractures along the former powder particle boundaries, which are probably weakened by residual contamination layers. This leads to higher localized strain and thus transcrystalline fracture surfaces. Analogue to the ductility it lowers the impact work [1]. The mechanical properties of the HIPed material can be improved by hot forming as this destroys the oxide networks, but this is not economically efficient [2].

A hint that this weakening of the former particle boundaries is due to oxides on the powder surfaces is given by the diploma thesis of Oppenkowski [21] who analyzed, amongst other things, the influence of fused tungsten carbides in the X40 powder after HIP. He found out that the addition of 10 vol.-% of fused tungsten carbides to the X40 powder enhances the fracture toughness. Even an addition of 30 vol.-% leads to the same fracture toughness as the X40 alone, although increasing hard phase contents usually lower the fracture toughness. This is due to the fact that with increasing hard phase content, the distance a crack has to pass through the ductile matrix from one brittle hard phase to another decreases [22]. The enhancement in fracture toughness is explained by the binding of oxygen in the fused tungsten carbides during the HIP process and so the metallic bonding between the powder particles improves [21].

In [1] some attempts to remove surface contaminations by drying, annealing in hydrogen containing atmosphere at 550 °C or annealing in medium vacuum conditions ($4 \cdot 10^{-2}$ mbar) of up to 1050 °C were performed, but no pronounced improvement of the mechanical properties could be achieved. However, no systematical investigation of the effect of different vacuum annealing conditions prior HIP processing on the contamination layer has been performed yet.

Therefore, the as-received powder is studied in this work to identify the contaminations present. Furthermore, different vacuum annealing conditions are applied to observe the changes in the powder surface chemistry and the interaction with the surrounding atmosphere. In the end, this knowledge can be used to design a vacuum annealing process prior to HIP and thus improve the bonding between the former powder particles in the final product.

2.4 Material and experimental techniques

A wide range of analytical techniques are used for the powder characterization in this thesis. Table 1 gives a short overview of those techniques and their use. A detailed description can be found in the following chapters.

Table 1: Overview of the applied experimental techniques

Experimental technique	Use in the investigation
X-ray Photoelectron Spectroscopy (XPS) combined with Ar-ion sputtering	Surface chemical analysis Chemical state identification Depth profiling
Scanning Electron Microscopy (SEM) combined with Energy Dispersive X-ray spectroscopy (EDX)	Morphology of the powder surface Chemical microanalysis Imaging of powder cross sections
Thermogravimetry Analysis (TGA)	Extend of weight loss (oxide removal) during heating
Residual Gas Analysis (RGA)	Analysis of the emission products composition while heating
Differential Thermal Analysis (DTA)	Analysis of phase transformations
Dilatometry (DIL)	Analysis of sintering behavior
Calculation of phase transformations (CALPHAD)	Estimation of phase transformations

2.4.1 Material and sieve analysis

The steel powder under investigation in this thesis is the Hot Work Tool Steel X40CrMoV5-1 (material number: 1.2344, according to DIN EN 10027-1 [23]) which was atomized with inert gas. The chemical composition according to [1] can be seen in table 2. The amount of silicon is lower than the limit set in EN ISO 4957 [6].

Table 2: Nominal chemical composition of the investigated steel powder in wt.-%

Material	C	Cr	Mo	V	Mn	Si
X40CrMoV5-1	0.39	5.19	1.36	0.98	0.28	0.24

The sieve analysis has been performed after DIN ISO 4497 [24] and DIN 66165 [25] with vertically arranged vibratory sieves and mesh sizes of 200, 150, 100, 63, 36 and 25 μm .

2.4.2 X-ray Photoelectron Spectroscopy

The X-ray Photoelectron Spectroscopy (XPS), also known as Electron Spectroscopy for Chemical Analysis (ESCA), is a surface sensitive method for analyzing chemical

compositions and states of solids [26]. Hence, it was used to analyze the surface chemistry of the powder particle of the steel under investigation in this thesis. Furthermore, combined with argon-ion etching it gave the possibility for depth profiling.

An XPS-system is basically build of an X-ray source, an electron analyzer and a sample holding device with attached sample preparation facilities, all kept under an ultra-high vacuum (UHV). The UHV-vacuum is necessary to avoid interactions of the released electrons with the molecules in the atmosphere. Common X-ray sources are aluminum ($K_{\alpha}=1486.6$ eV) and magnesium ($K_{\alpha}=1553.6$ eV) [26].

The principle of this technique is to irradiate the sample with monochromatic soft X-rays. This leads to the emission of the electrons due to the photoelectric effect. These electrons carry characteristic information in the energy level about the emitting atom. By plotting the number of emitted electrons over their kinetic energy a spectrum can be received. As every element has its own characteristic spectrum, the obtained spectrum of an alloy is roughly the sum of elemental spectra of all individual elements [26].

The photoelectron effect describes the emission of an electron from a core level after collision with an X-ray if the X-ray photon energy $h\nu$ is bigger than the binding energy E_B of the electron. This process is schematically shown in figure 6.

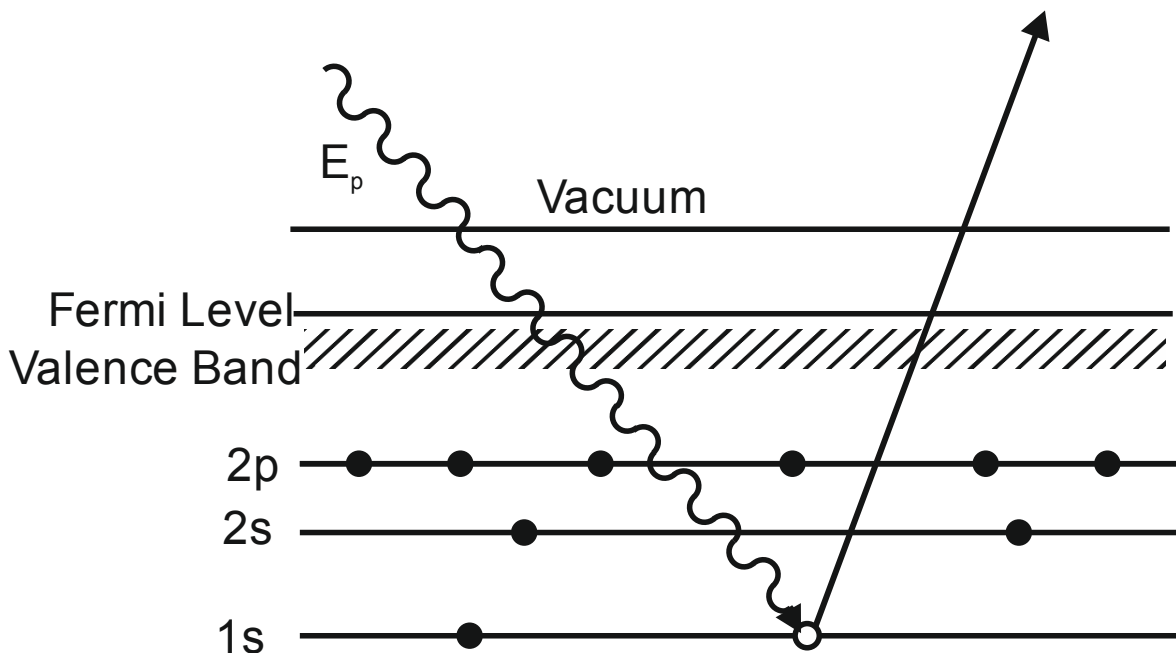


Figure 6: Process of photoemission, redrawn from [27]

The kinetic energy E_K of the released electron is described by

$$E_K = h\nu - E_B - W_S \quad (2.10)$$

Thus the kinetic energy E_K is not an intrinsic material property. The parameter W_S is the so called spectrometer work function which is identified during calibration of the spectrometer. After rewriting equation (2.10) to

$$E_B = h\nu - E_K - W_S \quad (2.11)$$

the binding energy E_B can be calculated which allows to identify the element of origin, as the binding energy is characteristic for each element [27].

Beside the peaks, the spectrum is composed of a background. Ejected electrons can undergo inelastic scattering on molecules of the specimen or the atmosphere, which leads to a loss of kinetic energy during the escape and the formation of a background in the spectrum. Whereas electrons that escape without any scattering and thus without energy loss form the characteristic peaks. The scattering of electrons on atoms is also the reason for the high surface sensitivity of XPS, as only electrons from the top tens of angstroms below the surface have a chance to escape without scattering, even if the ionization depth is deeper [26]. Therefore the XPS information depth is up to 10 nm. In general, the information depth depends on the electron mean free path λ , which is a function of the kinetic electron energy and also depends on the material under investigation [28]. About 65 % of the measured signal will emanate from a depth $< \lambda$, 85 % from a depth $< 2 \lambda$ and 95 % from a depth $< 3 \lambda$ [27]. For the elements Fe, Mn and Cr and their oxides λ has a value between 1 and 2 nm [19].

The chemical composition can be derived by the area under each peak. Beside the chemical composition, the chemical state of the atoms can also be determined by XPS. The chemical bonding leads to differences in the binding energies of the electrons in the shells. This in turn leads to a shift of a few electron volts in the XPS spectrum, which can be used to identify the binding state [28].

To describe the origin of an emitted electron the so called chemists' or spectroscopists notation formalism is used. It names the photoelectrons on the basis of their quantum numbers. The peaks observed in the spectra are labeled by the scheme n_lj . The n specifies the principal quantum number which refers to the electron shell. In the periodic table the shells are labeled by letters, beginning with K along the alphabet. The shell K corresponds to a quantum number $n=1$, L to $n=2$, etc. According to that, n can only have positive integer values [27].

The l describes the orbital angular momentum which determines the shape of the orbital. Values of l range from 0 to $n-1$, i.e. in the shell $M(n=3)$ l can have values from 0 to 2. For XPS usually a letter is used instead of a number which is shown in Table 3.

Table 3: Notation of the quantum numbers [27]

Value of l	Usual notation
0	s
1	p
2	d
3	f

Peaks in the spectra that origin from orbitals with an angular momentum number higher than 0, are usually split into two, due to the interaction of the spin with its orbital angular momentum. The spin angular momentum s can have either the value of $+1/2$ or $-1/2$. The quantity j can be determined by vector addition of l and s : $j=|l+s|$. Thus, one electron from the same shell can have two different values corresponding to the prefix of s . The ratio of the peak intensities of these double peaks can be looked up in corresponding literature. The value of the energy difference between those double peaks is a function of the strength of the spin orbit and the atomic number [27].

Reading the spectrum

The XPS-spectra are plotted as a number of electrons in a certain energy interval against the electron binding energy. The horizontal axis usually begins with a value of zero with reference to the Fermi level and increases to the left [27]. For the spectra interpretation the user has to know which kinds of peaks can occur and where they originate from.

The narrowest lines that can be observed in the spectra are typically the photoelectron lines. They appear as most intensive and relatively symmetric. These lines are mainly used for the analysis.

Auger lines show a quite complex pattern. As they are a consequence of the photoemission process, they carry characteristic information about the elements of origin and can additionally be evaluated.

By use of non-monochromatic X-rays so called satellite lines occur. This happens as magnesium and aluminum X-ray source do not only emit $K_{\alpha 1,2}$ X-rays, but also K_{1-6} and K_{β} X-rays.

As no anode material is completely pure, impurities lead to the emission of some different X-rays as well. This could be e.g. magnesium in aluminum or vice versa. These ghost lines result in small peaks corresponding to the main peak and should not be considered in line identification.

So called shake-up lines appear in rare cases when an ion is left in an excited state, a few

electron volts above the ground state. The difference in the electron binding energy leads to a difference in the kinetic energy and with that to the formation of a satellite peak, a few electron volts lower than the main peak.

Furthermore, multiplet splitting can cause a photoelectron line to split into asymmetrical components. Interactions of photoelectrons with other electrons lead to the so called energy loss lines about 20 - 25 eV above the energy of the parent lines [26].

Curve-fitting

By the use of curve fitting, the fractions of the different chemical states of an element can be estimated. For example, the elemental peak can be divided into metallic and oxidic parts. For that purpose the measured elemental curve is fitted by single peaks of the metallic and oxidic states. An example of such procedure is given in figure 7. The area under each curve corresponds to the amount of atoms in the associated chemical state. Thus, the fractions of each state can be calculated. As the state of oxides can change by ion etching, it is not always possible to distinguish the exact oxidic state, e.g. Fe^{2+} and Fe^{3+} after ion etching.

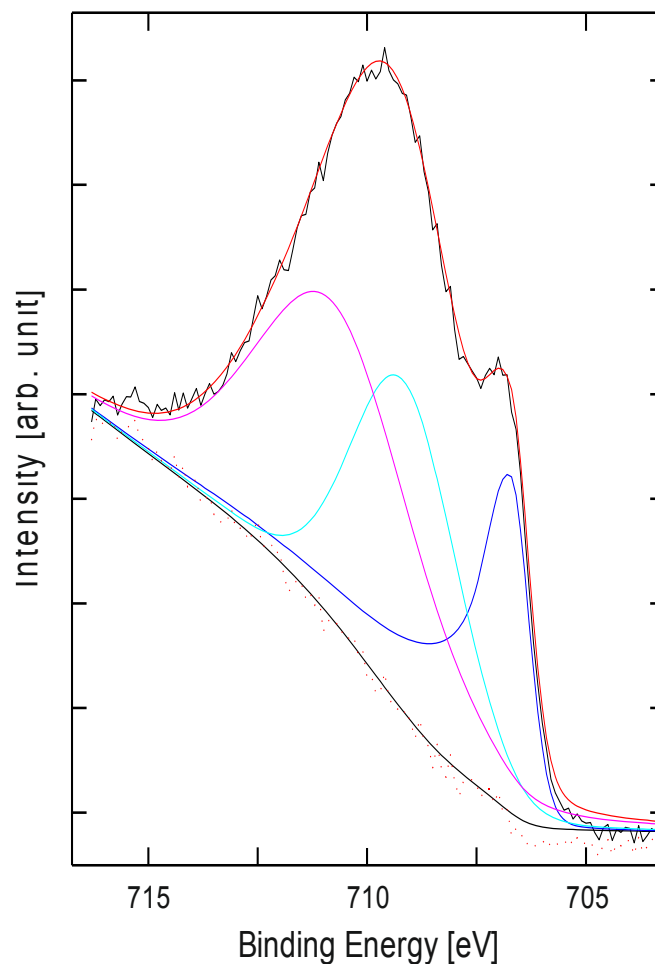


Figure 7: Example for the analysis of the chemical state by curve fitting. The measured peak ($\text{Fe } 2p \ 3/2$) is composed of a metallic part (blue) and two oxidic parts: Fe^{2+} and Fe^{3+} (cyan and magenta)

Experimental setting

An instrument PHI 5500 by Physical Electronics was used for measurements in this work. The analyzed area was about 0.8 mm in diameter. This implies that a large number of particles were measured at once and thus, the measurements give statistically reliable average results of the general powder surface composition.

Controlled ion etching was performed by the use of an argon beam with an accelerating voltage of 2 or 4 kV. The raster area of the argon beam was 4 mm x 5 mm. This corresponds to an etch rate of about 3 nm·min⁻¹. The calibration of the etch rate was performed on a flat oxidized tantalum foil.

The heat treatment took place in a furnace attached to the XPS system in ultra-high vacuum conditions of about 10⁻⁷ mbar to avoid exposition to air. The annealing time was 1 h for each heating step. For investigations of the as-received state, the powder was pressed into aluminium plates or glued on a carbon tape. The risk of contamination from Al plates is the disadvantage of the pressing on it. On the other hand, mounting on a sticky carbon tape leads to risk of overestimation of the measured carbon content. The comparison of both allows estimating how strong the mounting type influences the measurements. The powders heat treated from 500 to 800 °C were pressed on copper plates. For those samples heat treated at 900 and 1000 °C the pressing on plates was not necessary, as the powder starts to sinter during the heat treatment. Hence, the loose powder mass was placed in a small container made of stainless steel without risking to lose powder particles within the UHV-system when moving the sample after heat treatment.

2.4.3 Scanning Electron Microscopy

The Scanning Electron Microscope (SEM) is a microscope which uses a focused electron beam that scans the surface and produces an image of the object by measuring the interaction of the beam with the material. The use of an electron beam provides a number of benefits compared to light microscopy. As the wavelength of the electrons is very short and the parallelism of the beam high, big magnifications of theoretically up to 1,000,000:1 with simultaneous high depth sharpness can be achieved. On the other hand, the images do not carry any color information. Thus, only a light-dark contrast can be displayed.

In SEM an electron source provides the electrons which are accelerated in an electric field with common voltage of up to 30 kV. The beam is focused and controlled by magnetic coils. To avoid interactions between the electron beam and the surrounding atmosphere the process takes place under high vacuum conditions.

The interaction of the Primary Electron (PE) beam and the specimen creates several secondary products which can be used for imaging and analysis. These occur from different sections around the electron spot in the bulk material as can be seen in figure 8. The mostly used signals are the Secondary Electrons (SE), Backscattered Electrons (BE) and X-rays.

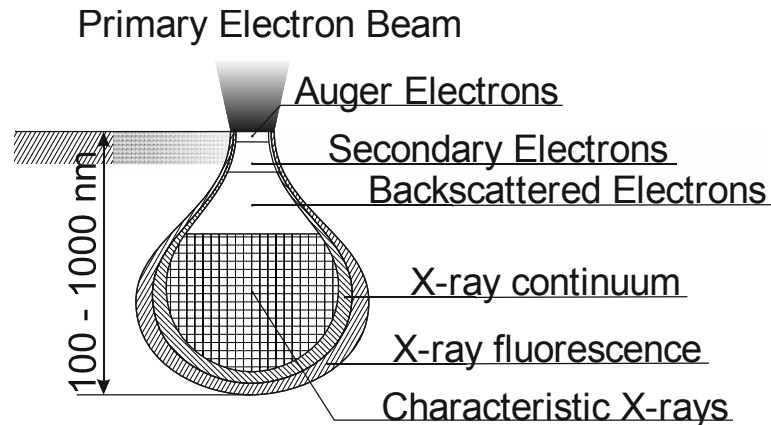


Figure 8: Interaction volume of the primary electron beam and the specimen material; redrawn from [29]

Secondary Electrons are generated by inelastic collisions of the Primary Electrons of the beam and the atoms in the specimen. They only reach low energy levels with the most probable energy of 2 - 5 eV [29]. Due to their low energies the detectable Secondary Electrons originate from the top atomic layers of the sample. As areas that are facing the detector appear brighter because more electrons can reach it, the SE-contrast provides a good method to investigate the topography of the sample surface.

Backscattered Electrons originate from the primary beam itself as they are reflected Primary Electrons. They have a much higher energy level as Secondary Electrons (> 50 eV) and carry information from a deeper volume of the specimen about the atomic mass of the reflecting atoms. This is due to the fact that heavier atoms are more likely to reflect electrons than lighter elements. Thus, it can be used to produce a contrast between areas with different chemical compositions.

Besides the possibility of imaging, SEM can be used for local chemical analysis, as in the specimen created X-rays carry characteristic information about the elements of origin. These X-rays occur when a Primary Electron removes an electron of the inner shell of an atom. An electron of a higher shell has to fill this vacancy and the difference of the energy levels of the electron shells is released by an X-ray quantum. The energy of this quantum is characteristic for the kind of element. By analyzing the X-Ray spectrum, the chemical composition of a small area of the sample surface can be determined. This method is called EDX-Analysis (Energy Dispersive X-ray Analysis) [29, 30].

Therefore, SEM was used in this thesis to investigate the morphology of the powder surfaces and imaging of powder cross-sections. Combined with EDX, chemical

microanalysis was performed to investigate individual particulate and selected areas on the powder surface.

A Scanning Electron Microscope (SEM) type LEO Gemini 1550 with a Field Emission Gun (FEG) was used. To analyze the powder surface, the InLens SE detector was utilized with an accelerating voltage of 15 kV, an aperture size of 20 μm and a working distance of 8.5 mm. Observations of cross-sections have been performed by the use of a BE-detector and an aperture size of 30 μm . EDX studies were performed with an INCA X-sight EDX system. Before the investigations of the sample started, the system was calibrated with a cobalt standard.

For analysis of cross-sections the powder was embedded in conductive epoxide resin. Subsequently, the samples were grinded using SiC paper with a grit size of 1000 and polished using 6 μm , 3 μm and 1 μm diamond suspensions. The last step was polishing with Oxide Polishing Suspension (OPS) which contains SiO_2 -particles with a size of about 0.25 μm and having a pH-value of 9.5.

For SEM investigations of heat treated powder the XPS samples have been used. They have been exposed to air prior to the SEM investigations. This has to be taken into account when evaluating the SEM images.

2.4.4 Thermogravimetry Analysis

The Thermogravimetric Analysis (TGA) is a technique in which the change in the sample mass is measured while the sample is subjected to a temperature change. This is done by connecting the crucible with the sample to a highly accurate microbalance. While heating the sample it can either loose mass (e.g. decomposition reactions, evaporation, etc.) or absorb mass due to chemical reactions (e.g. oxidation, corrosion etc.) which leads to a change in the sample mass. It is possible to perform the tests in different atmospheres to analyze the interaction of the sample with the surrounding atmosphere.

Beside the way of plotting the relative mass as a function of temperature or time, also the rate of mass change can be plotted (Differential Thermogravimetry, DTG). When doing it this way, different steps in a series of reactions are more obvious and identifiable as maxima or minima in DTG curves.

Thermogravimetry analysis techniques have been used in metallurgy to study a lot of phenomena such as oxidation, reduction and corrosion processes. In this study TGA was used to identify the temperature ranges and the extent of reduction and degassing processes during heat treatment of the powder [31].

The thermal analyzer STA 449 F1 Jupiter from Netzsch was used for Thermogravimetry Analysis using TG / DTA sample carrier system with tungsten / rhenium thermocouple. The loose powder with a mass of about 100 mg was placed in alumina crucibles for

analysis. An argon atmosphere (99.9999%, purified) with a flow rate of about 50 ml/min was used. Before the measurements started, the system was evacuated and flushed with argon three times before experiment. The heating rate was $10 \text{ K}\cdot\text{min}^{-1}$ and the specimens were heated up to $1300 \text{ }^\circ\text{C}$. The tests have been performed on the unsieved powder and sieve fractions of fine (36 - 63 μm) and coarse (100 - 150 μm) powder.

2.4.5 Residual Gas Analysis

Residual Gas Analysis (RGA), also known as Evolved Gas Analysis (EGA), is a technique to analyze the chemical composition of gases evolved under dynamic vacuum conditions. In case of this thesis it was used to evaluate the interaction between the sample and the vacuum during the heat treatment, as the evolving molecules give indications about the chemical reactions that taking on the surface. The measurement data is given as the partial pressure of the gases which can be plotted against the temperature or time.

The analyzing process can be separated into three steps: ionization, separation and collection.

The ionization is made by collision of the gas molecules with electrons produced in a tungsten filament. Characteristic for a molecule is the ratio of its atomic mass to the electric charge. This ratio will be called mass number in the following. Due to statistical distribution, the molecules can be ionized once or twice, but with a larger probability for the first. For example an N_2 -molecule can either have the mass number 28 ($^{14+14}/_1$) or 14 ($^{14+14}/_2$). Furthermore, molecules can be fragmented. For example, for a CO-molecule the mass number 28 ($^{12+16}/_1$) can be detected as well as C- and O-fragments with the mass numbers 12 and 16.

Via a perforated cathode, the ionized particles are accelerated into a quadrupole which separates the particles by mass number. To achieve that, the quadrupole is made out of four electrodes which are coaxially arranged towards the ion beam. Due to the arrangement of the electric fields only one specific mass number can pass the quadrupole, whereas all the others get deflected. At defined time intervals the electric field changes so that a different mass number can pass the quadrupole and the whole mass spectrum can be filtered in sequences.

For the collection a Faraday-detector is used which catches the discharge of the ions on a metal plate [31].

An RGA unit of type e-Vision EVS-160-080 from MKS Instruments was attached to the vacuum system of the dilatometer for the Residual Gas Analysis. The temperature values were aligned by the time data of RGA- and dilatometer measuring records. The tests were executed in high vacuum conditions ($<10^{-4}$ mbar) with a heating rate of $10 \text{ K}\cdot\text{min}^{-1}$. The chamber was flushed with argon and evacuated twice before experiment. To avoid damage

of the experimental set-up, the temperature was restricted to 1200 °C. A special crucible design was used to ensure a good exchange between the vacuum and the sample (see figure 9) [32].

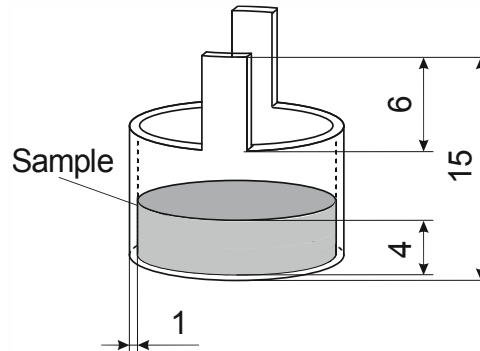


Figure 9: Schematic drawing of the crucible for the RGA measurements; redrawn from [32]

2.4.6 Differential Thermal Analysis

The Differential Thermal Analysis (DTA) is used to detect the characteristic temperatures of phase transformations in a material. The method is based on the effect that phase transformations are either endothermic or exothermic reactions. This means that while the reaction takes place, heat is absorbed (endothermic) or released (exothermic) due to the difference in the Gibbs energies of the phases.

For the observation of this effect the temperatures at the sample crucible and at a reference crucible are measured. The reference crucible is either empty or filled with a substance which does not undergo any phase transformation in the relevant temperature interval. Both crucibles are subjected to the same controlled temperature program in a furnace chamber. A phase transformation in the sample leads to a change in the sample temperature compared to the reference crucible. By plotting the temperature difference of the sample and the reference crucible against the furnace temperature, the kind of reaction (exo- or endothermic) and the temperature range of the phase transformation can be determined. For example melting of a metal requires an input of heat. Thus, this transformation is endothermic and the peak is downwards in the plot. Solidification releases heat and therefore it is the other way around [31, 33].

The DTA-measurements were performed by using a test facility type PT1600 L62/432 from Linseis. The powder was filled into an Al_2O_3 -crucible and the reference body was made of Al_2O_3 as well. The heating rate was $10 \text{ K}\cdot\text{min}^{-1}$ and the atmosphere was helium with a constant gas flow rate of $12 \text{ l}\cdot\text{h}^{-1}$. Before the tests started the chamber was evacuated to $2\cdot 10^{-2}$ mbar and flushed with helium afterwards twice.

2.4.7 Dilatometry

Dilatometry was used in this thesis to observe the sintering and densification behavior of the bulk powder. In this method the elongation of the sample is measured with temperature and time. To compensate the thermal expansion of the measurement set-up a reference measurement with a known reference body has to be performed simultaneously [31].

A dilatometer of type L75VX from Linseis was used in this thesis. It has a vertical equipment configuration so there was no need for pre-compaction of the powder or utilization of bonding agents. The experimental set-up can be seen in figure 10. For the measurement the powder was filled in an Al_2O_3 -crucible and an Al_2O_3 die was placed on top. Subsequently, the unit was fixed between the measuring pins with a pressing force of 300 mN. This force can be neglected concerning the sinter behavior and was just used to lock the sample unit into position.

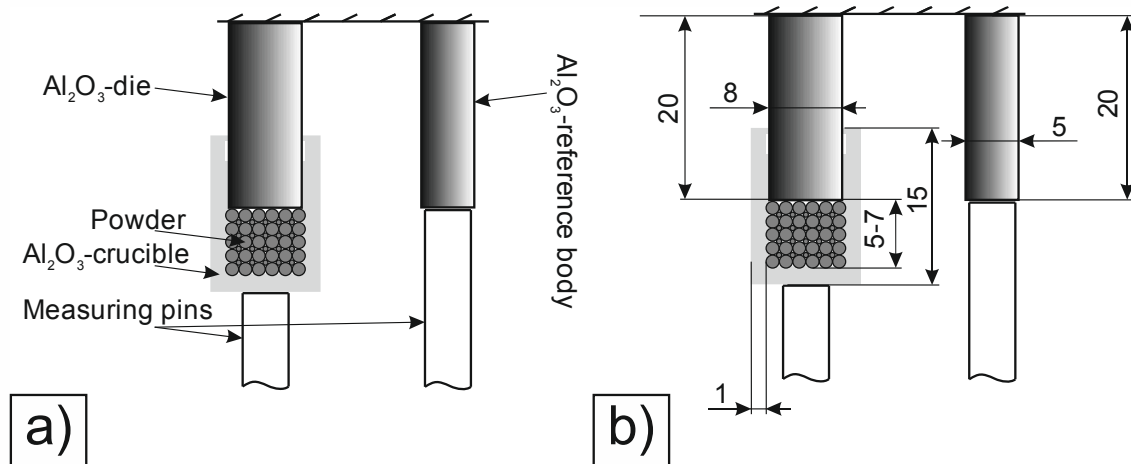


Figure 10: Schematic drawing of experimental set-up for the dilatometry; a) labeling of the components; b) dimensions; redrawn from [32]

For the reference measurement an Al_2O_3 -reference body was used. To measure the elongation, the dilatometer has an installed inductive displacement sensor. The tests were performed in medium vacuum ($< 2 \cdot 10^{-2}$ mbar), but the chamber furnace was evacuated and flushed with argon gas twice before experiment. The tests were performed by the use of a heating rate of $10 \text{ K} \cdot \text{min}^{-1}$.

2.4.8 Thermodynamic calculations

For calculations of phase transformations the program Thermo-Calc[®] was used which is based on the CALPHAD-method (CALculation of Phase Diagrams). This allows calculation of the thermodynamic equilibrium state of multi-phase systems. The principle of CALPHAD is the calculation of the change in the Gibbs energy ΔG , which is defined in the second law of thermodynamics:

$$\Delta G = \Delta U + p\Delta v - T\Delta S \quad (2.12)$$

The first summand describes the change of the internal energy U and the second one the change in the specific volume v multiplied by the pressure p . The third summand takes into account the entropy S multiplied by the temperature T in Kelvin.

As a thermodynamic system always aims to the lowest energy level, a process in a closed system takes place spontaneously for $\Delta G < 0$. In case of a global minimum of the ΔG -function a stable equilibrium exists and in the case of a local minimum a metastable equilibrium exists. The process which sets the equilibrium can be e.g. a chemical reaction or a phase change [34].

In a multicomponent system the entire enthalpy depends on the enthalpy of each component and their miscibility. This miscibility is described by the mixing enthalpy G_{mix} which correlates to the third term in (2.12) [35]. If there is neither an attractive nor a repulsive interaction the solution is called ideal. Thus the miscibility enthalpy in a two-component system can be calculated by

$$G_{\text{mix}}^{\text{ideal}} = RT(x_A \ln x_A + x_B \ln x_B) \quad (2.13)$$

with the mole fractions x_A and x_B and the universal gas constant R . However in real materials there is always an interaction between the components. Therefore, term (2.13) has to be extended by a non-ideal part $G_{\text{mix}}^{\text{xs}}$. In the simplest solution model $G_{\text{mix}}^{\text{xs}}$ is described by:

$$G_{\text{mix}}^{\text{xs}} = x_A x_B \Omega. \quad (2.14)$$

Ω is the interaction parameter which is positive for repulsive and negative for attractive interaction. This means that an attractive interaction leads to the dissolution of B in A and thereby the Gibbs free energy is reduced. With (2.13) and (2.14) the entire miscibility enthalpy can be determined by

$$G_{\text{mix}} = x_A x_B \Omega + RT(x_A \ln x_A + x_B \ln x_B). \quad (2.15)$$

But in general the $G_{\text{mix}}^{\text{xs}}$ -term is more complicated as it has to be extended with the interaction of each component in an n -component system [35] to

$$G_{\text{mix}}^{\text{xs}} = \sum_{i=1}^n \sum_{j=i+1}^{n+1} x_i x_j \left[\Omega_{ij}^0 + \Omega_{ij}^1 (x_i - x_j) + \Omega_{ij}^2 (x_i - x_j)^2 \dots \right] \quad (2.16)$$

The backgrounds of CALPHAD-programs are thermodynamic databases of two-, three- or four-component systems. With such a program systems of higher order can be calculated and the phase development simulated by e.g. changing temperature or chemical composition. By setting the boundary conditions such as chemical composition, pressure, temperature and the amount of substance the CALPHAD-program calculates the equilibrium of equation (2.12) and the phase diagram can be plotted. However, kinetic aspects cannot be considered [34].

In conclusion the practical use to predict the material behavior shall be discussed. Due to the high solidification rate in the atomization process, the material of the powder is far away from the equilibrium state. Because of that, the equilibrium calculations do not show the state of the materials for a certain temperature, but the tendency to which equilibrium state the non-equilibrium material aspires to [32].

For the calculation of phase transformations, thermodynamic software Thermo-Calc[®] version 3.0 [36] with the database TCFE6.2 for iron based alloys [37] was used. The chemical composition as shown in table 2 was used for the calculations.

3 Results

3.1 Analysis of the as-received state

In figure 11 the particle size distribution of the investigated powder is shown.

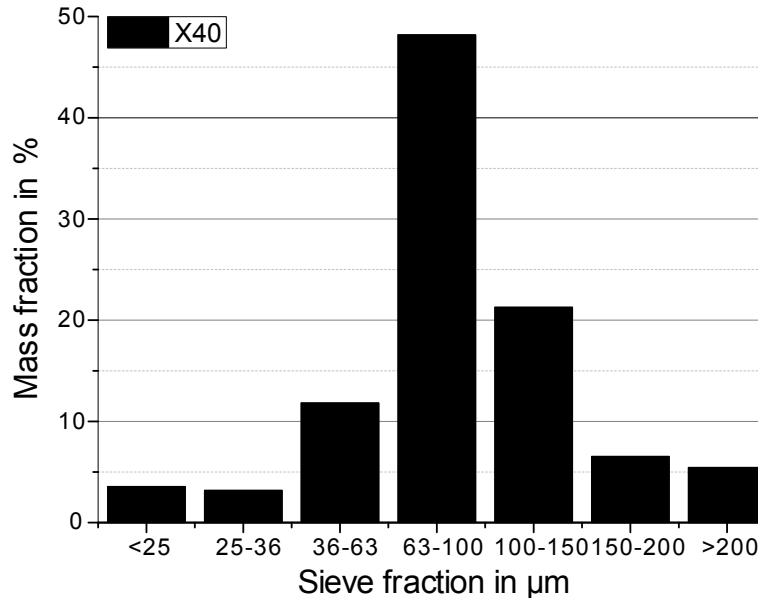


Figure 11: Particle-size distribution of the X40 powder. The fraction of the total mass is plotted against the particle-size fraction

The X40 shows a Gaussian-like distribution of the particle sizes with almost half of the powder mass having a particle-size between 63 and 100 μm . The exact values can be found in table 4 in the appendix.

3.1.1 Scanning Electron Microscopy

In figure 12 the appearance of the powder particles of the X40 can be seen. They have a spherical shape and the dendritic structure can be seen clearly on the surface (see a) and b)). In c), d) and e) a typical example of the appearance of the surface of this powder is shown. Small particles with the size below 1 μm can be found on the powder surface, which are most probably very fine particles of the same composition. At high magnifications (see f)) also very small, flaky shaped particulates are visible with the size below 100 nm, but most of the powder surface is rather clean. The particulates are too small to be measured by EDX.

Comparison of the spectra between the interdendritic and dendritic areas revealed that the interdendritic areas are enriched in chromium, molybdenum and vanadium (see figure 13). These segregations can also be seen in the cross-sections.

Figure 14 and figure 15 show cross-sections of the X40 after polishing with OPS. In the microstructure pores and bright particulates of submicron size can be found. Quite often the pores appear close to the particulates. EDX point-analyses make clear that the brighter particulates are enriched in chromium, molybdenum and vanadium (see figure 14), whereas the pores are also enriched in silicon and manganese (see figure 15). Each SEM result was confirmed statistically by observation in a number of sites.

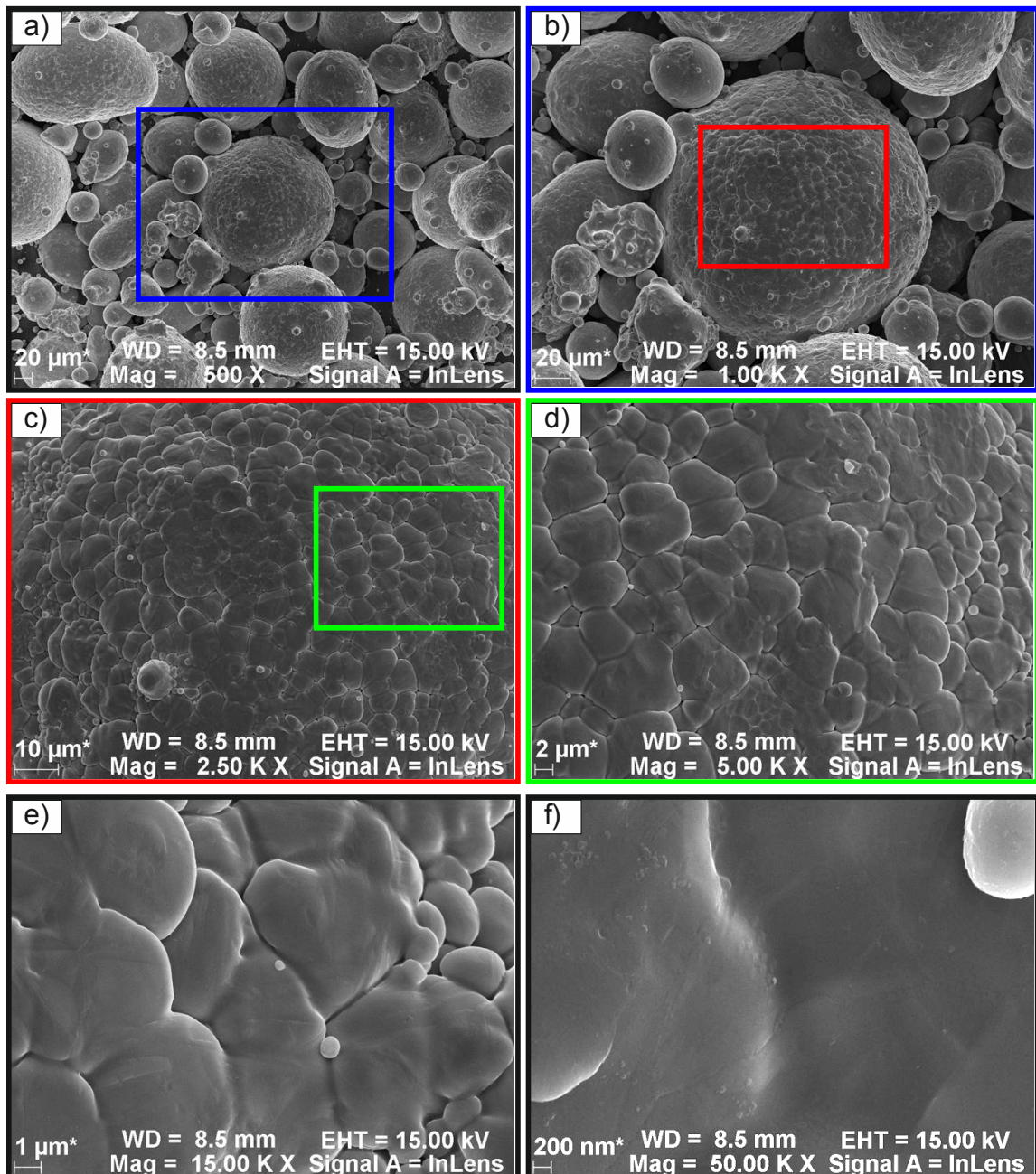


Figure 12: Overview of the appearance of the X40 powder studied

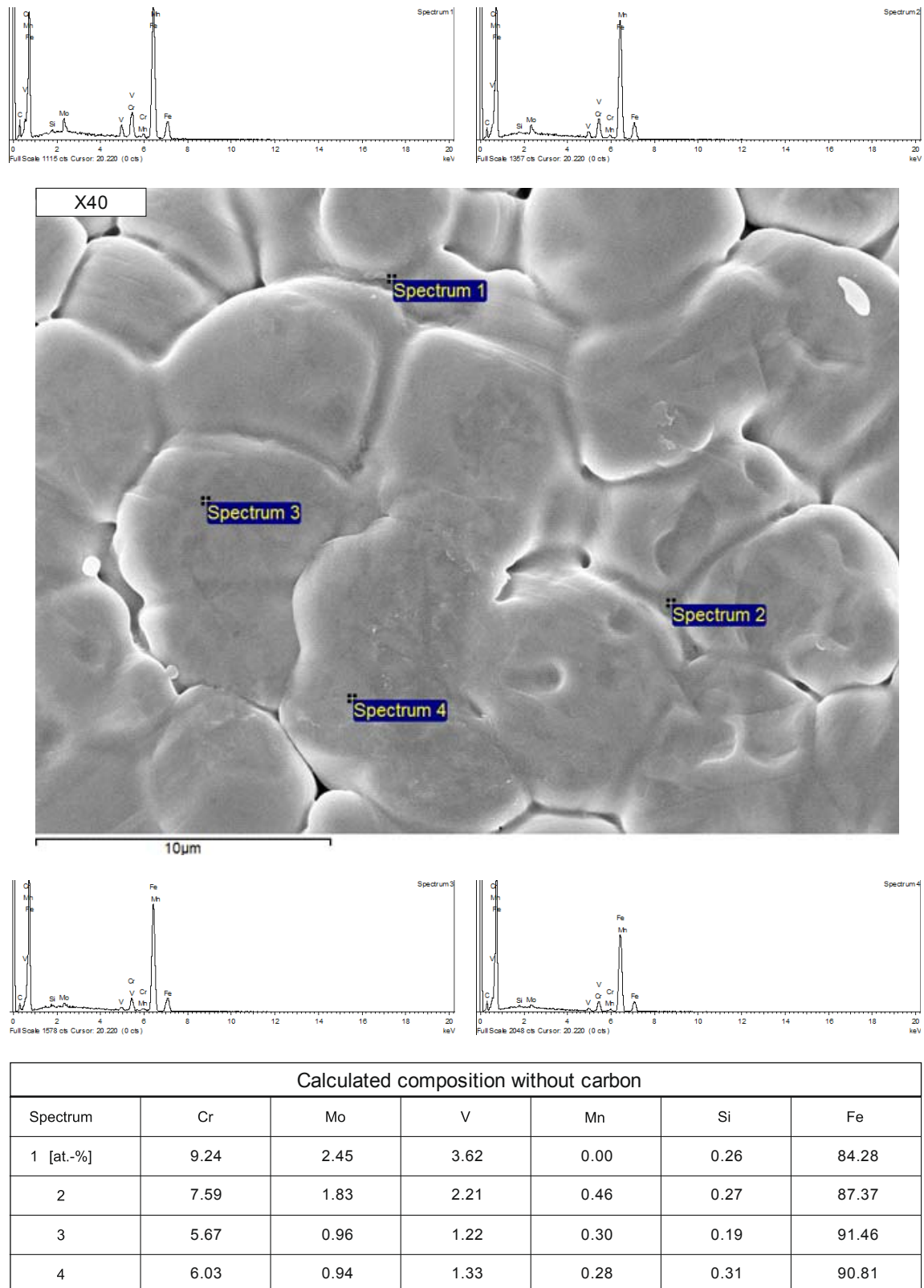
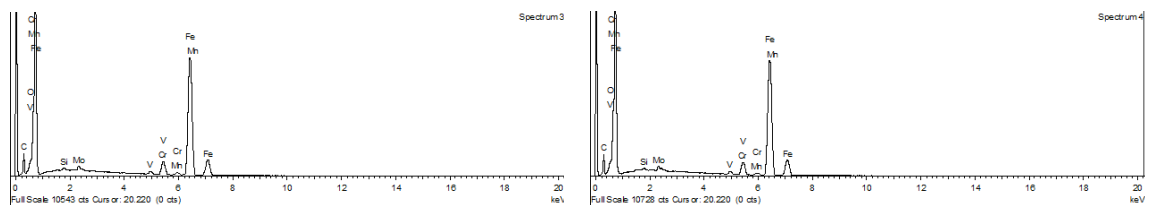
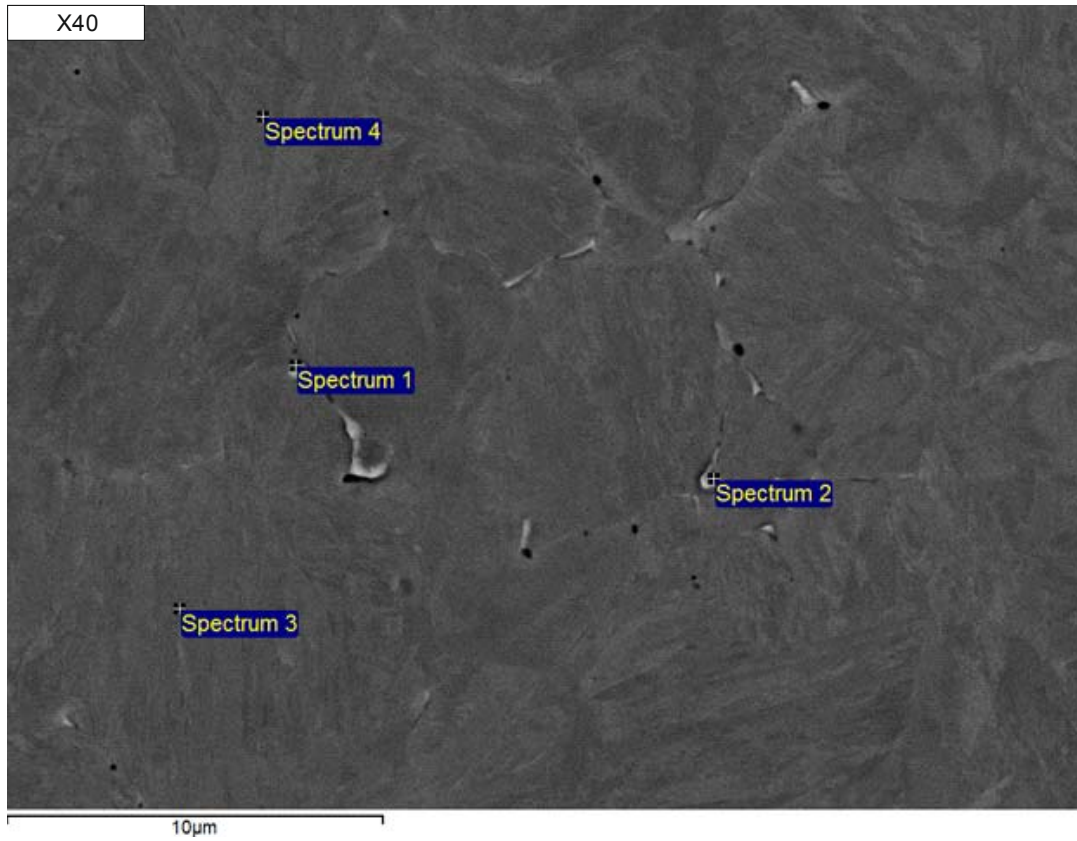
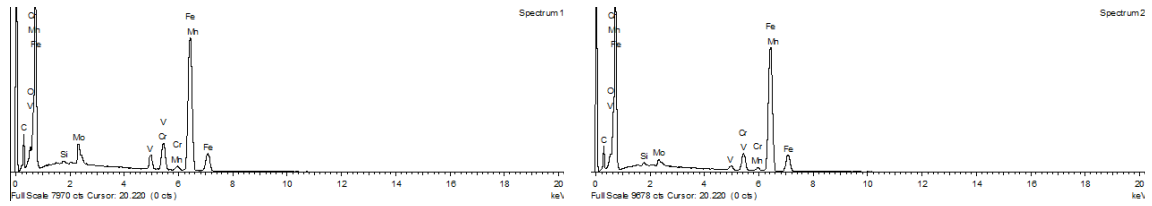
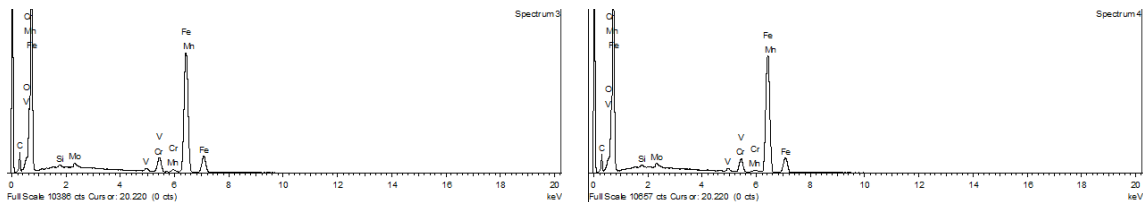
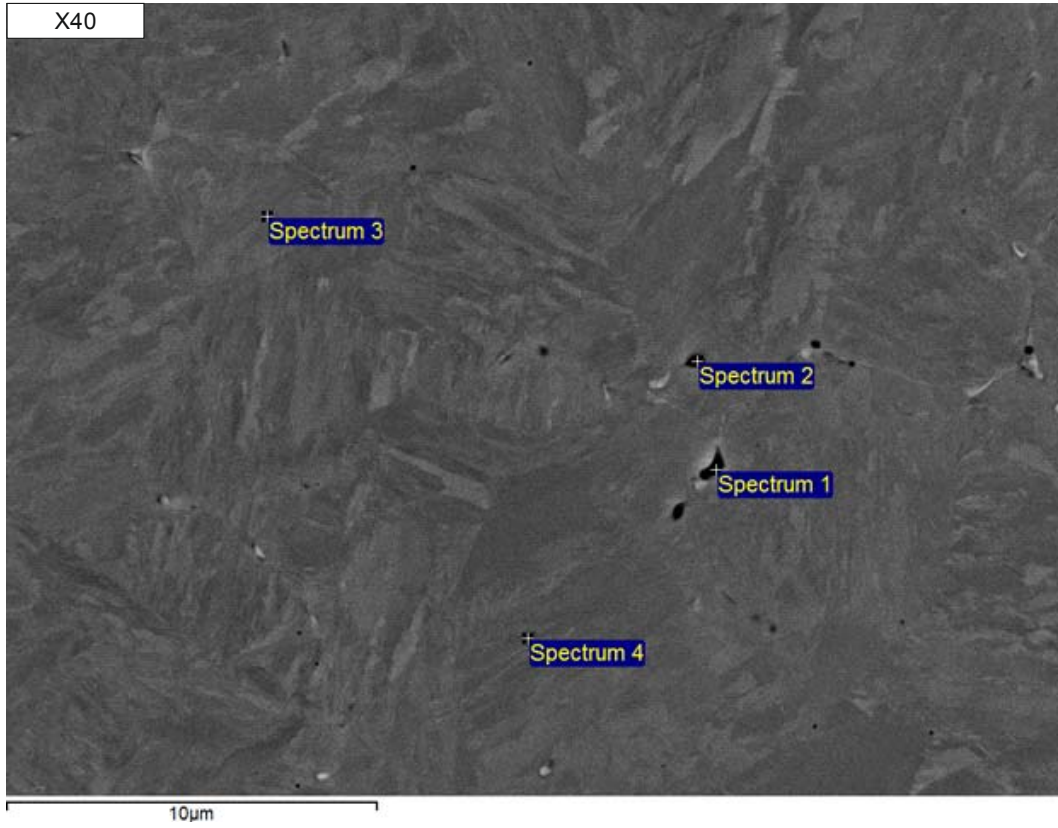
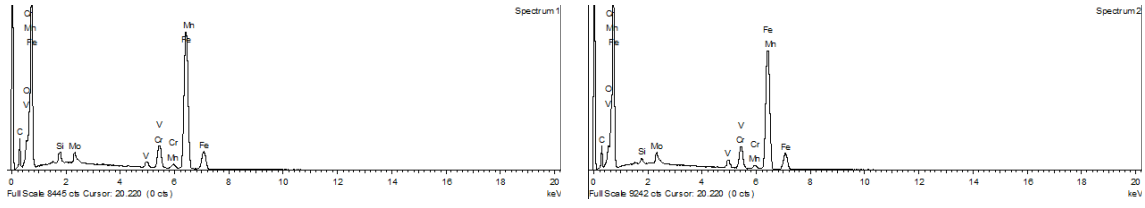


Figure 13: EDX analysis of the interdendritic areas on the powder surface of the X40. Spectra 1 and 2 - analysis of the interdendritic area and spectra 3 and 4 of the dendritic area



Calculated composition without carbon						
Spectrum	Cr	Mo	V	Mn	Si	Fe
1 [at.-%]	9.11	3.46	4.69	0.29	0.58	81.86
2	6.59	1.28	1.50	0.30	0.54	89.80
3	5.38	0.85	0.97	0.45	0.50	91.86
4	5.52	0.82	0.96	0.29	0.49	91.92

Figure 14: EDX analysis of a cross-section of the X40 powder. Spectra 1 and 2 analyze brighter spots and spectra 3 and 4 analyze the matrix material. BE-contrast was used for the picture



Calculated composition without carbon						
Spectrum	Cr	Mo	V	Mn	Si	Fe
1 [at.-%]	8.16	1.76	1.77	0.42	2.20	85.69
2	8.55	2.18	2.72	0.40	1.10	85.06
3	5.63	0.90	0.98	0.26	0.46	91.76
4	5.47	0.88	0.98	0.34	0.51	91.83

Figure 15: EDX analysis of a cross-section of the X40 powder. Spectra 1 and 2 analyze pores and spectra 3 and 4 analyze the matrix material. BE-contrast was used for the picture

3.1.2 X-ray Photoelectron Spectroscopy

Chemical composition

For the as-received state, measurements for the powder mounted on an aluminum plate and a carbon tape were performed. This was done to be able to evaluate the influence from different powder supports and hence possible contaminations. In figure 16 and figure 17 the development of the element content over the etch depth is shown. The exact values can be found in table 5 and table 6 in the appendix.

On the outermost surface there is a strong contamination by carbon. After ion-etching of 1 nm (Al-plate) respectively 3 nm (C-tape) the carbon content decreases strongly and stays on the same level for the other etching steps. But the measured carbon content is about five times higher for the powder mounted on carbon tape as for the powder pressed on aluminum. The developments of all the other elements are the same in both measurements, but the content of all the other elements is slightly lower in the powder measured on carbon tape due to the higher percentage of carbon. Therefore, the measurement on the aluminum plate will be described in more details.

The oxygen content decreases over all etching steps from about 54 at.-% on the outer most surface to ~7 at.-% after 50 nm of etching. Sulfur is enriched on the top surface showing a content of ~1 at.-%. Its content decreases with etching and cannot be detected after 10 nm of etching. Nitrogen can only be detected at the outermost surface below 1 at.-%. Silicon was not detected at all.

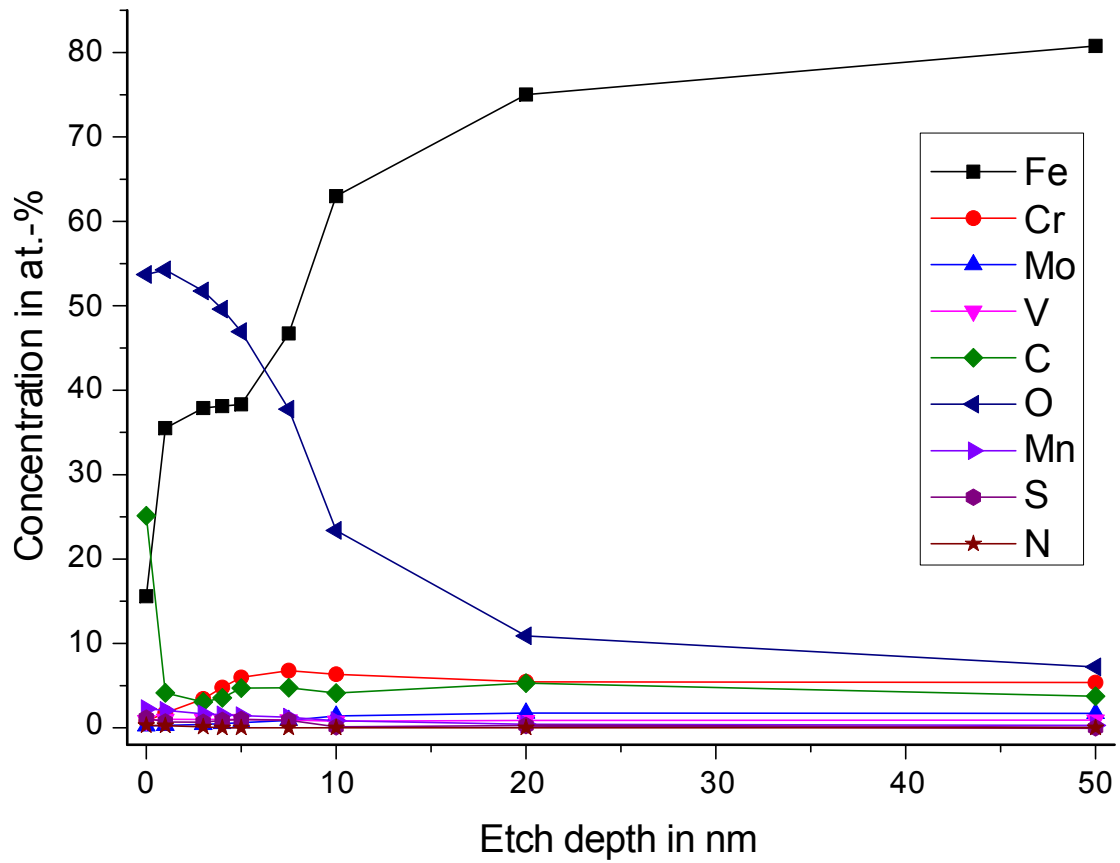


Figure 16: Element content over etch depth in the as-received state; powder mounted on aluminum plate

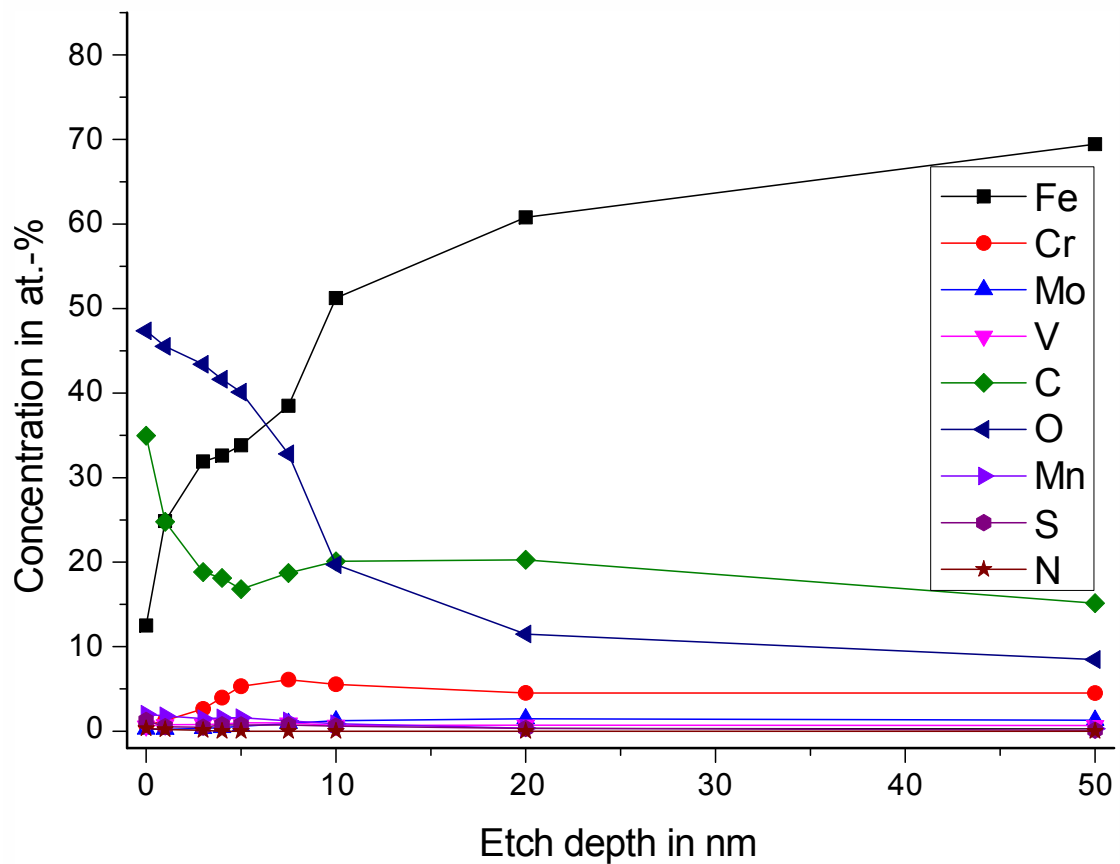


Figure 17: Element content over etch depth in the as-received state; powder mounted on carbon tape

To analyze the development of the metallic elements, the non-metallic elements have been suspended and the content was normalized to 100 % again. The associated plots can be seen in figure 18 and figure 19. The figures show that manganese is very much enriched in the outermost surface, reaching a content of ~ 12 at.-% and decreases constantly with etching to below 1 at.-% after 50 nm of etching. Vanadium is also enriched in the outer layer but varies only slightly over all etching steps between 4 at.-% in the outermost layer and 1 at.-% after 50 nm of etching. The chromium content is rather low in the outermost layer of ~ 4 at.-%, but is enriched in the range of 3 - 10 nm depth with a maximal content of 14 at.-% after 7.5 nm of ion etching. Its content decreases to about 6 at.-% with further etching. The molybdenum content is lower in the outer layers than after etching and shows its lowest content of below 1 at.-% after 1 nm of etching and its highest of 2 at.-% after 20 nm of etching. The iron content is low in the outermost surface with 78 at.-%. It increases after 1 nm of etching but decreases with further etching. After 7.5 nm of etching it increases again to 91 at.-% after 50 nm of etching. Silicon could not be detected in the as-received state.

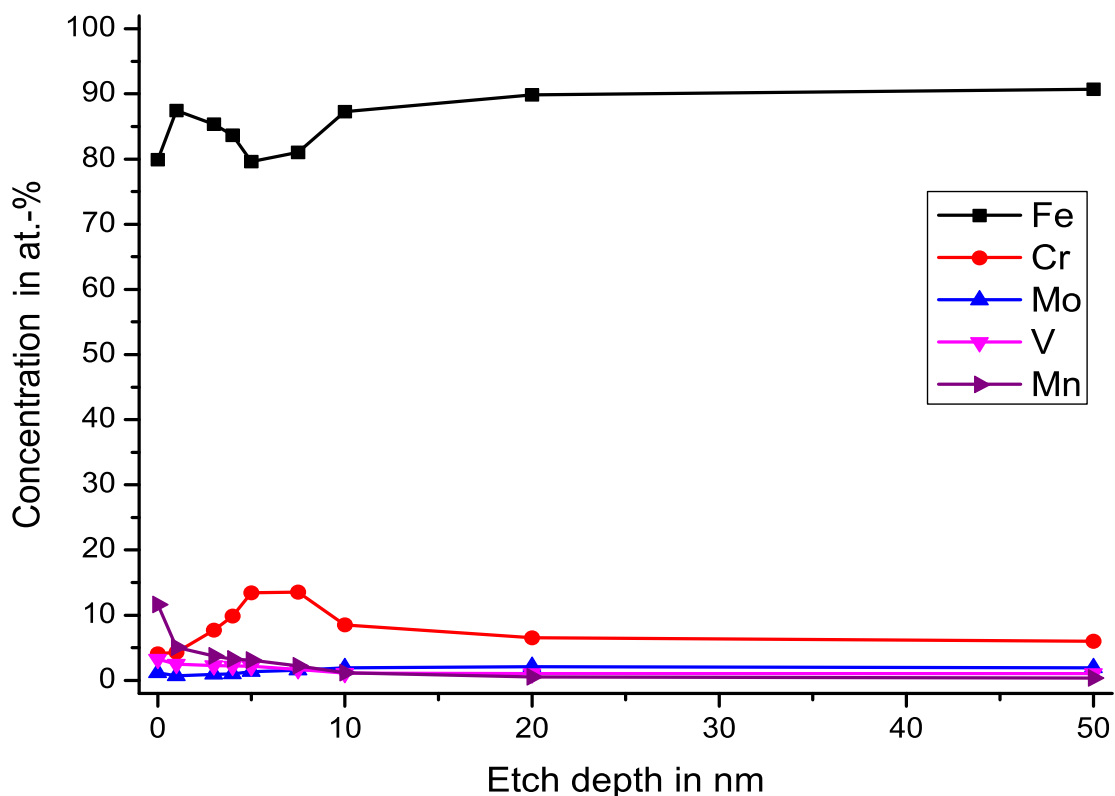


Figure 18: Relative concentration of the metallic elements over the etch depth in the as-received state; powder mounted on aluminum plate

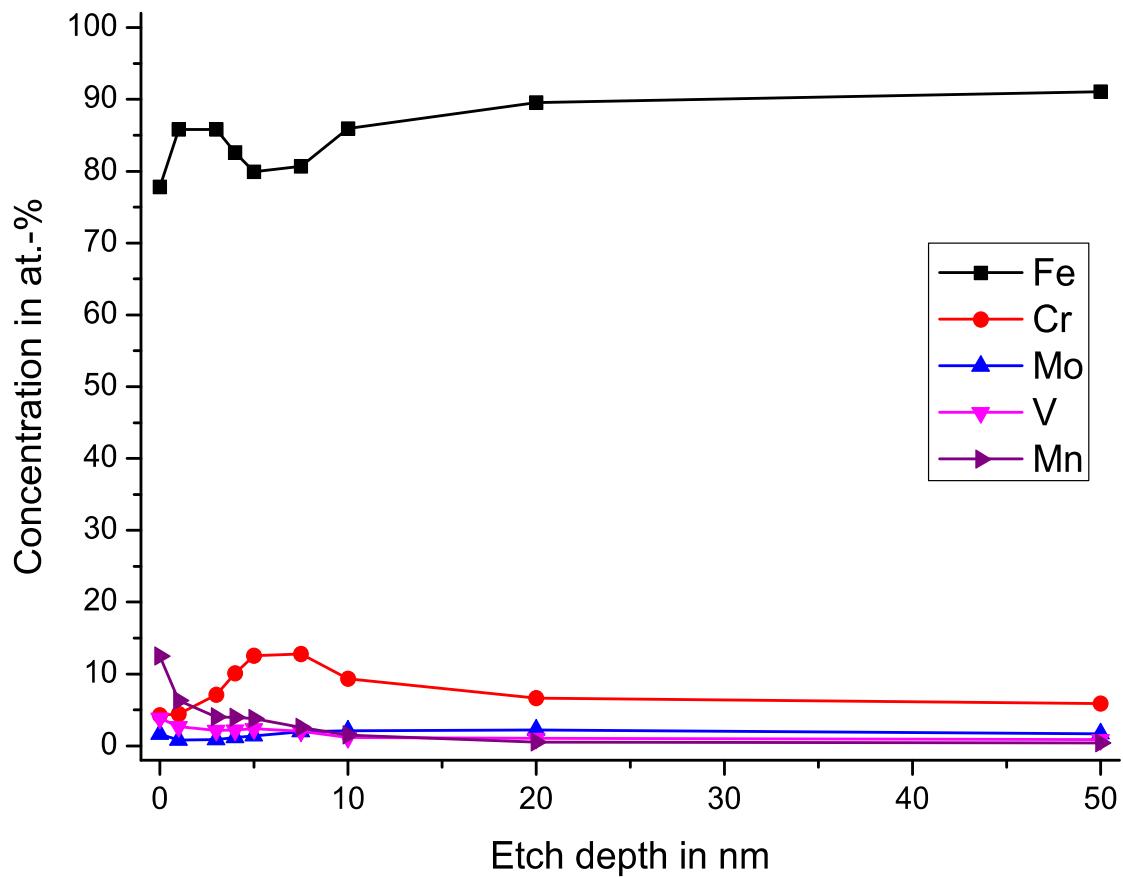


Figure 19: Relative concentration of the metallic elements over the etch depth in the as-received state; powder mounted on carbon tape

Chemical state

High resolution narrow scans have been used to analyze the chemical state of the metallic elements. The pressing into the aluminum plate can lead to partial removal of the surface layer in the locations of inter-particle contacts during pressing. This leads to thinner surface layers and thus appearance of metallic signal on the spectra. As this has no actual physical meaning, the measurements of powder mounted on carbon tape are used to evaluate the chemical state of the unannealed powder, since this problem does not occur here.

Figure 20, figure 21 and figure 22 show narrow spectra of iron, chromium and manganese peaks for the powder after 1 nm of etching, which corresponds to the removal of surface contaminations, and after 7.5 nm and 50 nm of ion etching for the powder mounted on the carbon tape.

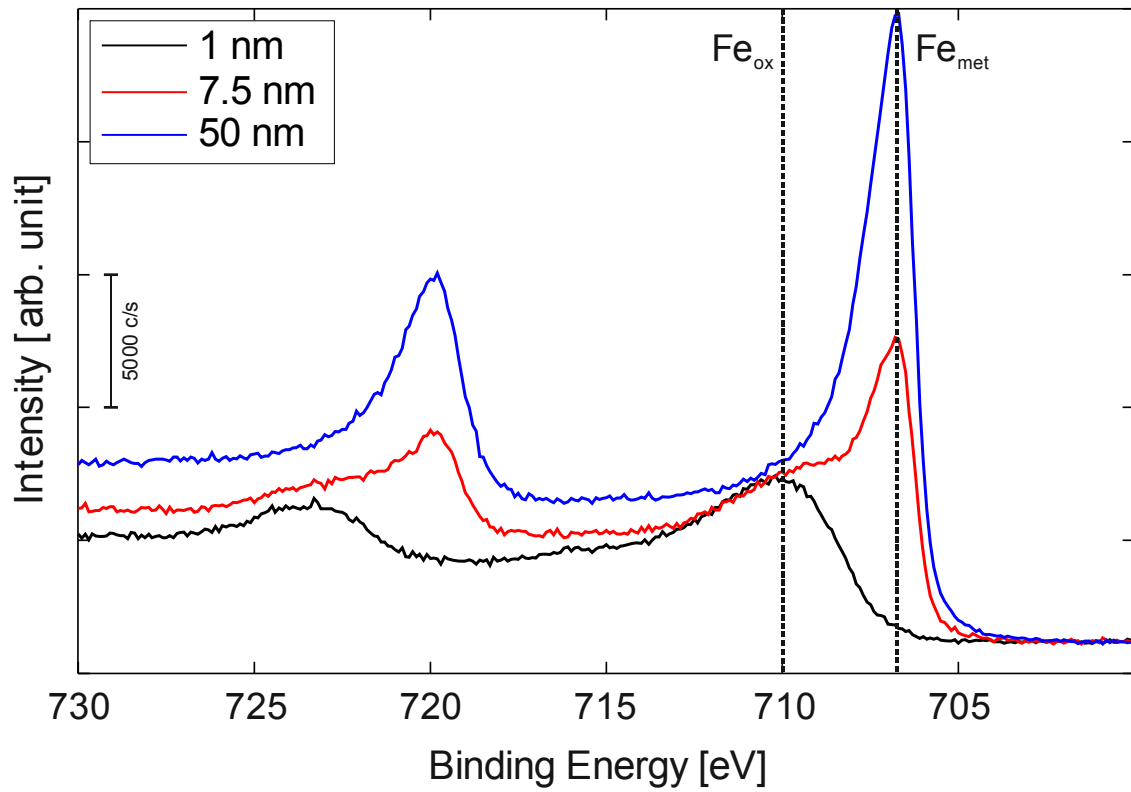


Figure 20: Detailed XPS spectra of Fe 2p after 1 nm, 7.5 and 50 nm of ion etching; powder mounted on carbon tape

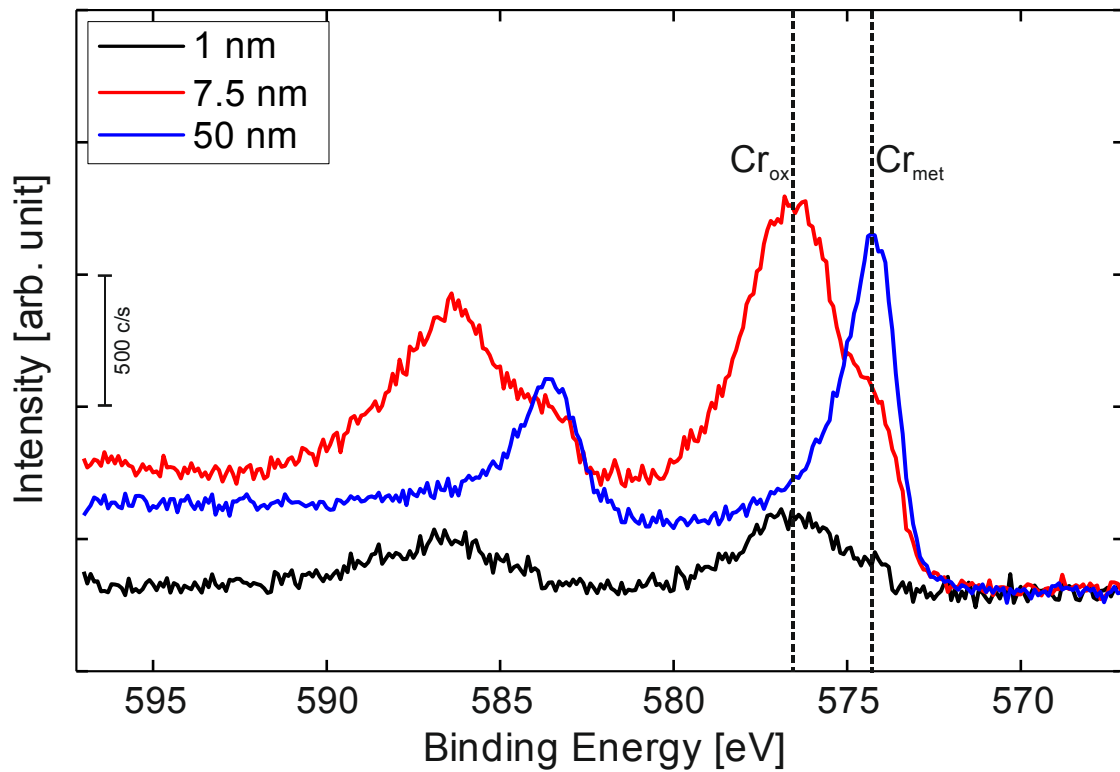


Figure 21: Detailed XPS spectra of Cr 2p after 1 nm, 7.5 and 50 nm of ion etching; powder mounted on carbon tape

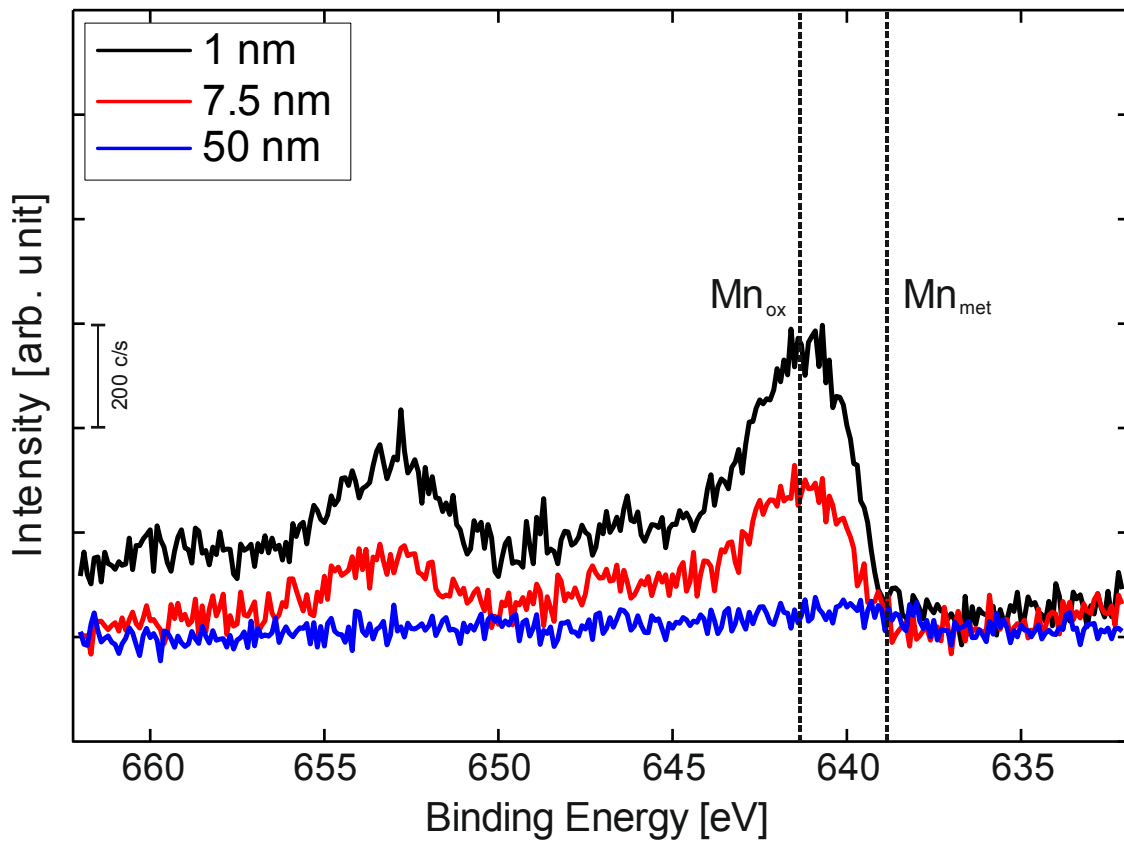


Figure 22: Detailed XPS spectra of Mn 2p after 1 nm, 7.5 and 50 nm of ion etching; powder mounted on carbon tape

The narrow scans for vanadium and molybdenum are shown in figure 23 and figure 24, respectively. It can be seen that for none of the metallic elements a metallic peak is detectable in the as-received state. After 7.5 nm of etching the metallic peak is the major peak for iron and the minor peak for chromium. Manganese is still fully oxidic. Iron and chromium are completely metallic after 50 nm of etching. However, in case of manganese only traces can be detected after 50 nm of etching. Vanadium does not show any metallic signal for all etching steps. The peak shifts to lower energy levels with increasing etch depth. But the peak position is still slightly too high to indicate a metallic state.

The signal of molybdenum is quite weak in the narrow scan after 1 nm of etching. However, the ratio of the Mo 3d_{5/2} and Mo 3d_{3/2} peaks gives a hint about some molybdenum oxides. This is due to the fact that the peaks of the metallic state of Mo 3d_{3/2} and of the oxidic state of Mo 3d_{5/2} overlap. For the pure metallic state the ratio of the Mo 3d_{5/2} and Mo 3d_{3/2} peaks is about 3:2. But after 1 nm of etching the ratio is about 1:1. A closer look reveals that at this binding energy range also the sulfur S 2s peak is located at 229 eV. Also no oxidic signal of Mo 3d_{3/2} can be seen. Hence, the spectrum shows the overlap of the Mo 3d_{5/2} and S 2s peak, the later one being dominant. However, the signal of molybdenum is quite weak in the as-received state and probably derived from underneath the oxide layer.

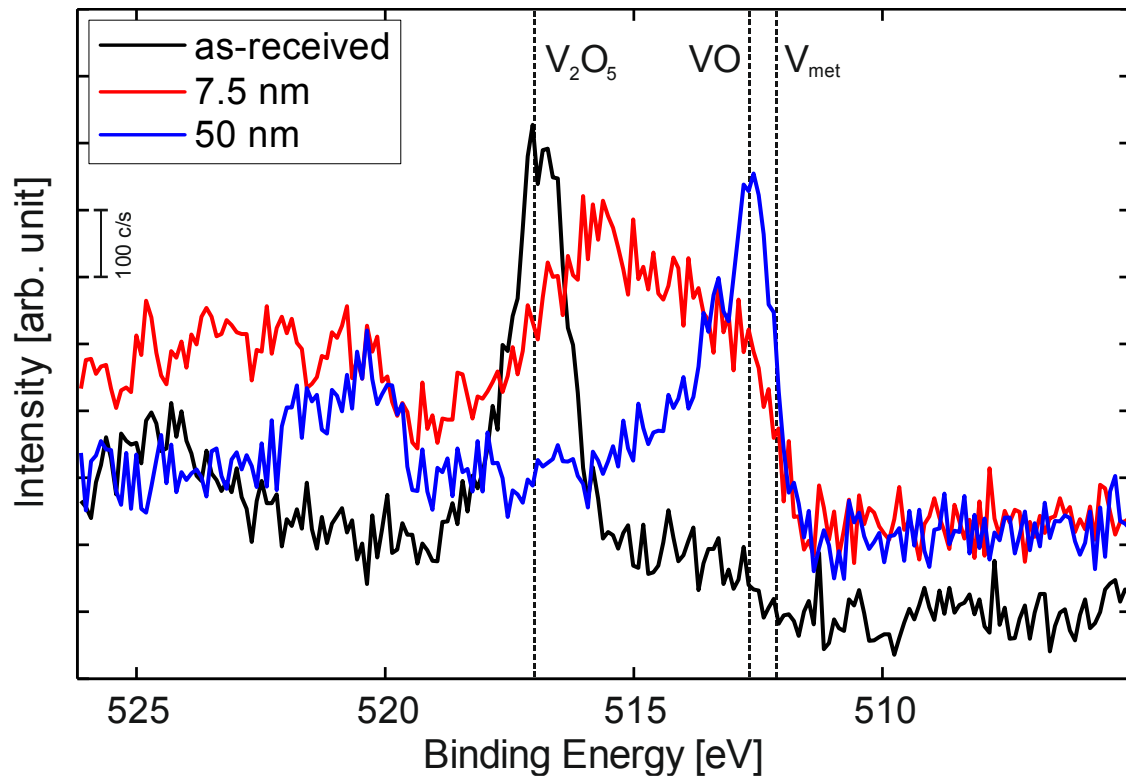


Figure 23: Detailed XPS spectra of V 2p in the as-received state and after 7.5 and 50 nm of ion etching; powder mounted on carbon tape

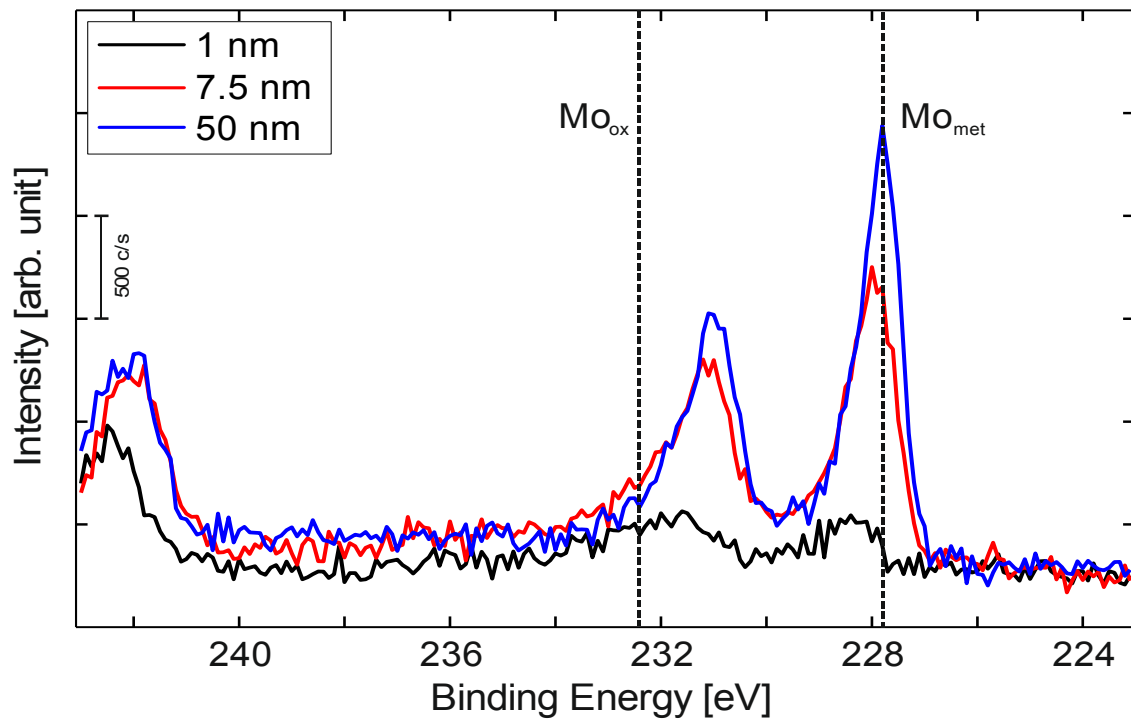


Figure 24: Detailed XPS spectra of Mo 3d after 1 nm, 7.5 and 50 nm of ion etching; powder mounted on carbon tape

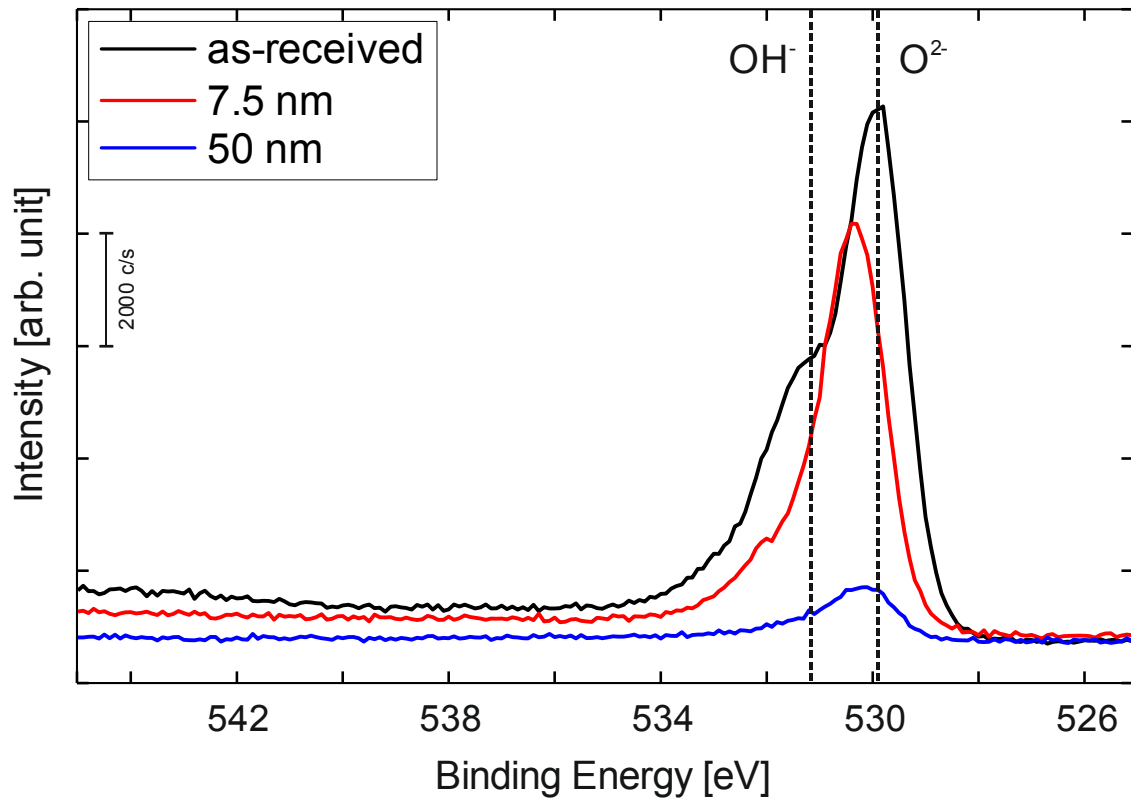


Figure 25: Detailed XPS spectra of O 1s in as received state and after 7.5 and 50 nm of ion etching; powder mounted on aluminum plate

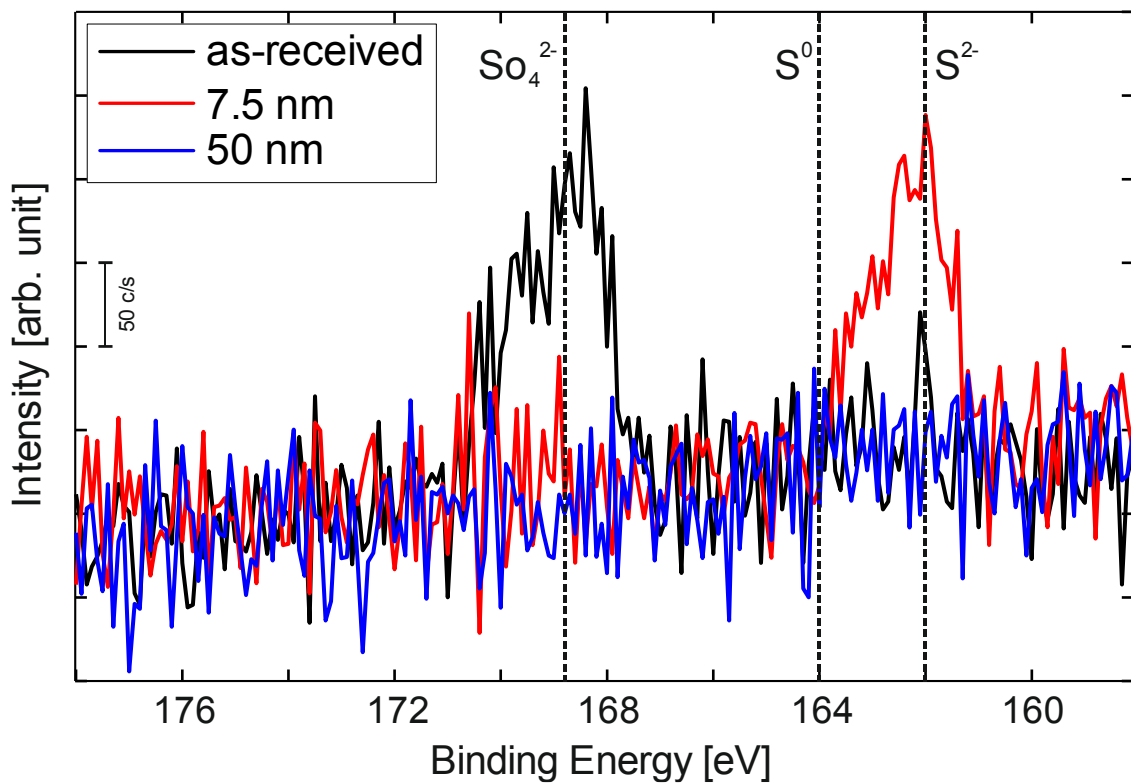


Figure 26: Detailed XPS spectra of S 2p in as received state and after 7.5 and 50 nm of ion etching; powder mounted on aluminum plate

Besides the metallic elements, the non-metallic elements undergo changes in the chemical state, as well. The oxygen peak of the as-received state can be split into two main peaks (see figure 25). It is composed of O^{2-} which represents oxygen in metallic oxides and OH^- representing oxygen in hydroxides. However, the contribution from the hydroxyl group is removed after 1 nm of etching. Hence, it is only present as a top layer.

Sulfur is present in the SO_4^{2-} group in the as-received state. After removal of the contamination layer its binding energy shifts to lower binding energies which corresponds to some sulfides. After 50 nm of etching no sulfur can be detected.

To analyze the fraction of the elements in different chemical states, curve-fitting was performed for iron, chromium and manganese. This was not done for vanadium as it is fully oxidic at every etching step. However, different oxidic states can also be observed but this is most probably due to ion etching that leads to transformation of oxides [38]. Hence, after ion etching a quantitative analysis is not possible. Molybdenum does not show any changes in the chemical state indicating its presence in the metallic state from the beginning.

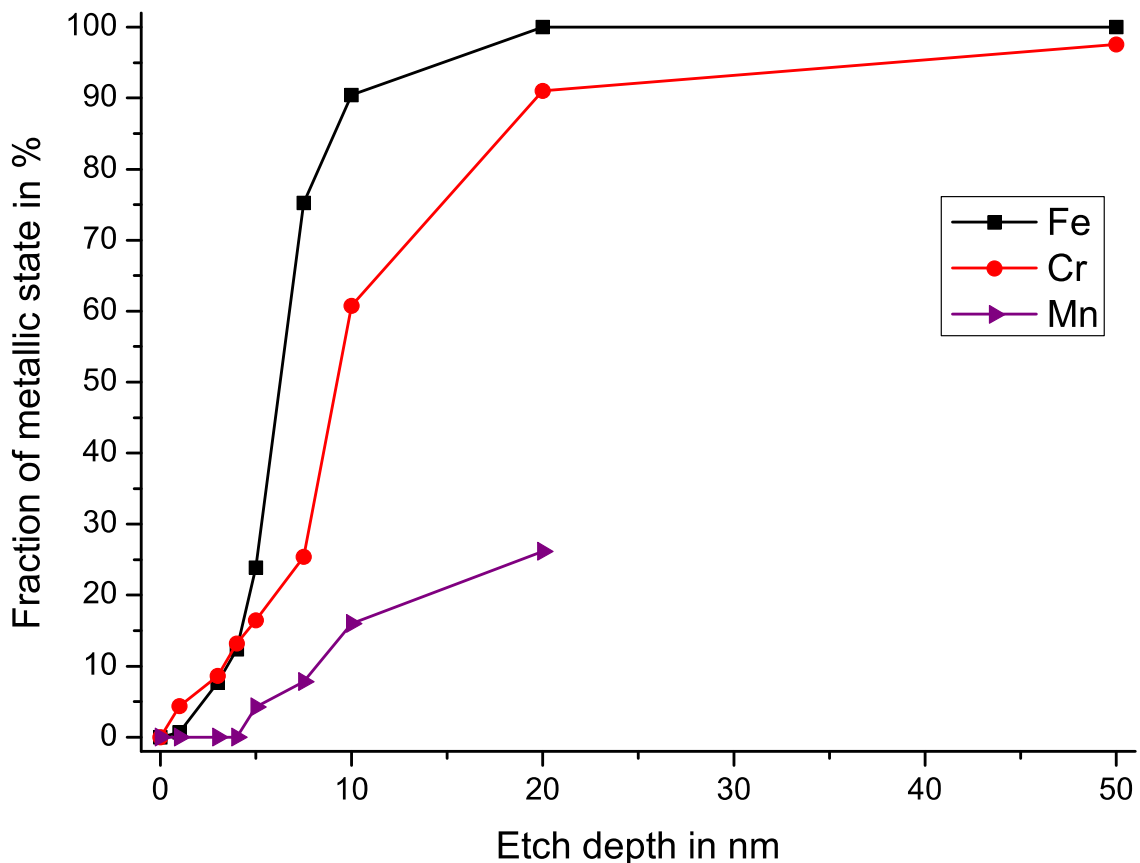


Figure 27: Fraction of the metallic state of Fe, Cr and Mn as a function of the etch depth; powder mounted on carbon tape

In figure 27 the fraction of the metallic state is plotted over the etch depth. In the outermost surface iron is fully oxidized. After etching, the metallic fraction increases with increasing etch depth until it is fully metallic at 20 nm depth. The trend for chromium is almost the

same as for iron, but with a smaller metallic part for etch depth over 4 nm. Manganese is fully oxidic in the first 4 nm. After 5 nm of etching a weak metallic signal can be detected which increases slightly after ion etching. The signal was too weak after 50 nm of etching to perform curve fitting.

Iron oxide layer thickness

The iron oxide layer thickness can be estimated by applying the relation between the normalized intensity of the iron metal peak and the etch depth. For an iron layer of uniform thickness, the layer thickness is about the depth where the metal intensity reaches 65 % [39].

Another method uses the oxygen intensity. It determines the oxide thickness as the etch depth where the oxygen intensity is decreased by half of the difference between its maximum and minimum intensities [19]. Both evaluation methods are shown in figure 28.

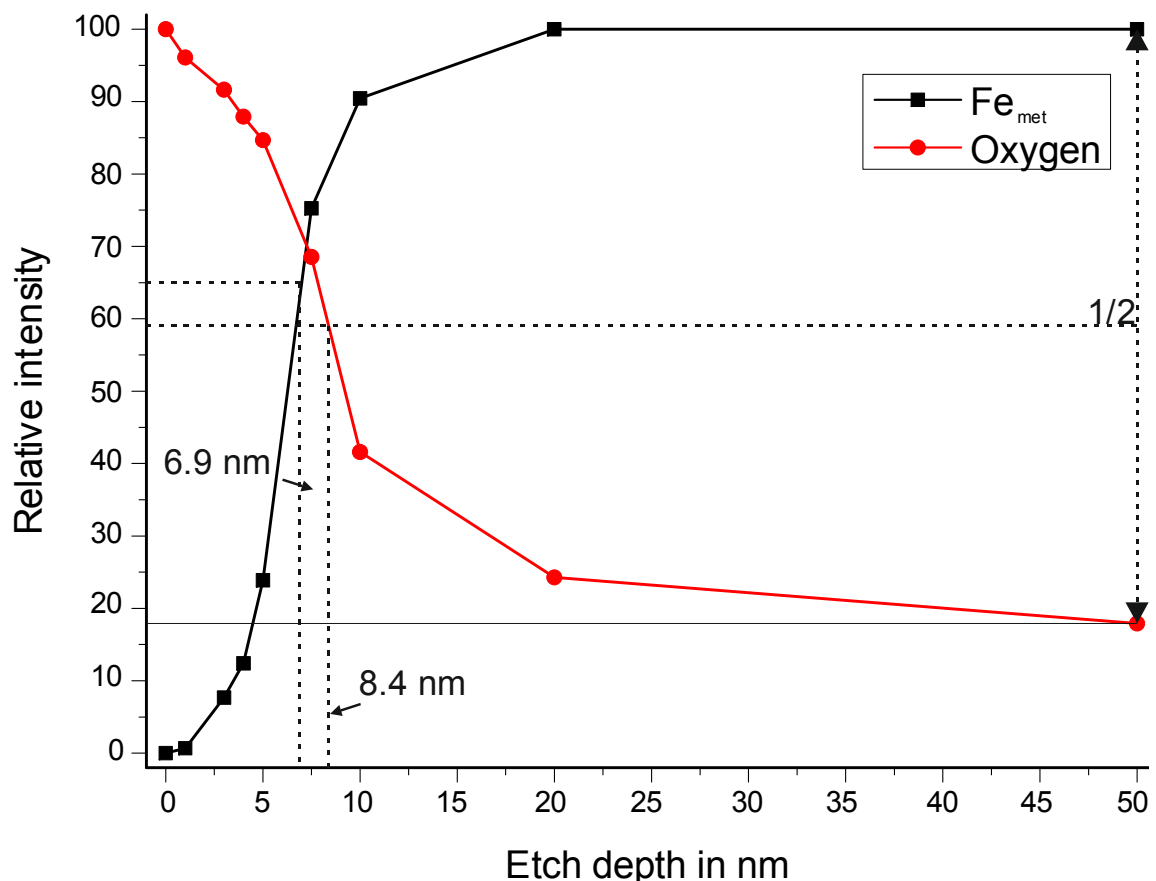


Figure 28: Estimation of the surface iron oxide layer for powder mounted on carbon tape by using the normalized intensities of metallic iron and the oxygen content as a function of the etch depth

The results of both evaluation methods are slightly different. Using the method utilizing the metallic iron intensity gives an iron oxide layer of about 7 nm. By using the oxygen relative intensity the oxide layer is estimated to be 8 nm thick. This difference appears because of the heterogeneity of the oxide compounds. Most of the oxides rich in chromium, manganese and vanadium are of a large size. This rises the oxygen content in

deeper etch depth. Therefore, the evaluation method using the oxygen intensity cannot be applied in case of the X40 powder.

Relative cation concentration

The relative cation concentration gives information about the composition of oxides. It is calculated from the fraction of the oxidic state of each element in relation to the relative concentration of the metallic elements. Figure 29 shows the relative cation concentration depending on the etch depth for the powder mounted on carbon tape. Until about 15 nm depth the main cation is iron - over 77 % in the outermost 5 nm. It decreases with higher etch depth to 0 % at 20 nm. In the outer layers the chromium cation fraction is rather small with 4 % at the outermost surface. But it enriches with increasing etch depth, with a maximum of 30 % after 20 nm of etching and then decreases again with further etch depth. Manganese is the second largest cation fraction in the outermost layer with 13 %. Nevertheless, after etching it stays on a rather low level but increases with larger etch depths with a maximum of 20 % at 20 nm. The vanadium cation content is very low for the outer layers but increases strongly after etching above 10 nm. After about 15 nm it is the dominant cation with a maximum fraction of ~71 % at 50 nm.

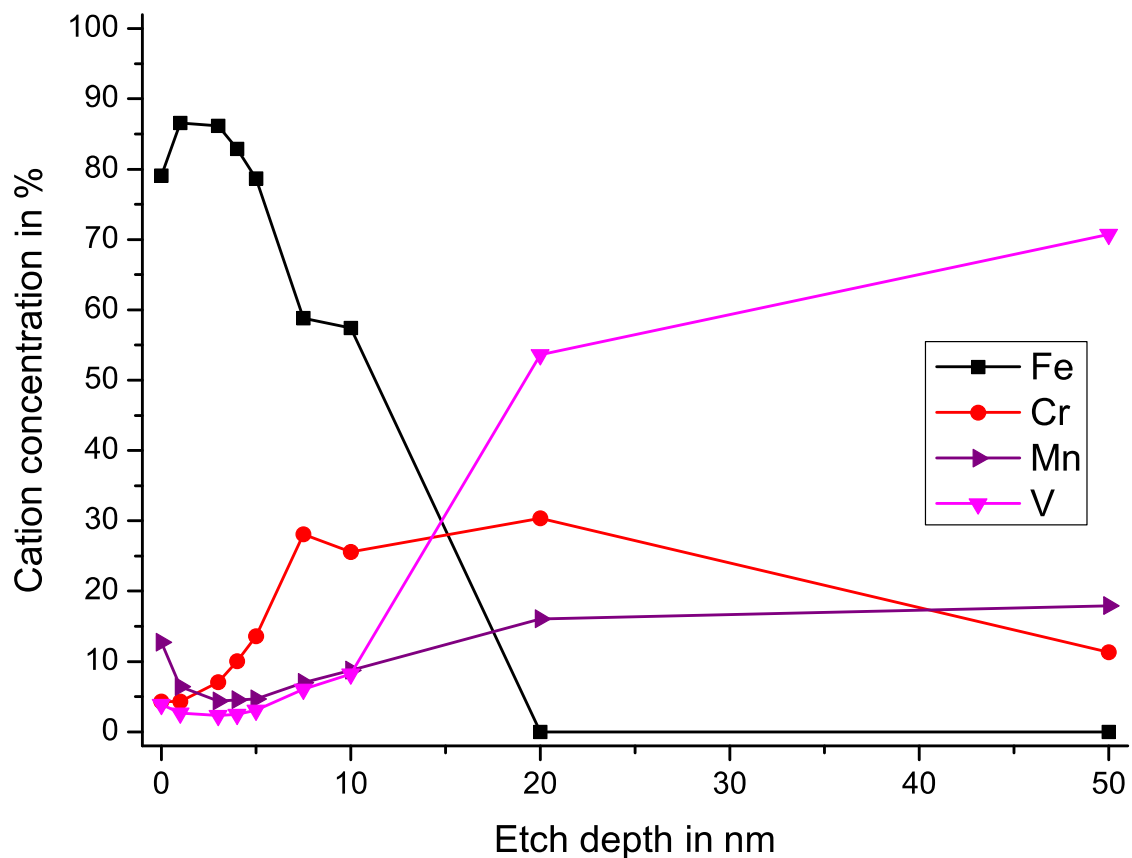


Figure 29: Relative cation concentration as a function of the etch depth, powder mounted on carbon tape

3.2 Analysis after heat treatment

3.2.1 Scanning Electron Microscopy

The specimens were analyzed in the SEM after XPS measurements. Consequently, slight oxidation due to exposure to air was unavoidable. But this leads mostly to formation of the iron oxide layer that cannot be detected by SEM and EDX. Each result was confirmed statistically by observation in a number of sites.

The differences observed on the powder surface after vacuum annealing at 500 °C are rather small compared to the un-annealed powder. The only remarkable difference is the appearance of a very few rectangular particulates with sizes below 200 nm which can be seen in figure 30. They could not be analyzed by EDX due to their small size.

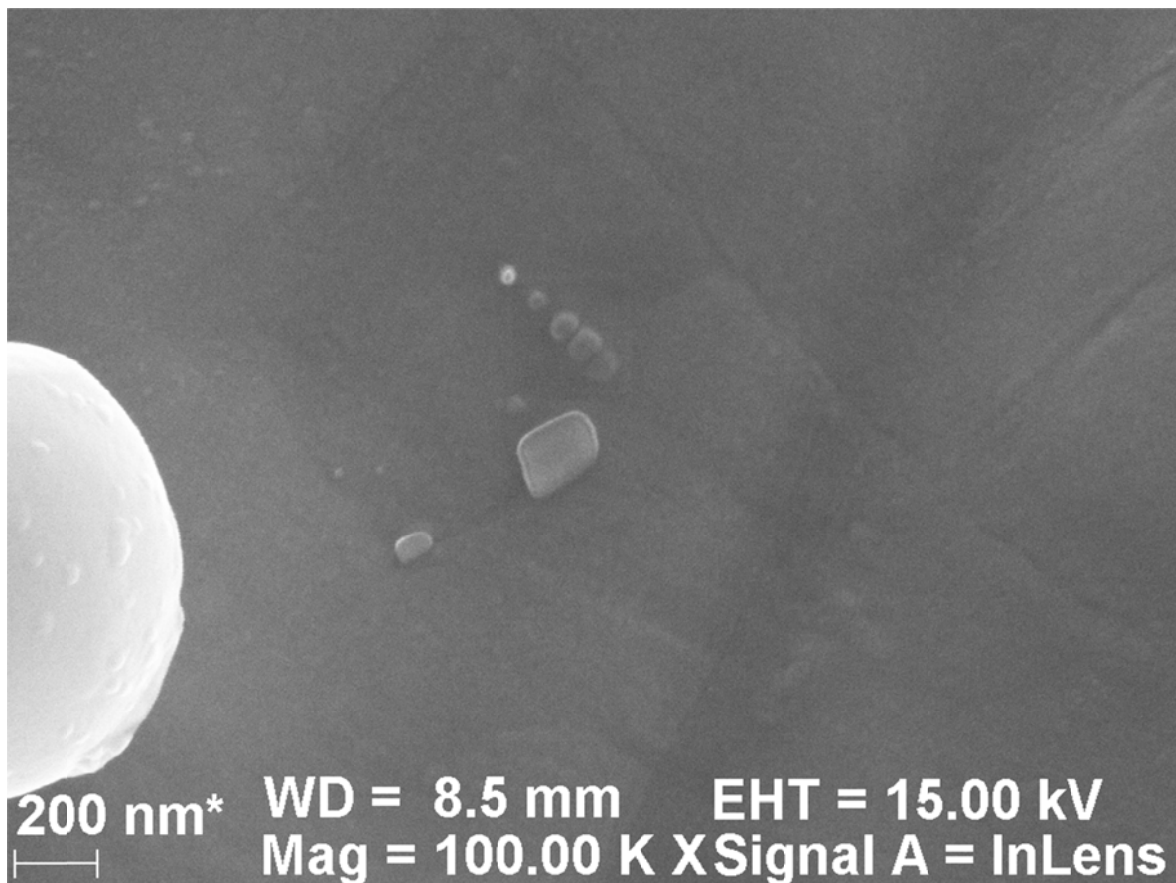


Figure 30: SEM image of rectangular particulates on the X40 powder surface after heat treatment at 500 °C in vacuum

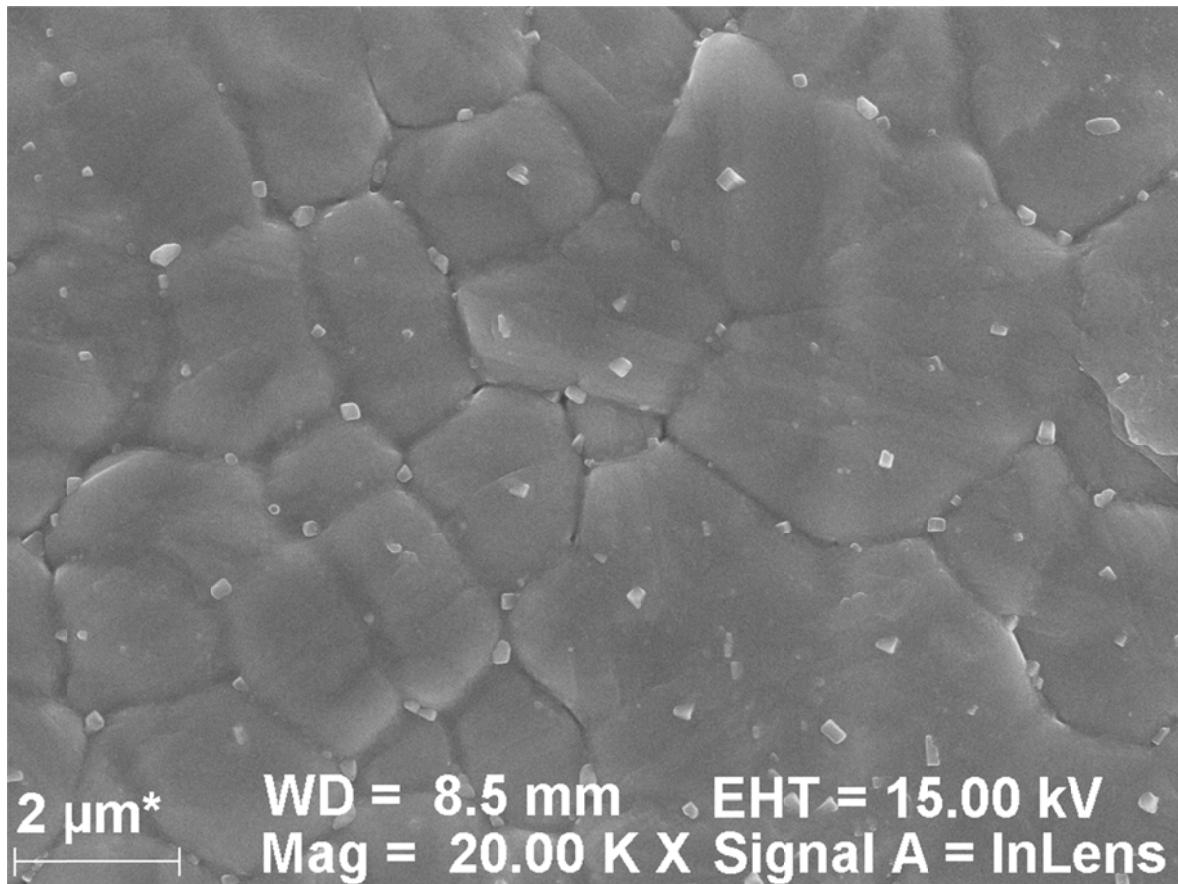


Figure 31: SEM image with an overview of rectangular particulates on the X40 powder surface after heat treatment at 600 °C in vacuum

The powder surface appearance changes considerably after vacuum annealing at 600 °C. All over the powder surface homogeneously distributed rectangular particulates can be found, which grow mainly in the interdendritic areas as can be seen in figure 31. The particulates have sizes of about 200 nm and grow out of the powder particle (see figure 32).

After annealing at 700 °C in vacuum still a lot of particulates are present on the powder surface as shown in figure 33. Their shape becomes more spherical but they are approximately of the same size as at 600 °C (see figure 34).

The amount of particulates becomes far less after annealing at 800 °C as can be seen in figure 35. Also the particulate shape changes to a more flaky structure. EDX analyzes revealed that some of those particulates are slightly enriched in manganese and others rich in aluminum (see figure 36 and figure 37). Besides that, very small, dark particulates can be found mainly in the interdendritic areas.

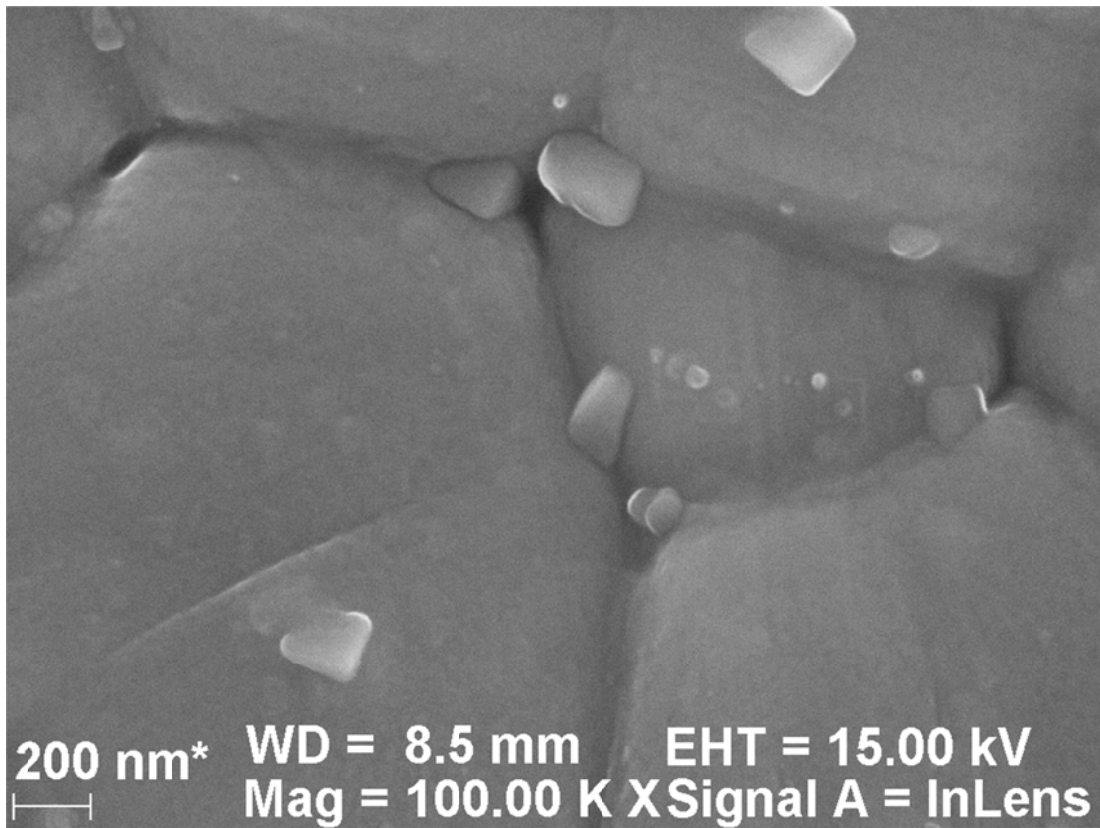


Figure 32: SEM image with a close-up of rectangular particulates on the X40 powder surface after heat treatment at 600 °C in vacuum

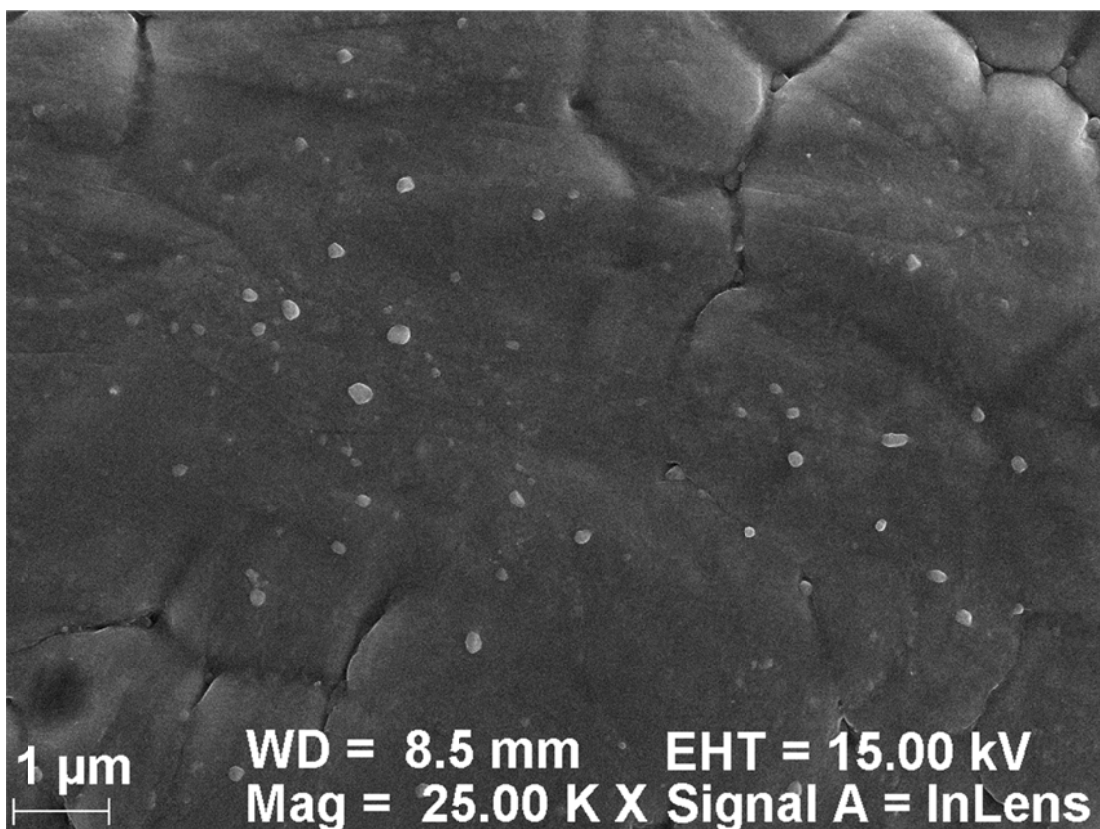


Figure 33: SEM image with an overview of particulates on the X40 powder surface after heat treatment at 700 °C in vacuum

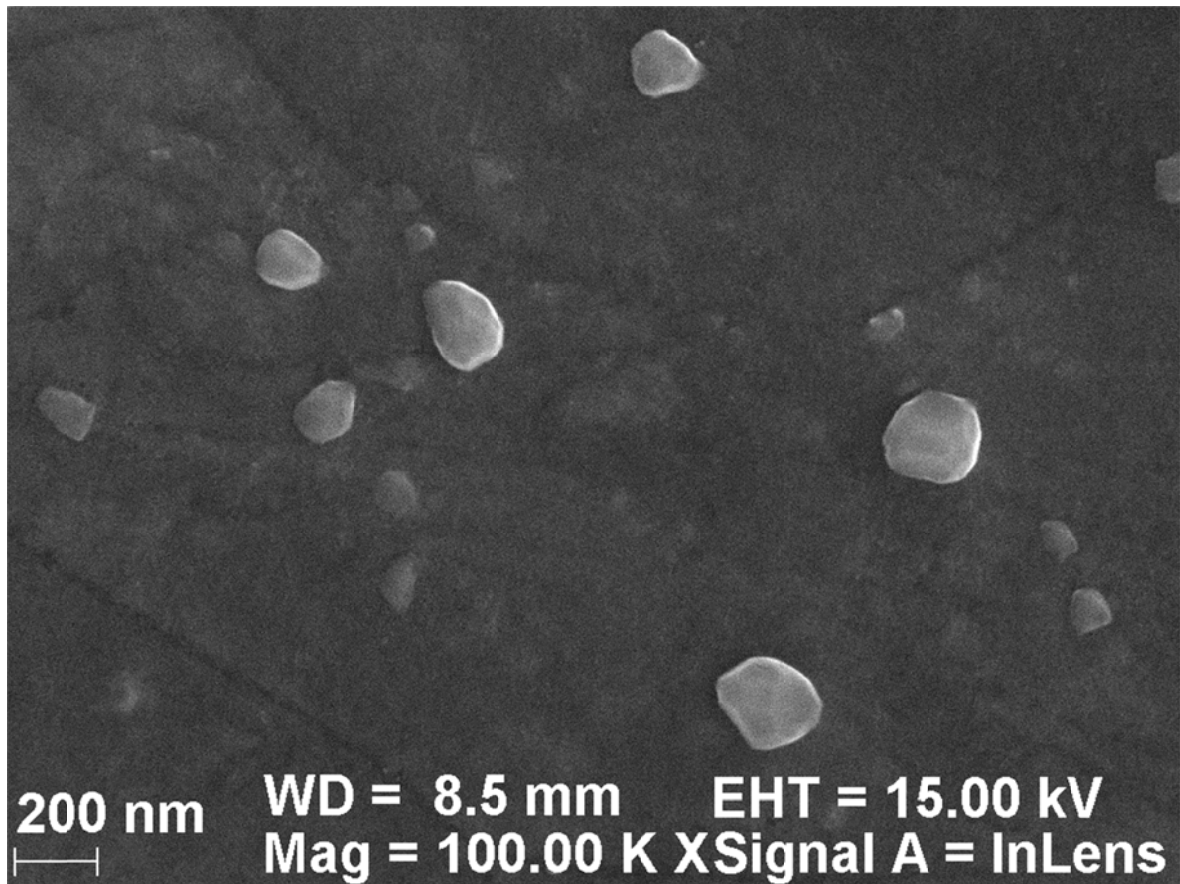


Figure 34: High magnification SEM image of the powder surface after heat treatment at 700 °C in vacuum

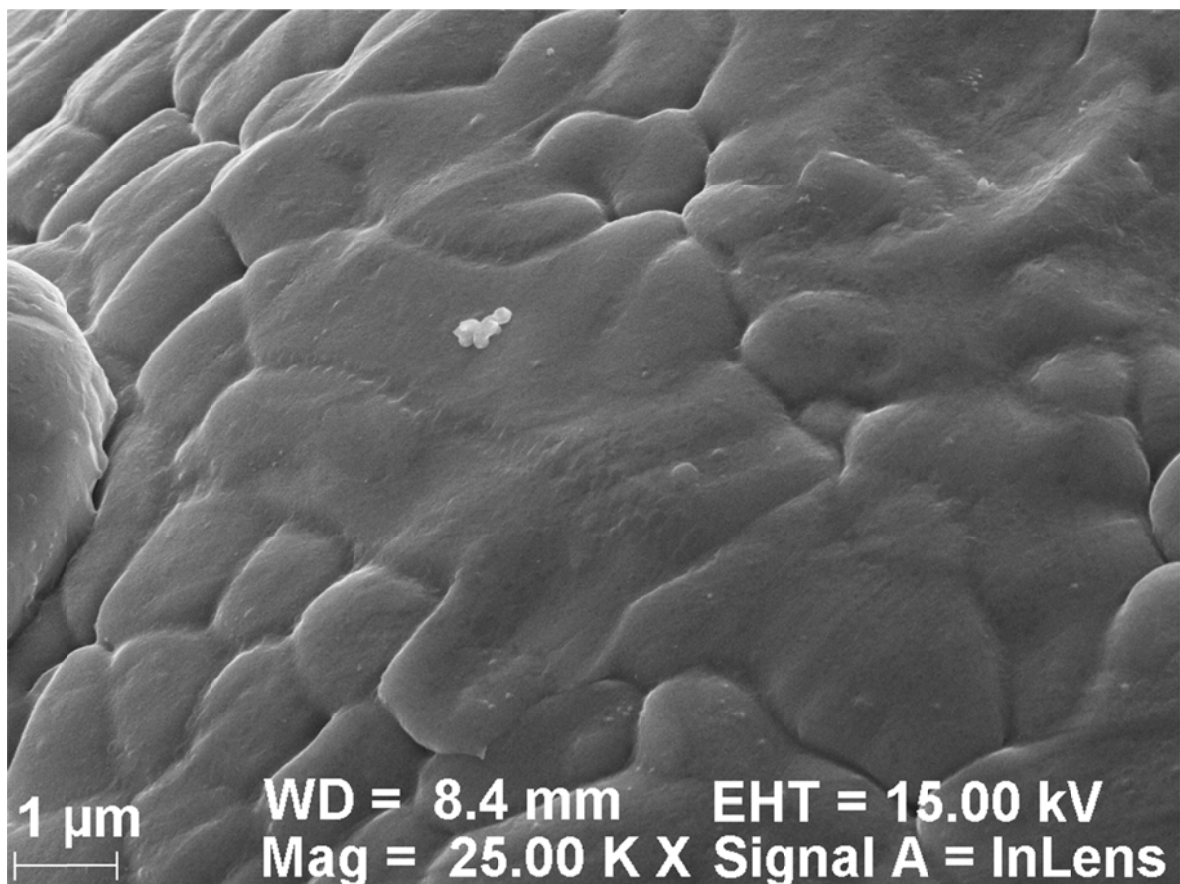
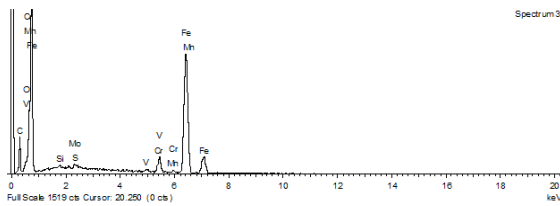
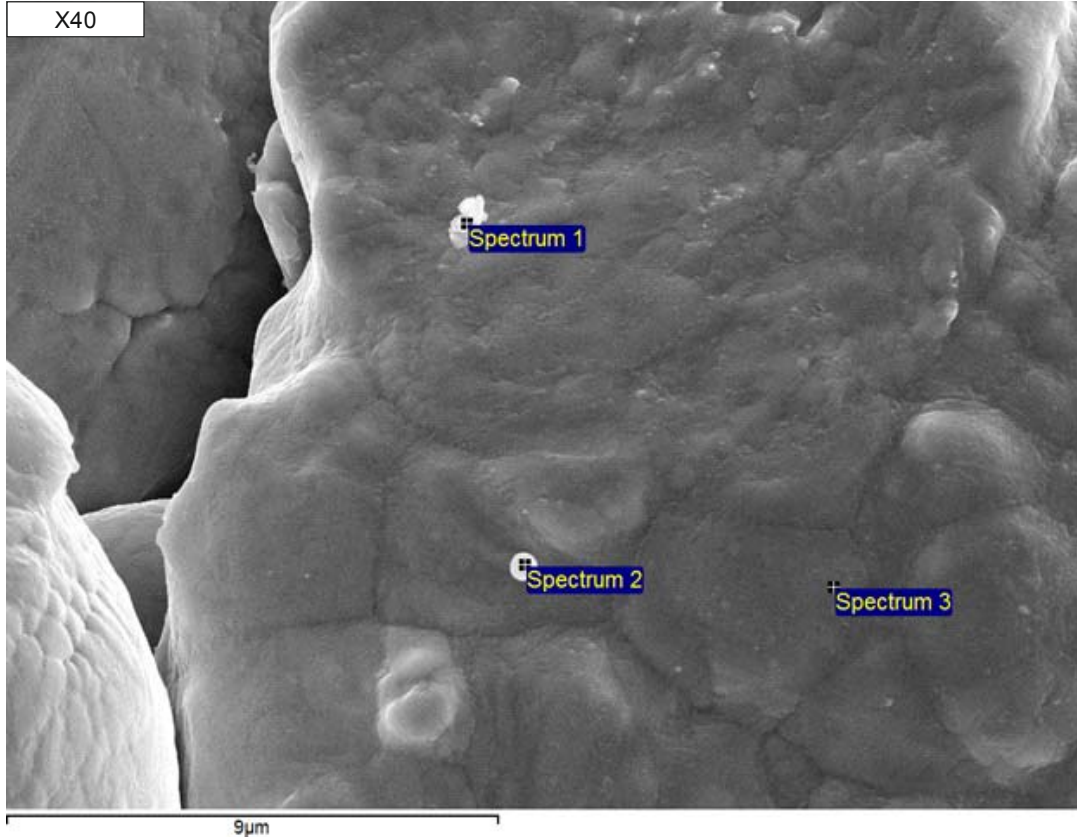
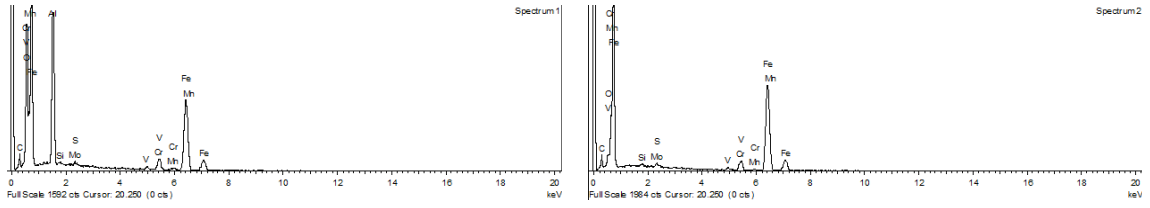
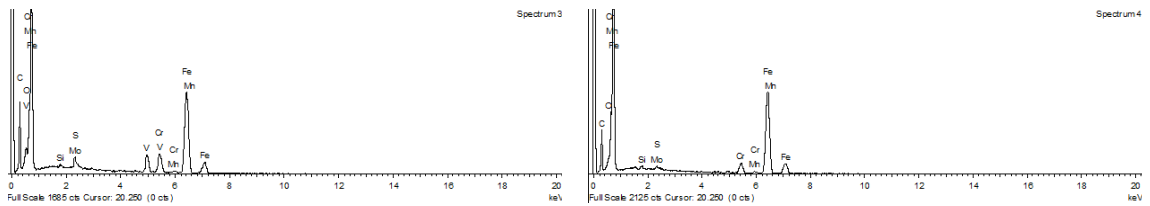
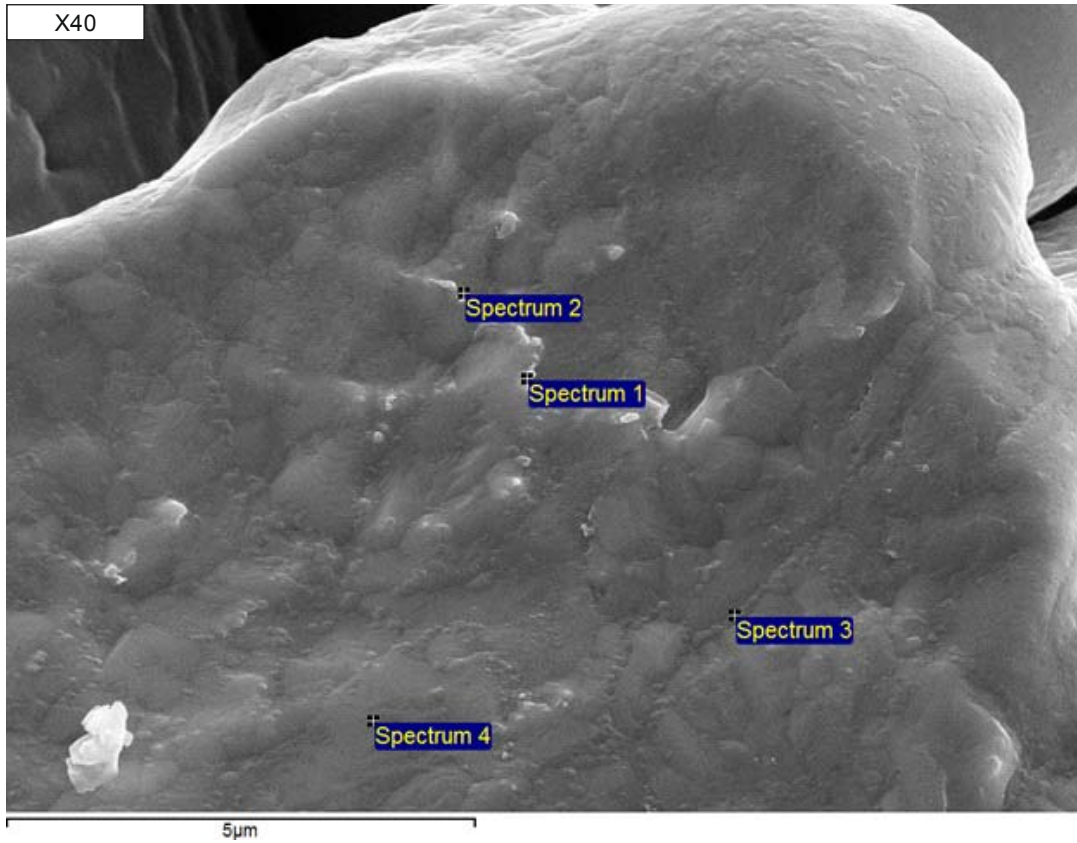
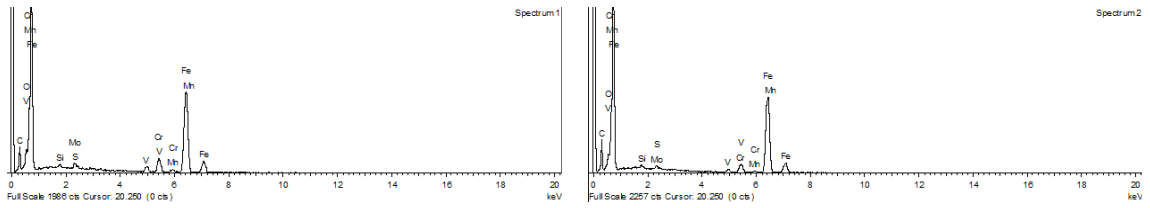


Figure 35: SEM image of the powder surface after heat treatment at 800 °C in vacuum



Calculated composition without carbon							
Spectrum	Cr	Mo	V	Mn	Si	Al	Fe
1 [at.-%]	4.54	0.52	0.86	0.20	0.37	38.96	54.55
2	5.45	1.02	0.84	0.60	0.58	0.08	91.42
3	5.63	0.83	0.46	0.12	0.62	0.04	92.30

Figure 36: EDX analysis of particulates on the powder surface after heat treatment at 800 °C in vacuum; spectra 1 and 2 analyze particulates and spectrum 3 matrix



Calculated composition without carbon						
Spectrum	Cr	Mo	V	Mn	Si	Fe
1 [at.-%]	7.02	1.37	2.95	0.78	1.03	86.85
2	5.10	1.21	1.38	0.70	1.08	90.53
3	8.82	2.68	8.88	0.00	0.54	79.18
4	6.24	0.84	0.68	0.26	0.87	91.10

Figure 37: EDX analysis of particulates on the powder surface after heat treatment at 800 °C in vacuum; spectra 1 and 2 analyze bright particulates, spectrum 3 dark particulates and spectrum 4 matrix

After annealing at 900 °C the powder particle surface is quite clean and evaporation lines can be seen clearly. Dark particulates can be found on the surface, which mainly appear in the interdendritic areas (see figure 38). They are rich in vanadium as can be seen in figure 39.

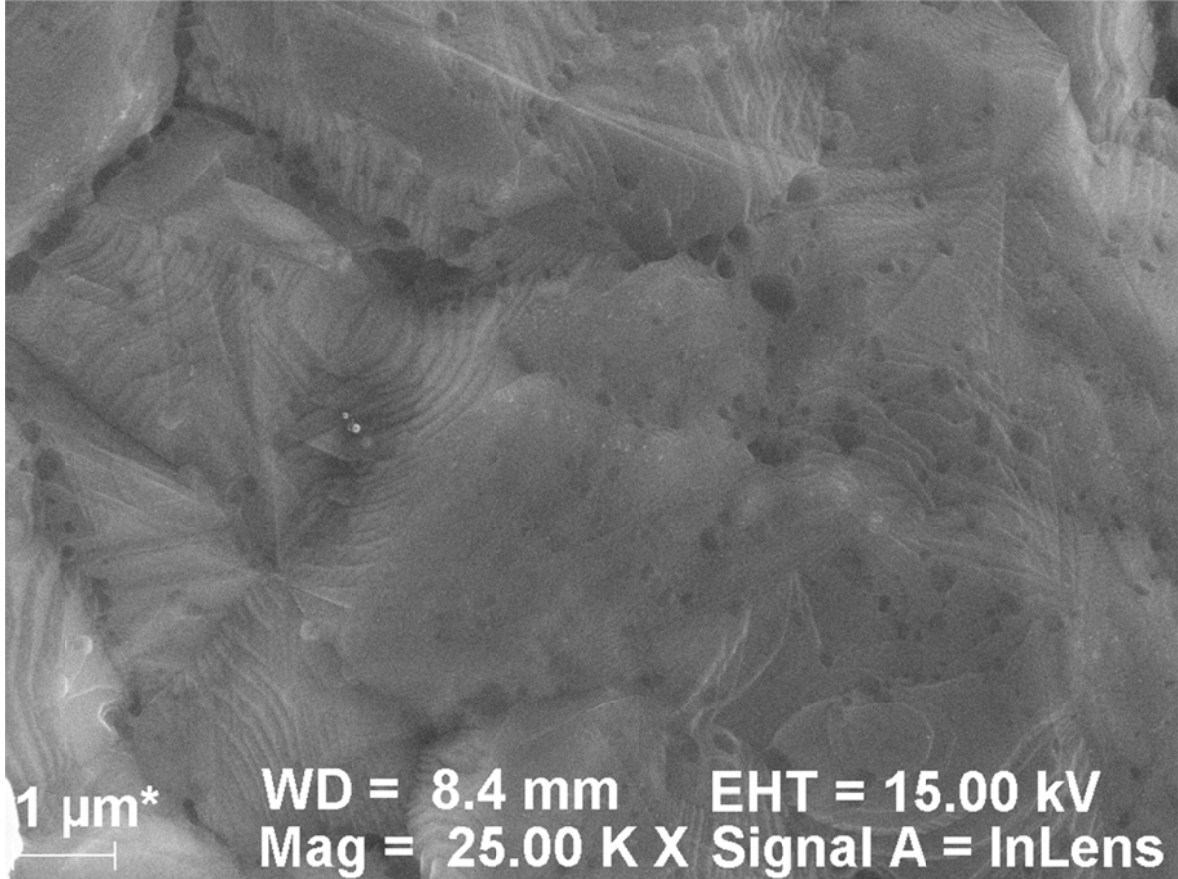
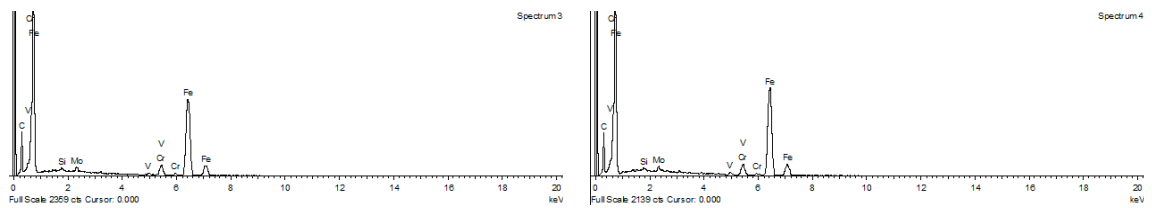
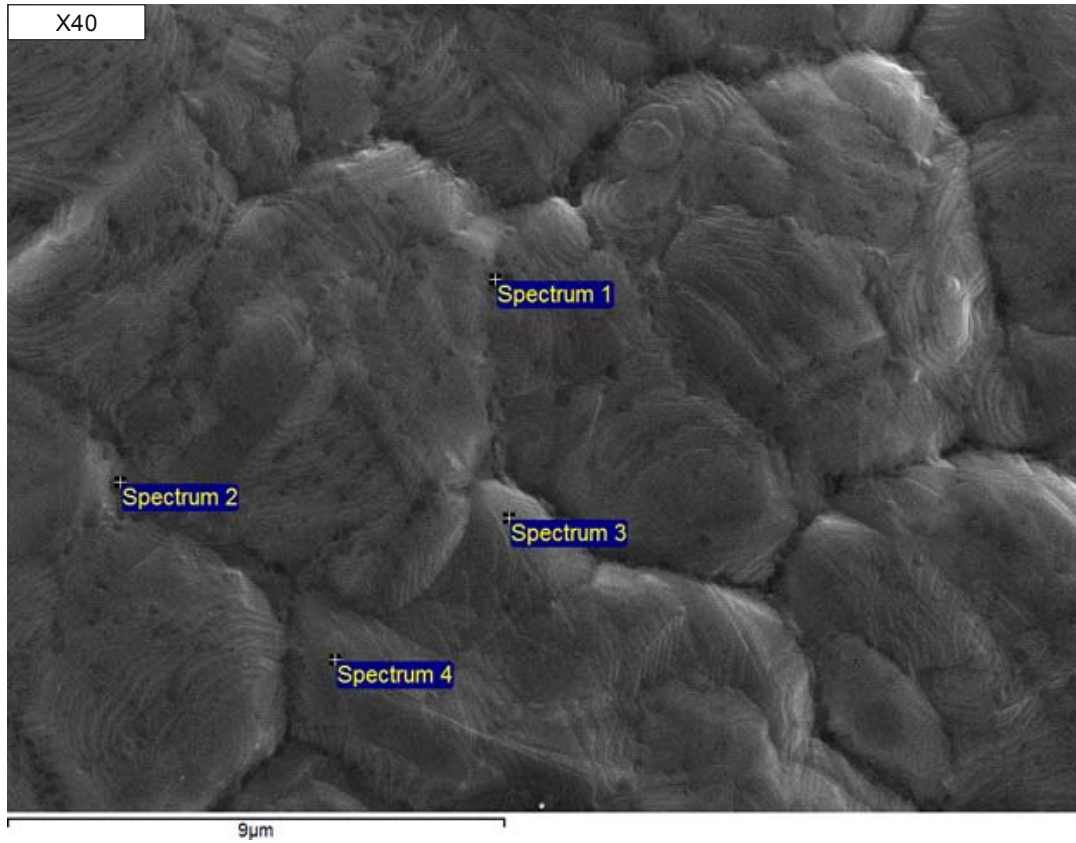
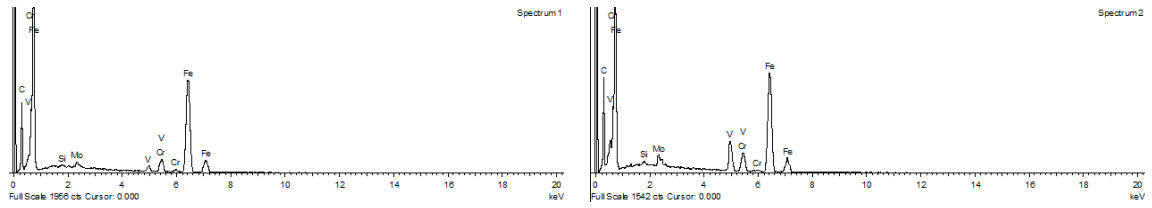


Figure 38: SEM image with an overview of the X40 powder surface after heat treatment at 900 °C in vacuum



Calculated composition without carbon						
Spectrum	Cr	Mo	V	Mn	Si	Fe
1 [at.-%]	6.55	1.07	2.57	0.00	0.47	89.34
2	7.02	2.56	12.89	0.00	0.57	76.97
3	5.93	1.35	0.73	0.00	1.02	90.97
4	6.15	1.31	1.06	0.00	0.59	90.90

Figure 39: EDX analysis of particulates on the powder surface after heat treatment at 900 °C in vacuum; spectra 1 and 2 analyze dark particulates and spectra 3 and 4 the matrix

A lot of aluminum-rich particulates, probably nitrides or oxides, can be found on the powder particle surface after annealing at 1000 °C as can be seen in figure 40. Besides that, still the vanadium rich dark spots can be detected.

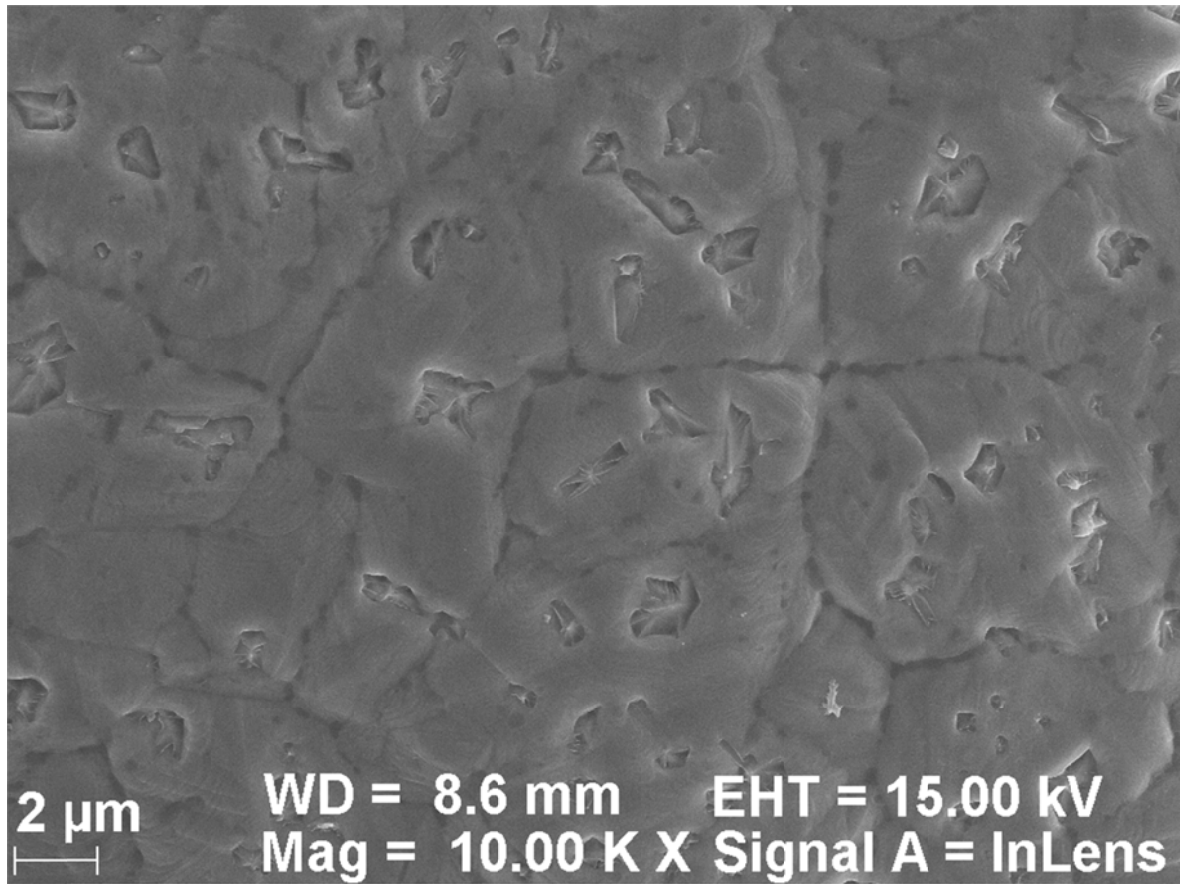
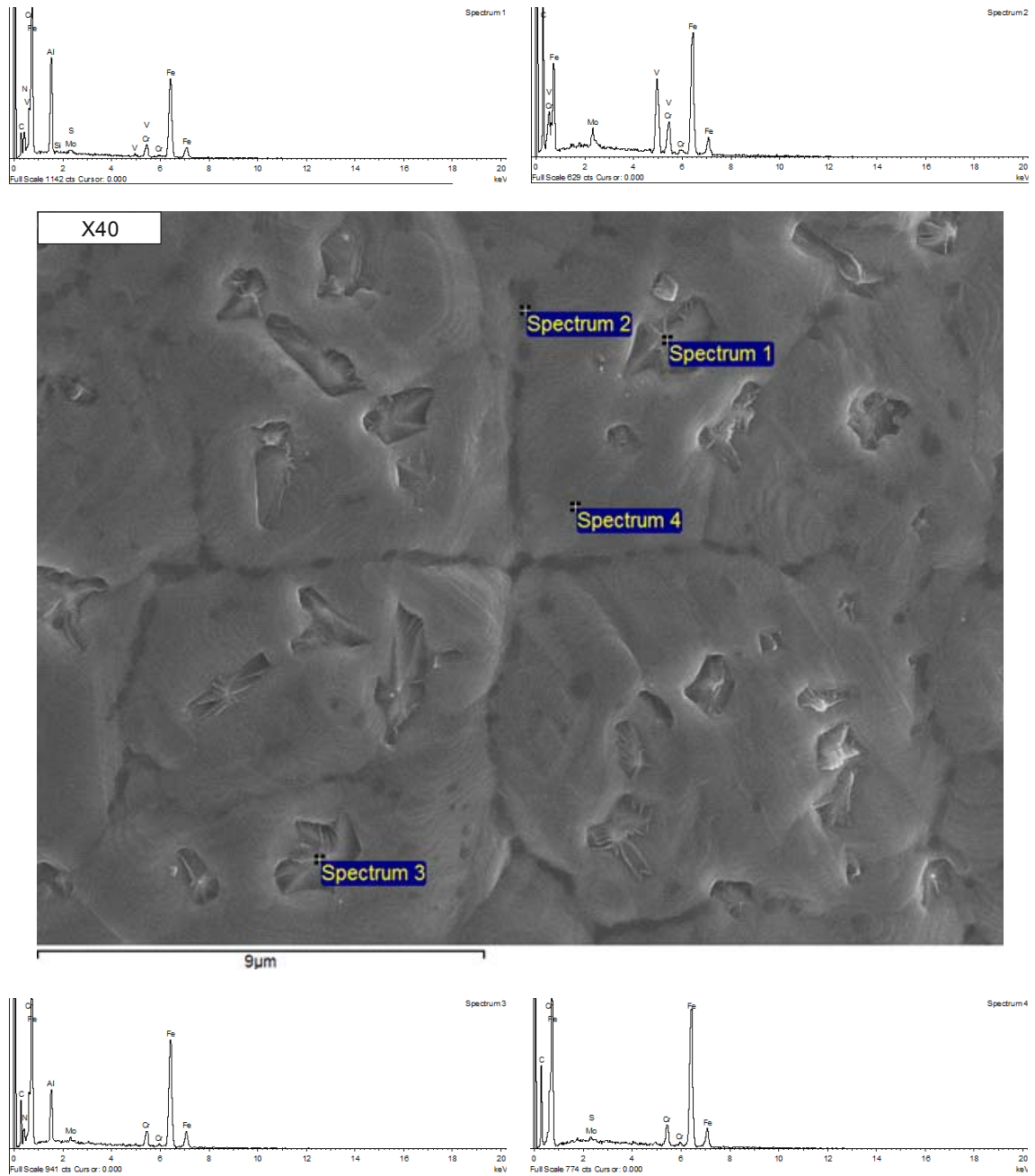


Figure 40: SEM image with an overview of the X40 powder surface after heat treatment at 1000 °C in vacuum



Calculated composition without carbon						
Spectrum	Cr	Mo	V	Al	Si	Fe
1 [at.-%]	5.20	0.64	0.84	27.17	0.64	65.52
2	7.46	2.30	20.89	0.32	0.43	68.61
3	6.28	0.97	0.51	13.94	0.15	78.15
4	7.11	0.71	0.74	0.24	0.58	90.62

Figure 41: EDX analysis of particulates on the powder surface after heat treatment at 1000 °C in vacuum. Spectra 1 and 3 analyze Al-rich particulates, spectrum 2 V-rich dark particulates and spectrum 4 the matrix

3.2.2 X-ray Photoelectron Spectroscopy

Survey scans

Figure 42 gives an overview of survey scans of the powder surface in the as-received state as well as after heat treatment at different temperatures in vacuum. Due to the influence of a contamination layer, the survey scans after 1 nm of etching are shown.

The survey scans were used to identify the elements present on the powder surface. Iron is one of the main elements in the most surveys scans. Also an intensive signal of oxygen can be found, but it decreases strongly for annealing temperatures above 700 °C. Besides that, distinctive signals of chromium, vanadium, molybdenum and sulfur were detected. Manganese is mainly visible at heat treatment temperatures up to 800 °C. Also traces of silicon and nitrogen can be found. Aluminum is only detectable after annealing at 900 and 1000 °C in the oxidic state.

At 397 eV the N 1s and Mo 3p peaks are overlapping. Since the molybdenum peaks are located at 394.0 eV (3p_{3/2}) and 411.6 eV (3p_{1/2}) respectively [40], the peak around 397 eV could be identified as the nitrogen N 1s peak.

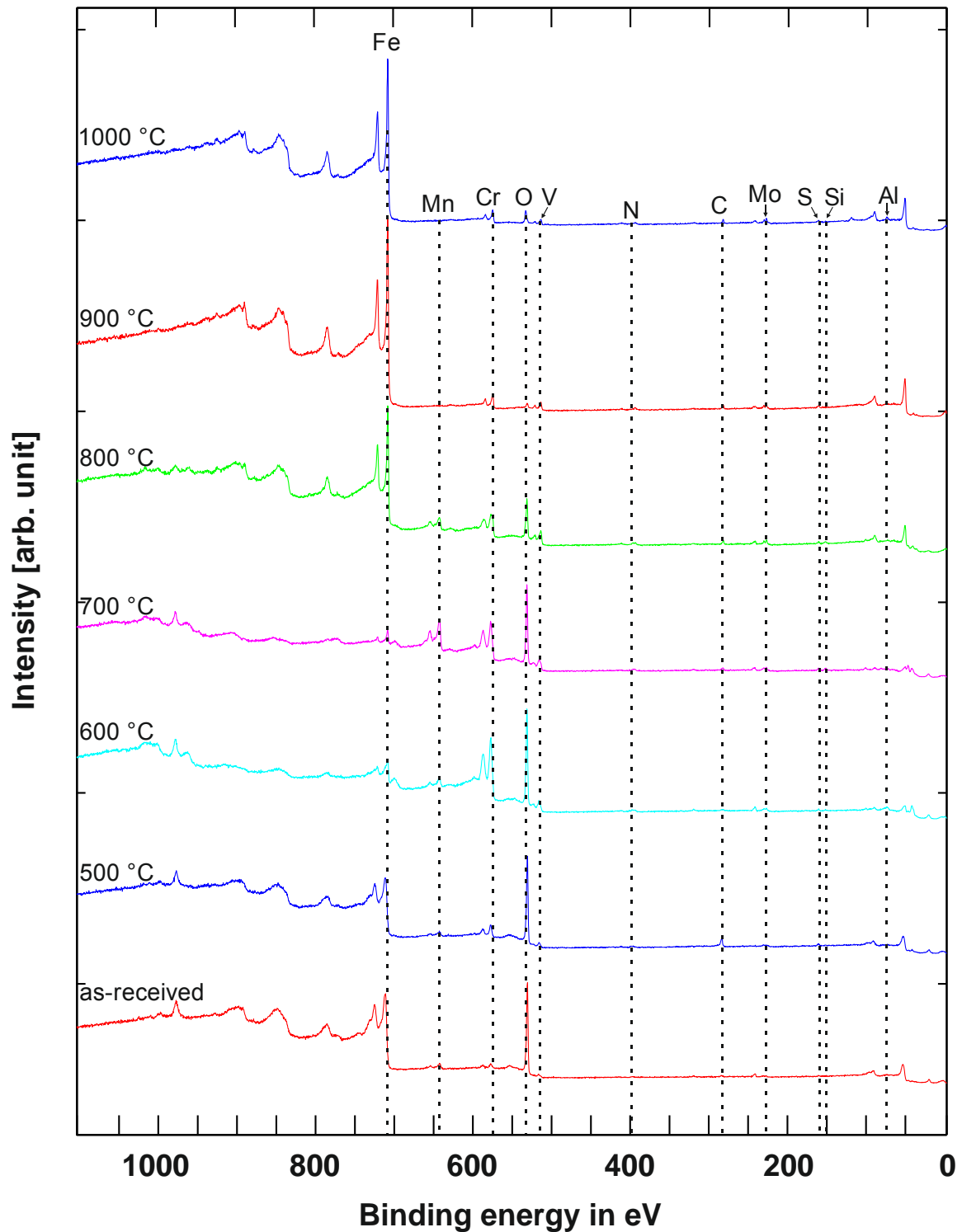


Figure 42: Survey scans of the powder surface at 1 nm etch depth after heat treatment at different temperatures in vacuum compared to the as-received state

High resolution narrow scans

High resolution narrow scans were performed for the elements Fe, Cr, Mo, V, Mn, Si, O, C, S and N to analyze chemical shifts and identify compounds formed on the powder surface. The scans were also performed for Al after annealing at 900 and 1000 °C. The peak appearance and position gives clue about the chemical state of an element.

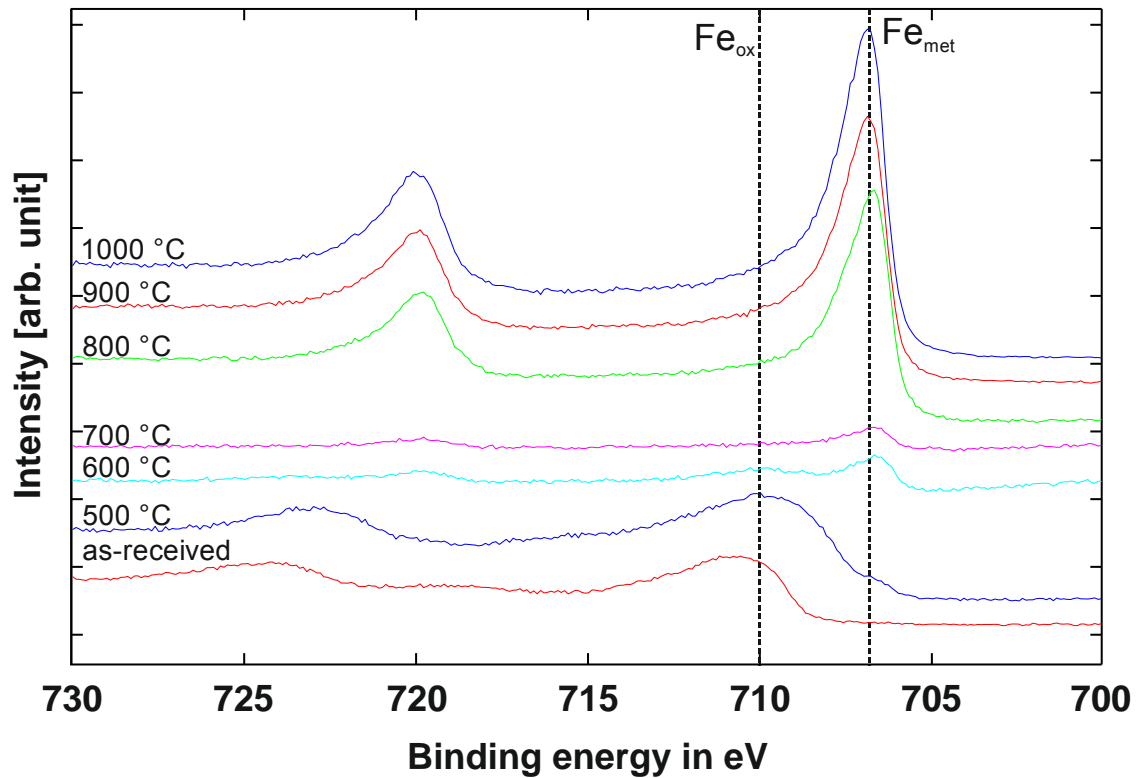


Figure 43: High resolution narrow scan of the iron Fe 2p peak at in the as-annealed state at different heat treatment temperatures in vacuum

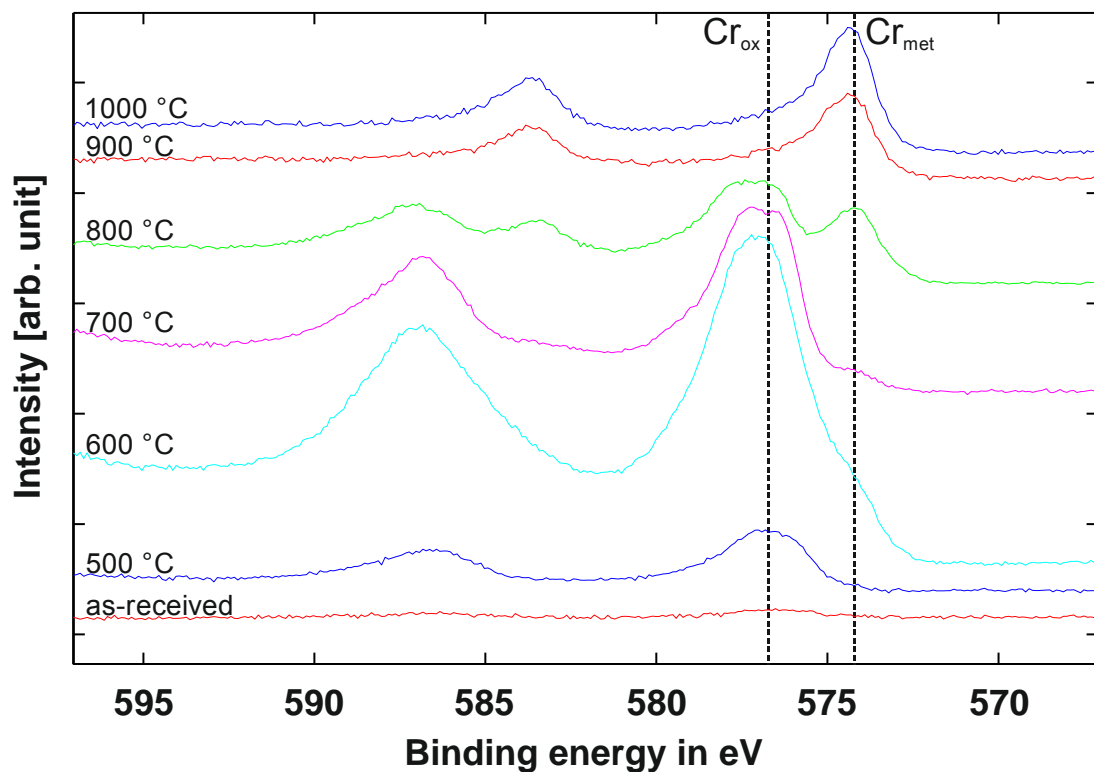


Figure 44: High resolution narrow scan of the chromium Cr 2p peak in the as-annealed state at different heat treatment temperatures in vacuum

Figure 43 shows a high resolution narrow scan for the Fe 2p peak after different heat treatment temperatures in the as-annealed state. It can be seen that in the as-received state

iron is only present in the oxidic state. A heat treatment at 500 °C leads to the appearance of a very weak metallic signal. Annealing at 600 °C and 700 °C changes the peak appearance completely as it shifts to the lower binding energies and the signal becomes rather weak. The shift of the peak means that iron is mainly metallic now. With even higher annealing temperatures the signal intensity increases again.

The development of the chromium Cr 2p peak is shown in figure 44. The chromium signal in the as-received state is rather weak and indicates its presence in a fully oxidic state on the surface. With annealing at 500 °C the intensity increases a little bit, but it increases very strongly after annealing at 600 °C. Also the appearance of a shoulder on the main peak indicates appearance of Cr in metallic state. With higher annealing temperatures the signal gets weaker and the peak shifts to lower binding energies. After annealing at 900 and 1000 °C peak positions indicate fully metallic state.

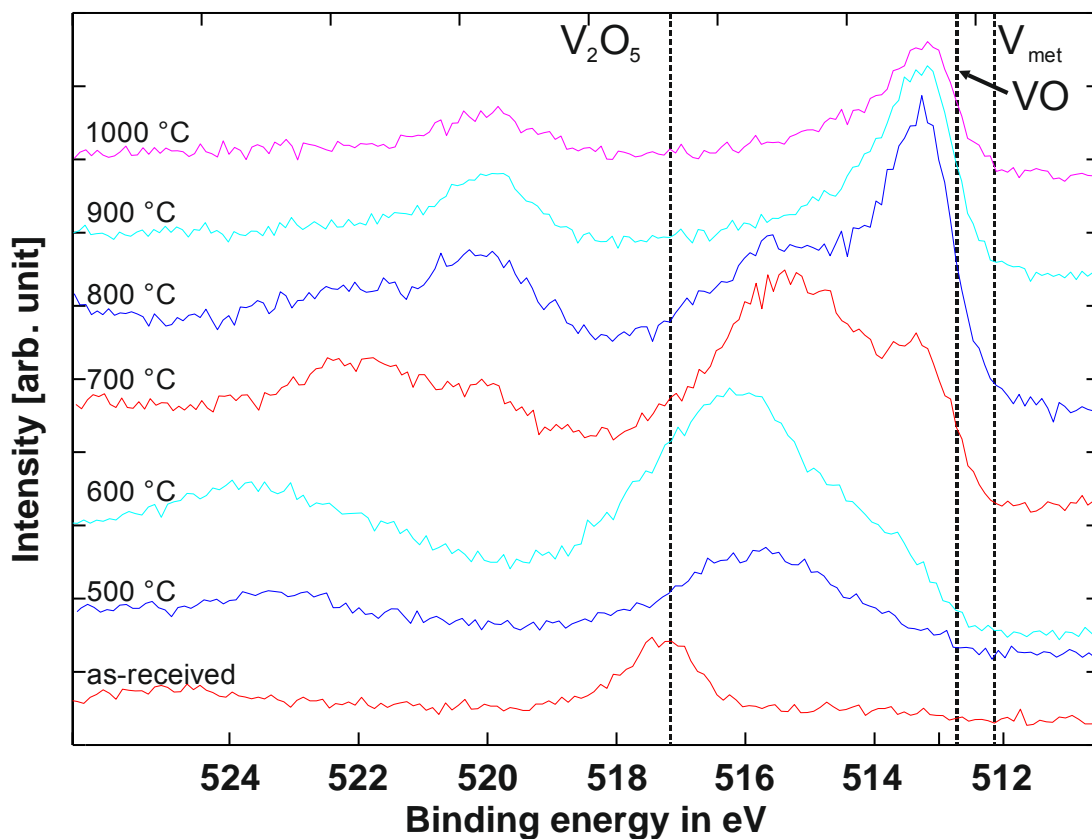


Figure 45: High resolution narrow scan of the vanadium V 2p peak in the as-annealed state at different heat treatment temperatures in vacuum

The changes of the appearance of the vanadium V 2p peak are shown in figure 45. In the as-received state the peak is located at 517.1 eV and has a rather low intensity. The peak position corresponds to the vanadium pentoxide oxide V_2O_5 . With increasing annealing temperatures the peak shifts constantly to lower binding energies. In the temperature range from 600 to 800 °C a double peak is visible and considerably more intense than in the as-received state. After annealing at 900 and 1000 °C the peak is located at 512.7 eV which

corresponds most probably to VO oxide [38] or VC carbide [41]. Also the peak intensity decreases.

Manganese can only be found in the oxidic state on the surface (see figure 46). The intensity increases with increasing temperature to 700 °C. After annealing at 800 °C the signal becomes weaker and disappears completely after annealing at 900 and 1000 °C.

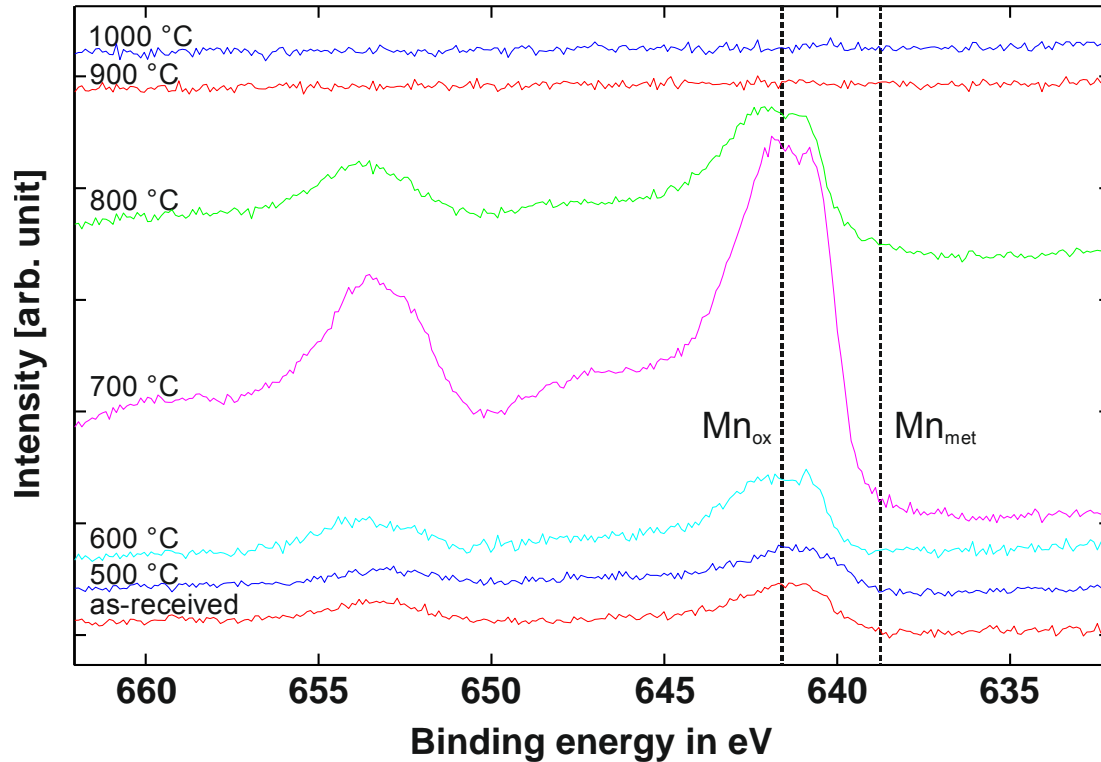


Figure 46: High resolution narrow scan of the manganese Mn 2p peak in the as-annealed state at different heat treatment temperatures in vacuum

The high resolution narrow scans of molybdenum and silicon are shown in the appendix in figure 63 and figure 64. They do not show any peak shift and hence no transformation of the chemicals state. But variations of the intensity can be seen. In contrast, carbon C 1s shows a shift from 285.1 eV to 283.1 eV with increasing annealing temperature (see figure 47). In the as-received state the S 2p peak is located at about 169 eV as can be seen in figure 48. This binding energy is related to the SO_4^{2-} group. After heat treatment the peak shifts to about 162 eV and increases steadily with increasing annealing temperature. Apparently the peak is composed of two peaks with a minor peak at slightly higher energies.

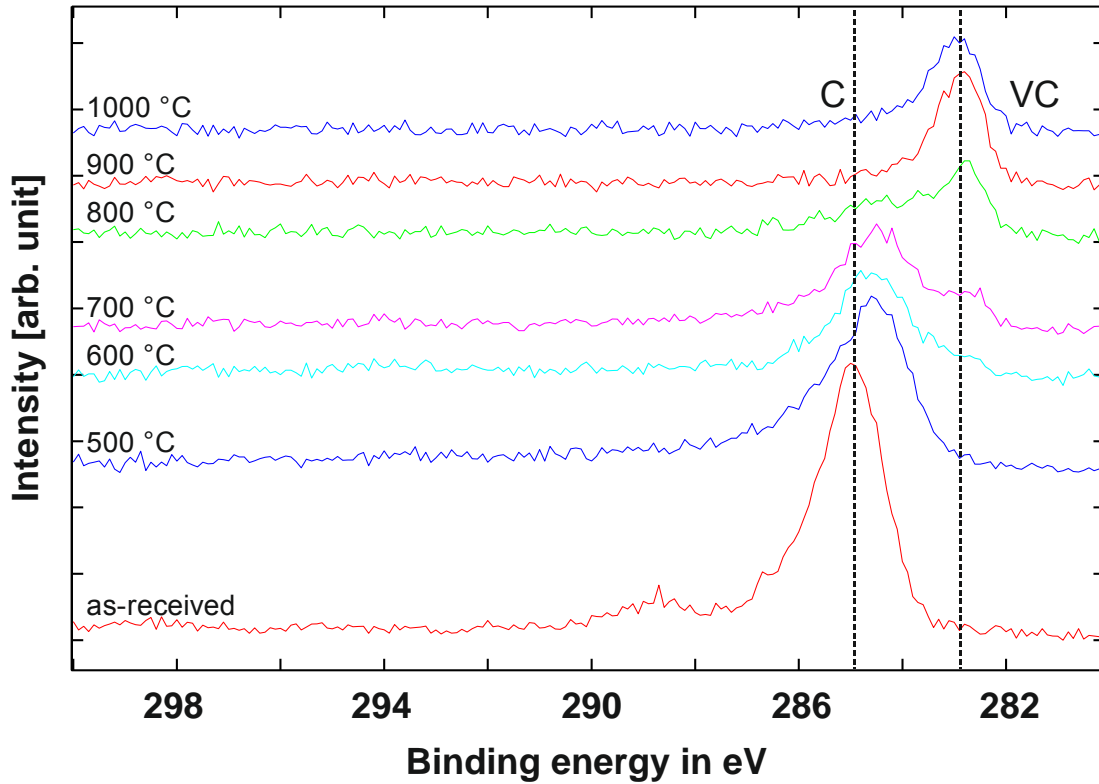


Figure 47: High resolution narrow scan of the carbon C 1s peak in the as-annealed state after different heat treatment temperatures in vacuum

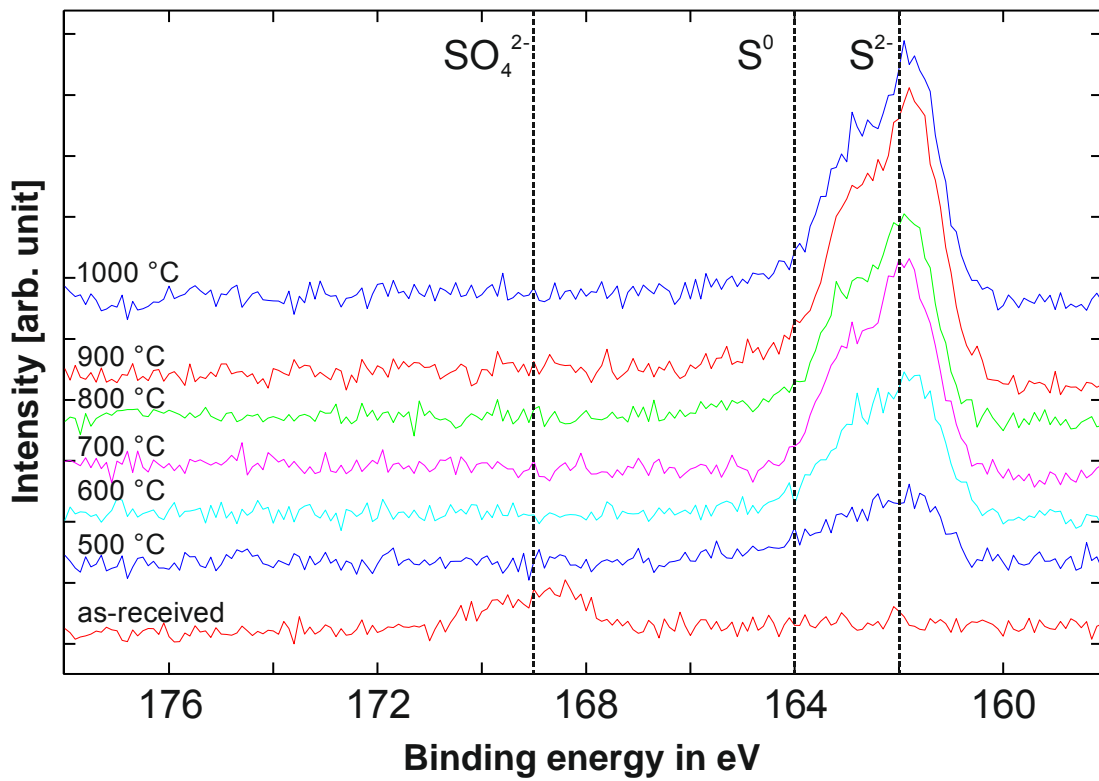


Figure 48: High resolution narrow scan of the sulfur S 2p peak in the as-annealed state after different heat treatment temperatures in vacuum

Chemical composition of the powder surface after heat treatment

The high resolution narrow scans were used to determine the chemical surface composition quantitatively. Figure 49 shows the results over the etch depth for different annealing temperatures in vacuum. This diagram will be used to describe the development of the non-metallic elements. The development of the metallic elements will be described in the next subchapter “Metal composition of the powder surface after heat treatment”. This has the advantage that the trends for the metallic elements can be seen more clearly, as changes in the fraction of non-metallic elements can be quite steep and this strongly affects the fraction of the metallic elements. The exact values for the chemical composition after heat treatment can be found in the appendix in table 7 to 12.

After annealing at 500 °C the chemical compositions of the powder surface changes only very slightly compared to the as-received state. Remarkable is that the trace elements like nitrogen and sulfur appear stronger on the outermost surface. The content of sulfur increases to almost 3 at.-%. The oxygen content decreases slightly after annealing at 700 °C. The content of sulfur, nitrogen and silicon increases further. After heat treatment at 800 °C the oxygen content decreases considerably to 30 at.% and to 6 at.-% after annealing at 900 °C. Hence, after annealing at 900 °C the oxygen content on the outermost layer is lower than in the inner layers due to segregation of other non-metallic elements, especially sulfur with over 8 at.-%. After annealing at 1000°C the oxygen content on the outermost layer decreases even more to 2 at.-%. The sulfur content is still high with 8 at.-%. Furthermore, nitrogen is enriched with almost 4 at.-%.

Metal composition of the powder surface after heat treatment

To evaluate the development of the metallic elements, the non-metallic elements have been excluded and the data normalized to 100 %. The corresponding diagram can be seen in figure 50.

After annealing at 500 °C the amounts of Cr, V and Mn increased on the outermost surface compared to the as-received state. The fraction of molybdenum is below 1 % on the outermost surface and increases with etch depth. The trend of enrichment of the alloying elements increases further with annealing at 600 °C. Chromium is the major metallic element with 66 at.-%. Also vanadium increased strongly to almost 11 at.-% and manganese to 7 at.-%. In general, the enrichment can mainly be seen in the top 10 nm. On the other hand, the amount of silicon decreased a little bit and the fraction of iron is very low with 14 at.-%. Manganese is the major element on the surface after annealing at 700 °C with 40 at.-%. Furthermore, increased silicon content can be found with a maximum of 9 at.-% after 3 nm of etching. The fraction of chromium decreases to 33 at.-%.

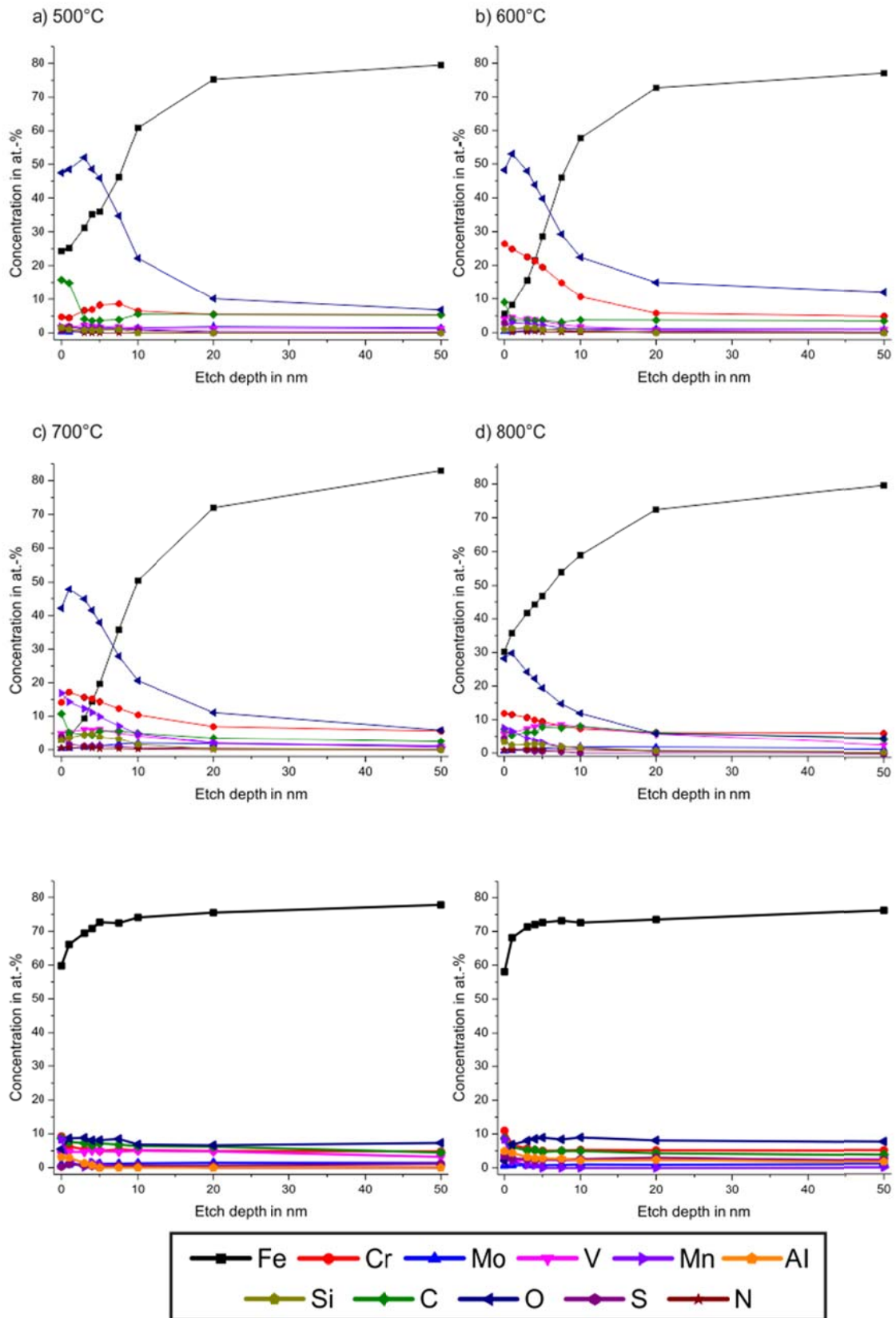


Figure 49: Surface composition over the etch depth for annealing temperatures between 500 and 1000 °C

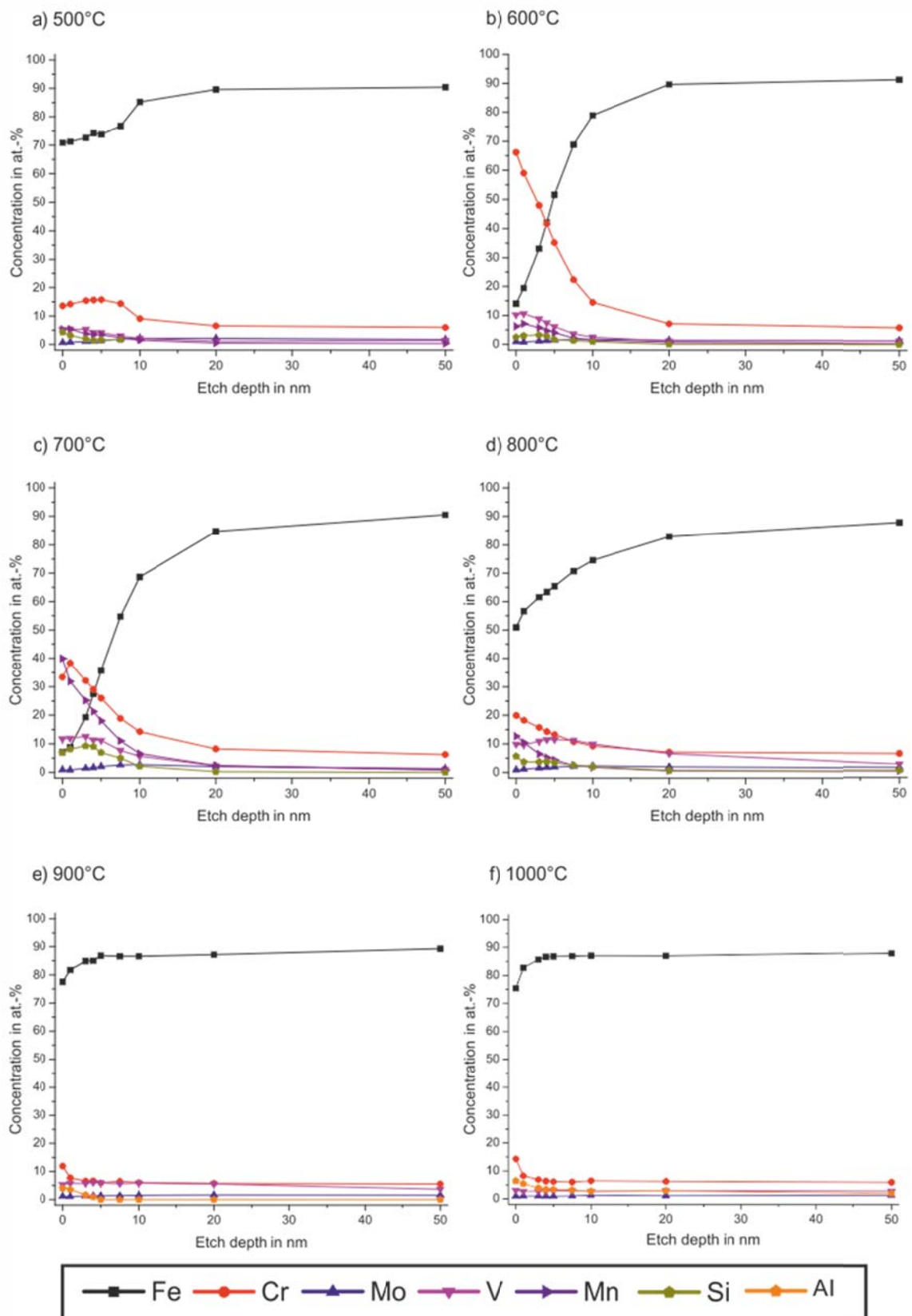


Figure 50: Composition of metallic elements on the powder surface over the etch depth for annealing temperatures between 500 and 1000 °C

After annealing at 800 °C the amount of alloying elements on the powder surface decreases compared to 700 °C. Therefore, iron is the major element again, followed by chromium with ~20 at.-% and manganese (13 at.-%). The amount of vanadium and silicon remains almost the same.

Annealing at 900 °C decreases the amount of alloying elements on the surface even more. Chromium is still enriched in the surface with 12 at.-%, but its content decreases strongly after etching. Molybdenum stays on a quite constant level just above 1 at.-% for all etch depth. Vanadium is very slightly enriched on the surface with 5 at.-% on the outermost layer and decreases constantly to about 4 at.-% after 50 nm of etching. Manganese and silicon cannot be found anymore. But instead, aluminum can be detected with 4 at.-% on the outermost layer. After 5 nm of etching it cannot be detected at all.

Annealing at 1000 °C leads to an increase of the aluminum content to 5 at.-% on the outermost layer and after 50 nm of etching still almost 2 at.-% can be found. The vanadium content decreases to 2 at.-%. Chromium is still strongly enriched in the surface with 14 at.-%, but it decreases to 8 at.-% after 1 nm of etching.

Chemical state of the metallic elements and composition of cations on the powder surface after heat treatment

In figure 51 the fraction of the metallic state is plotted over the etch depth for different heat treatment temperatures for iron, chromium and manganese. Vanadium and molybdenum are not shown, because vanadium was only found in the oxidic state and molybdenum only in the metallic state. Aluminum found after annealing at 900 and 1000 °C was also only detected in the oxidic state. The fraction of the metallic state of manganese was not evaluated for all etch depth as it was not always possible to perform curve fitting due to its low content.

The differences in the chemical state after 500 °C of annealing compared to the as-received state are quite small. However, after annealing at 600 °C iron is mainly reduced. The amount of metallic chromium and manganese decreased for the etch depth of 20 nm and 50 nm. The amount of metallic chromium increased again after annealing at 700 °C. But still some oxidic chromium can be found even after 50 nm of etching. Annealing at 800 °C leads to full reduction of iron and higher amount of reduced chromium on the outermost surface. But after annealing at 900 °C chromium is also fully reduced for all etch depth. After annealing at 900 °C and 1000°C no manganese was found at all.

Figure 52 shows the relative cation concentration over the etch depth on the powder particle surface for different heat treatment temperatures in vacuum. After annealing at 500 °C iron is the main cation on the powder surface with 71 %. After 5 nm of etching its fraction decreases constantly to 0 % after 20 nm of etching. When the fraction of iron cation decreases the fraction of chromium cation increases. On the outermost surface 14 %

of all cations are chromium. The fraction increases to about 32 % from 7.5 nm to 20 nm of etching and decreases again to 0 % after 50 nm. The fraction of vanadium is about 5 % on the outermost surface, but it increases constantly after 7.5 nm of etching and reaches 89 % after 50 nm of etching. The manganese fraction is about 5 % in the outer layers with a maximum of 16 % after 20 nm of etching. The fraction of silicon cations is rather low with a maximum of 5 % after 7.5 nm of etching.

Chromium becomes the main cation after heat treatment at 600 °C. On the outermost surface its fraction is 73 % and it decreases constantly to 40 % after 50 nm of etching. At the same time the fraction of iron decreases strongly with a maximum of 7 % after 1 nm of etching. The second largest fraction is observed for vanadium cations. Their amount increases constantly from 12 % in the unetched state to 49 % after 50 nm of etching. The fraction of manganese and silicon also increases slightly compared to 500 °C with a maximum of 13 % after 20 nm of etching for manganese and 8 % after 10 nm of etching for silicon.

Besides chromium the surface is mainly enriched in manganese after annealing at 700 °C. Both elements have a cation fraction of about 42 %. With increasing etch depth the amount decreases to 25 % after 20 nm of etching for chromium and 22 % after 50 nm for manganese. Vanadium becomes the main cation after 10 nm of etching. It increases constantly with increasing etch depth from 13 % to 44 %. The fraction of silicon increases from 7 % at the outermost surface to 17 % after 7.5 nm of etching and decreases again to 0 % after 50 nm of etching. The iron cation fraction is below 1 %.

After annealing at 800 °C the outermost surface is still enriched in chromium (32 %) and manganese (29 %). But also high fraction of vanadium can be found of around 24 %. With increasing etch depth the fraction of chromium and manganese decreases and the fraction of vanadium increases. After 3 nm of etching vanadium is already the main cation and it has a maximum of 82 % after 50 nm of etching. The fraction of silicon is rather constant over all etch depth and varies between 9 and 16 %.

Vanadium is the main cation after heat treatment at 900 °C. Besides vanadium also aluminum cations can be found on the top surface with 43 %. After 5 nm of etching only vanadium cations are found.

The amount of aluminum cations increases after annealing at 1000 °C and is the main fraction for the top 10 nm. At higher etch depths the amount of vanadium cations is slightly increases.

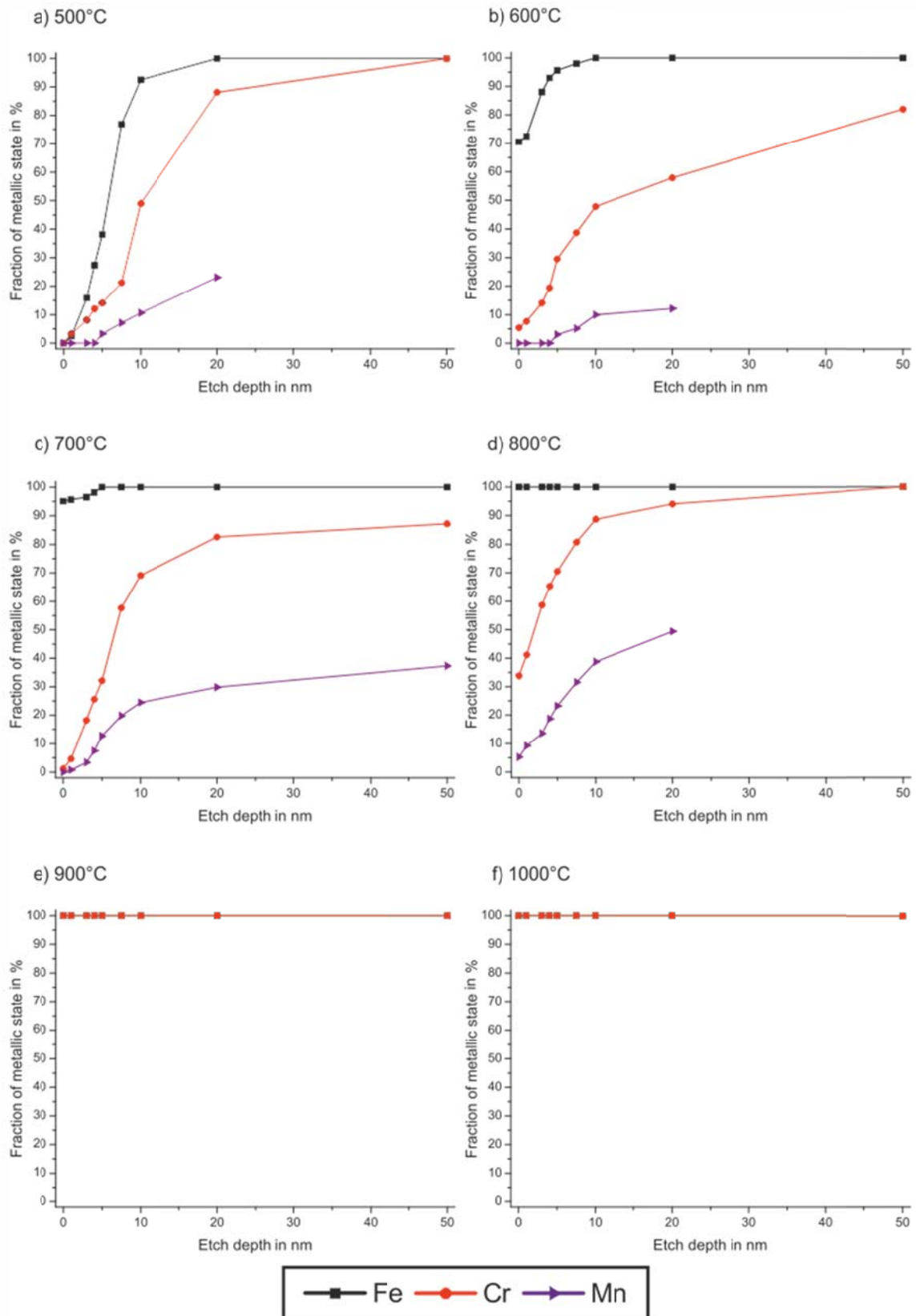


Figure 51: Fraction of the metallic state over the etch depth for Fe, Cr and Mn after heat treatment at different temperatures in vacuum; no Mn was found after annealing at 900 and 1000 °C

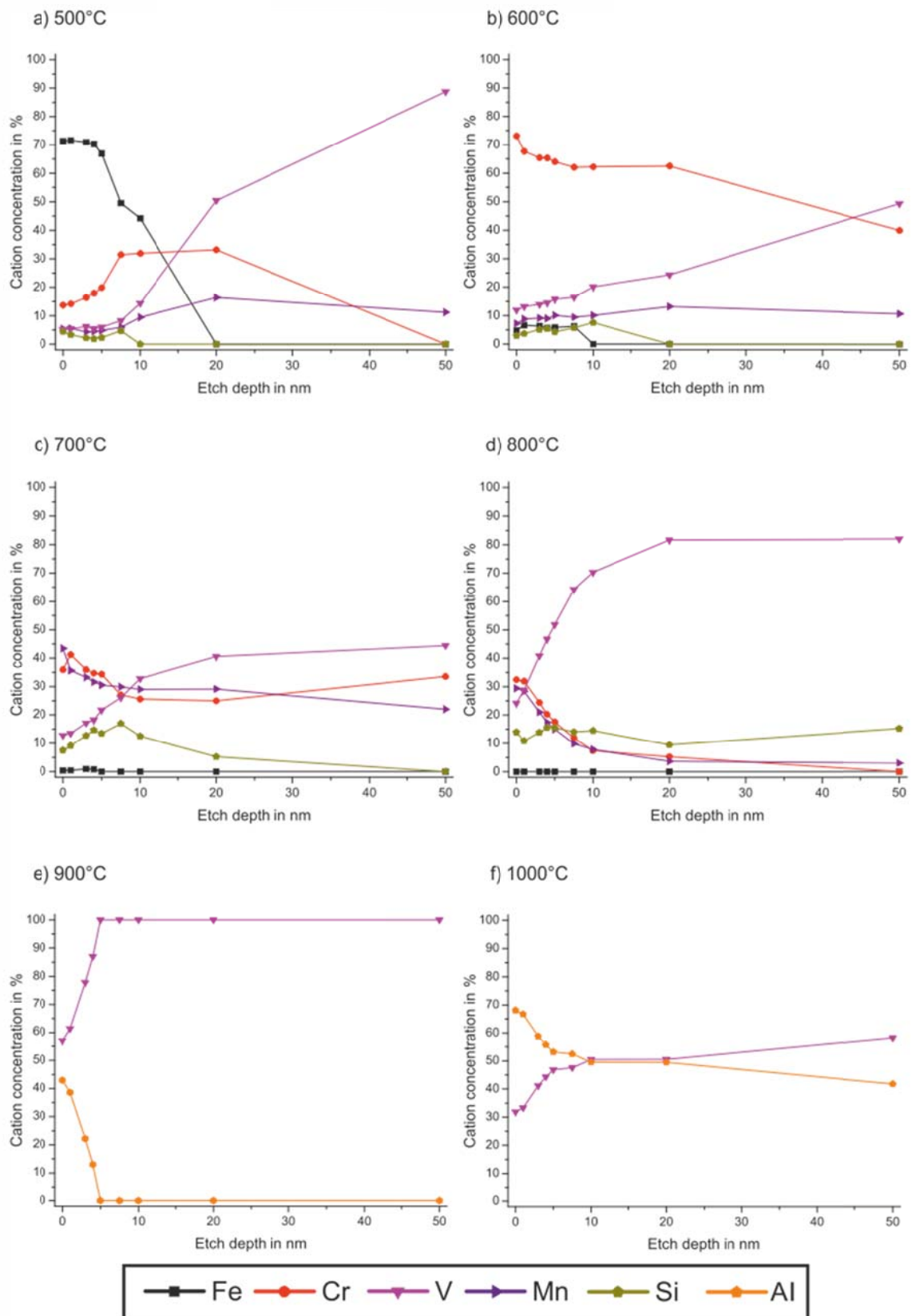


Figure 52: Relative cation concentration over the etch depth after heat treatment at different temperatures in vacuum

3.3 Thermoanalytical investigations

3.3.1 Thermogravimetry Analysis

In figure 53 the TGA measurements of the unsieved X40 powder, a fine size fraction (36 - 63 μm) and a coarse size fraction (100 - 150 μm) are shown. The evaluation of the measurements can be found in the appendix in figure 60, figure 61 and figure 62.

Two main steps of weight loss are clearly visible in the plots. The onset of the unsieved powder appears at 1016 $^{\circ}\text{C}$. For coarse powder it appears at lower temperatures ($T_{\text{Onset}} = 983$ $^{\circ}\text{C}$) and at higher temperatures for fine powder ($T_{\text{Onset}} = 1023$ $^{\circ}\text{C}$). In return, the weight loss in the first step is more pronounced for fine powder (-0.04 %) and unsieved powder (-0.04) compared to coarse powder (-0.02 %). However, the second step of weight loss happens at lower temperature for fine powder ($T_{\text{Onset}} = 1156$ $^{\circ}\text{C}$) compared to unsieved powder ($T_{\text{Onset}} = 1161$ $^{\circ}\text{C}$) and coarse powder ($T_{\text{Onset}} = 1063$ $^{\circ}\text{C}$). The weight loss is also in the second step more pronounced for the fine powder (-0.03 %) and unsieved powder (-0.03 %) compared to coarse powder (-0.02 %).

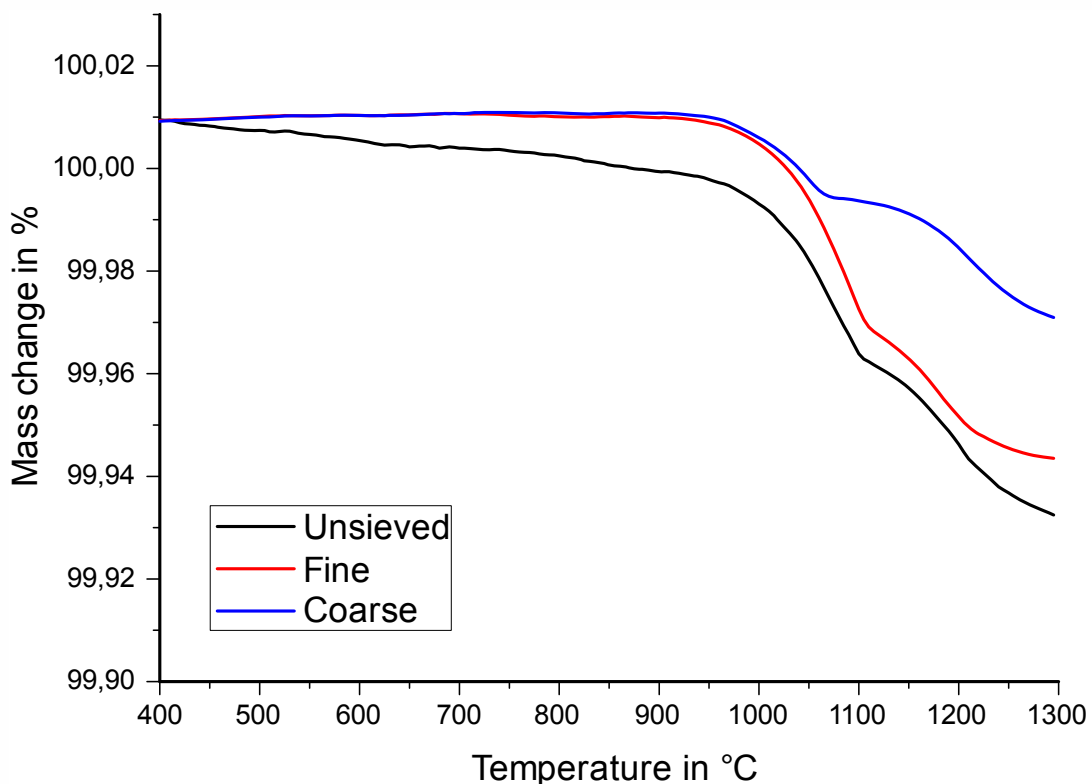


Figure 53: TGA measurements of the X40 unsieved, fine (36 - 63 μm) and coarse (100 - 150 μm) in flowing argon with a heating rate of 10 K/min

3.3.2 Residual Gas Analysis

In figure 54 the ion concentration is plotted as partial pressure against the temperature. The mass numbers 12, 14, 28 and 44 have been chosen to be of interest for this work. Considering the whole diagram three main peaks are visible. The first one has its peak temperature (T_{Peak}) at 911 °C. It also has a slight shoulder around 868 °C. The second peak occurs at 1053 °C and the third one is not fully completed but its peak temperature seems to be at 1189 °C. The graphs of the mass numbers 12 (C) and 28 (CO_2) show qualitatively the same shape, except on the temperature range from about 1150 °C to 1200 °C. In this temperature range the mass number 14 (N) shows a significant peak. This indicates that the first two peaks are related to an increase of the CO-concentration, whereas the third peak can be related to an increase of the N_2 -concentration. The mass number 44 (CO_2) increases constantly for temperatures above 770 °C. The three peaks lead to very small peaks in this graph as well.

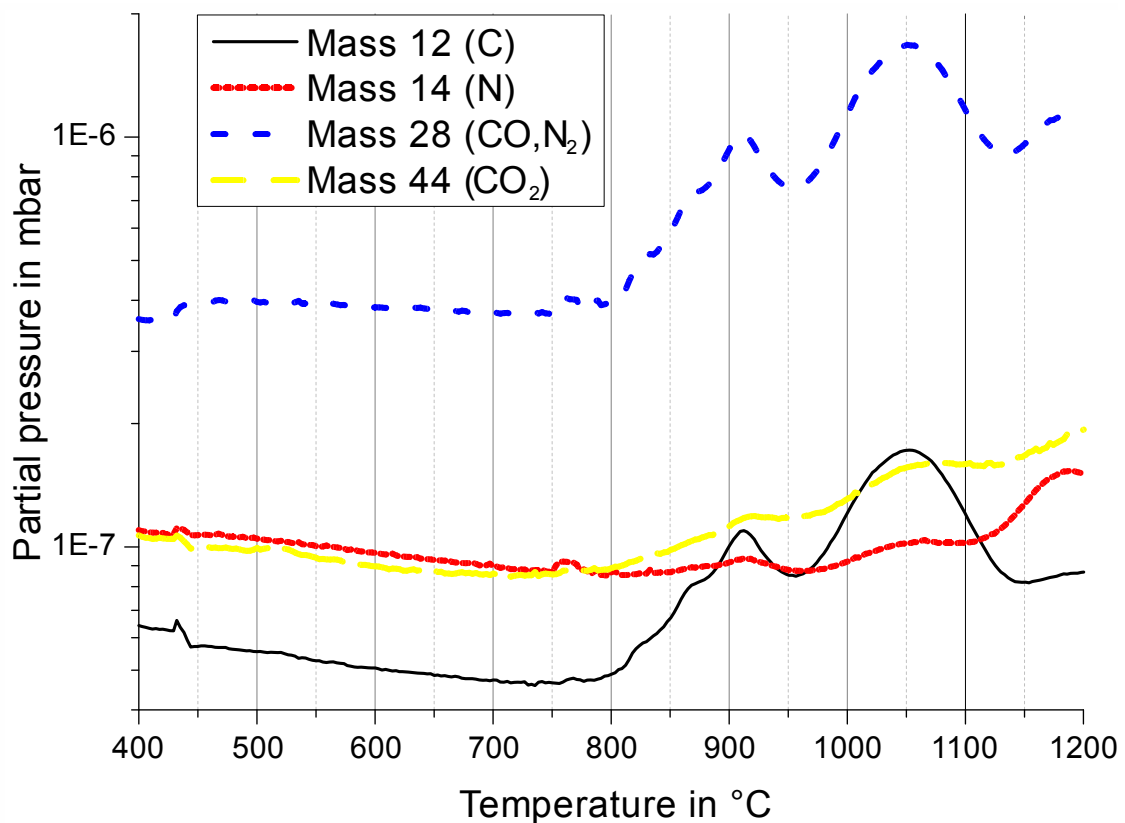


Figure 54: Residual gas analysis of the X40 powder in high-vacuum with a heating rate of 10 K/min

3.3.3 Differential Thermal Analysis

In figure 55 the DTA-measurement of the X40 in helium atmosphere is shown. Two exothermic peaks can be seen. The first one occurs between 740 °C and 780 °C with a peak temperature (T_{Peak}) of 765 °C. The second peak is more intensive and is located between 840 °C and 890 °C ($T_{\text{Peak}} = 859$ °C).

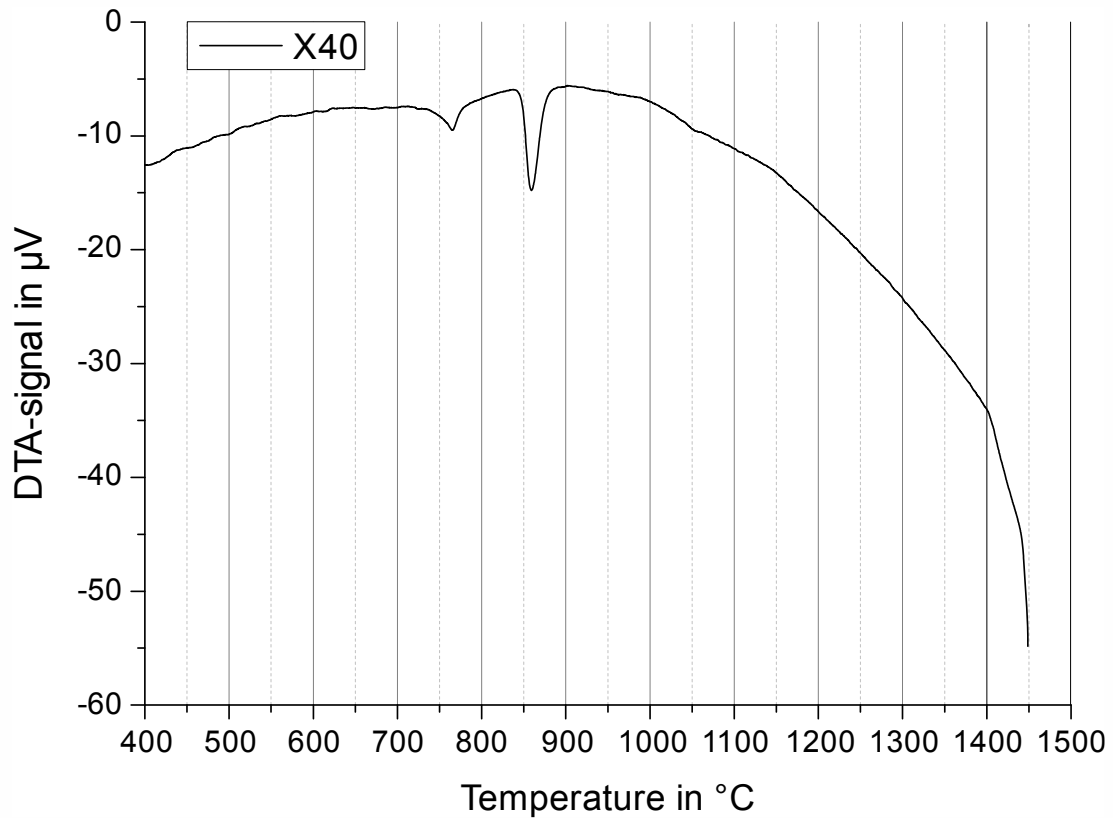


Figure 55: DTA-analysis of the phase transformations of the X40-powder in helium atmosphere with a heating rate of 10 K/min

3.3.4 Dilatometry

The dilatometric investigation of the X40 powder is shown in figure 56 for temperatures above 400 °C. From 400 °C to 733 °C the powder expands almost linearly to about 0.49 %. From there on until 843 °C the elongation remains constantly and then the powder contracts rapidly to 0.24 % until 883 °C. Then again, the powder elongation remains constant until about 962 °C. Above that temperature the powder starts to densify, first slowly then rapidly with a very strong densification rate above 1404 °C.

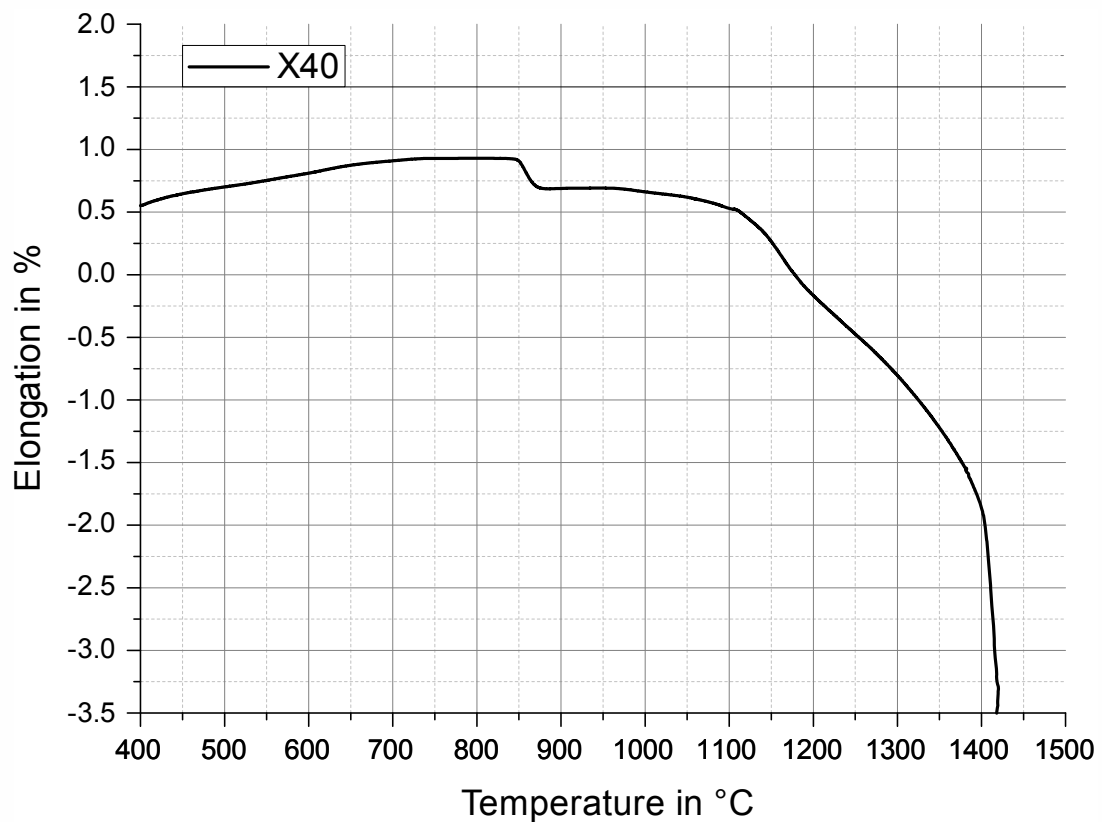


Figure 56: Dilatometric measurement of the X40 powder in high-vacuum with a heating rate of 10 K/min

3.3.5 Calculation of phase transformations

The calculated volume fractions of the phases as a function of the temperature in vacuum for the steel X40 is shown in figure 57. At low temperatures until 830 °C the material is basically ferritic in the thermodynamic equilibrium state. Above that temperature the ferrite transforms into austenite. Besides that, some hard phases are stable. Until 777 °C these are about 6 vol.-% of chromium-rich $M_{23}C_6$ -carbides (M stands for metal). At higher temperatures they transform into M_7C_3 -carbides, which then dissolve at about 902 °C. Between 840 °C and 904 °C a very low amount of molybdenum and vanadium rich carbides of the stoichiometry M_2C is stable. Also ~1.5 vol.-% of vanadium-rich monocarbides (VC) are stable up to 1063 °C. Above 1063 °C none of the described hard phase is stable and the material is fully austenitic in the equilibrium state. At about 1409 °C the solidus line is located. Above that temperature, the material starts to melt with an appearance of delta-ferrite between 1432 °C and 1486 °C.

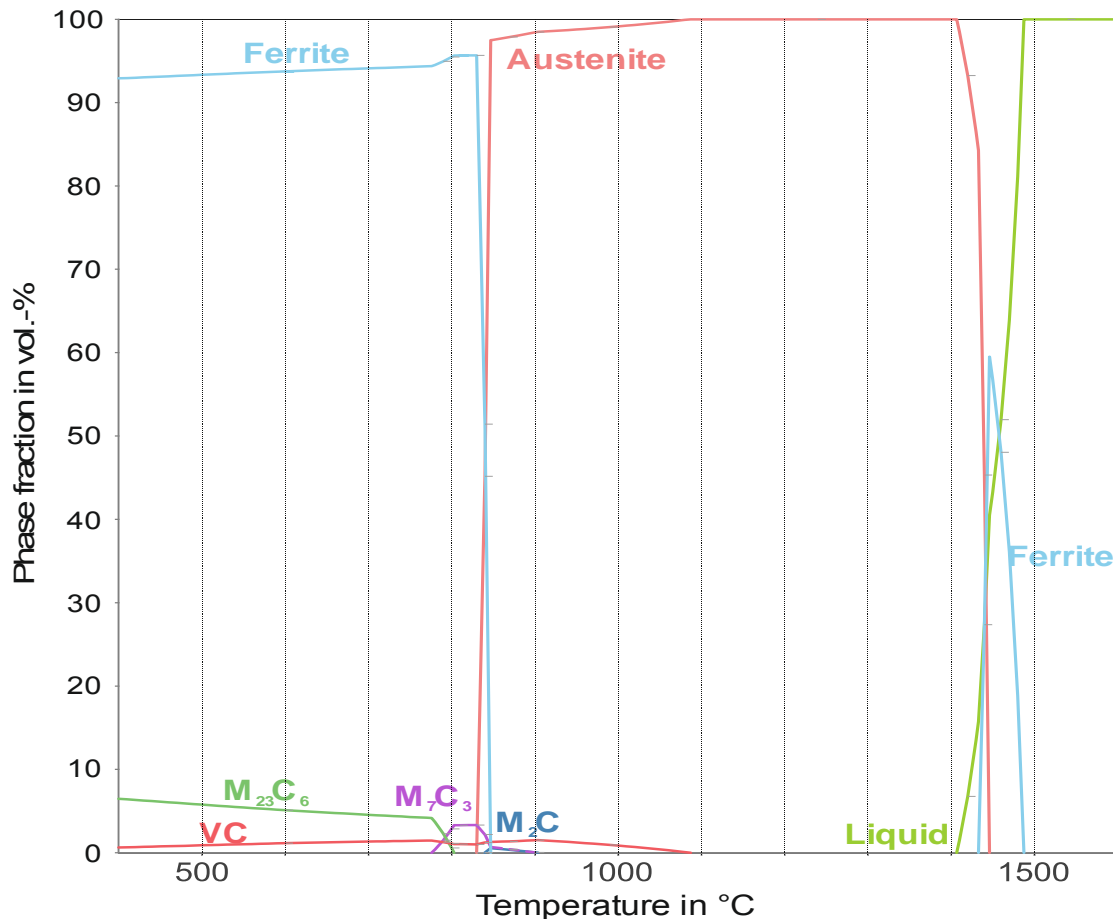


Figure 57: Thermodynamic calculation of the phase content as a function of the temperature in vacuum atmosphere of the X40

4 Discussion

First of all the powder particle surface in the as-received state will be discussed. The SEM studies show that the X40 powder is spherically shaped which is typical for gas-atomized steel powder [8]. No metallic element could be found in the metallic state on the as-received surface, which implies that the powder surface is covered completely by a continuous oxide layer. After a few nanometers of argon ion etching the fraction of the metallic state increases strongly for iron and after 20 nm of etching iron is completely metallic. Since the other elements do not show the same trend, it can be concluded that iron forms a thin homogeneous oxide layer on the powder surface. The thickness has been determined to be about 7 nm. This is quite thick for inert gas atomized steel powder and can be explained by improper storage over a long period of time without protective atmosphere. After 7.5 nm of etching the iron cation concentration decreases strongly. This can be explained by the removal of homogeneous iron oxide layer and so chromium cations increase at this depth. In fact, chromium also shows a steep increase of the metallic state, even though a little bit weaker compared to iron. However, it cannot be concluded that it also forms a chromium oxide layer. If there would be a continuous chromium oxide layer no metallic iron signal could be detected. Hence, there is a free metallic matrix with distributes chromium, manganese and vanadium oxide particulates.

Vanadium shows a change in the chemical state with increasing etch depth, but the binding energy is still too high to indicate a metallic state. Besides that, vanadium oxide is very sensitive to ion etching [38]. That means that it transforms to lower oxidation states when being etched. Thus, the implied change in the chemical state must not only have a real chemical meaning but is also a secondary effect of the ion etching. Molybdenum does not play an important role in the oxide formation and is depleted on the surface. This was also shown in studies of Karlsson [12] and Danninger et al. [42, 43].

On top of the oxides a contamination layer can be found. It is indicated by a large amount of carbon, assuming presence of absorbed species. Also the oxygen peak shows a shoulder which corresponds to the present of oxygen in hydroxides. Besides that, the sulfur S 2p peak shifts strongly after 1 nm of etching from about 169 eV to 162 eV. The higher binding energy corresponds to sulfur in the SO_4^{2-} group and the lower one to some sulfides. But it cannot be concluded if there is a contamination layer with SO_4^{2-} and underneath sulfides or if the shift is due to the influence of ion etching [19]. Manganese is also enriched on the surface and both elements mainly disappear after 10 nm of etching. Hence, presence of a monolayer formed by MnS sulfide can be assumed, covering the powder surface. Because it is very thin, the oxide layer underneath the contamination layer can also be measured in the as-received state. Such a contamination layer is typical for atomized metal powders.

The SEM studies confirm the observations by XPS. The iron oxide layer cannot be found due to its small thickness compared to the large interaction area of the electron beam with the powder material, but different kinds of particulates could be observed.

Heat treatment of the X40 powder in an UHV furnace leads to significant changes in the powder surface composition. However, the differences after annealing at 500 °C are rather small compared to the as-received state. Chromium, silicon and vanadium are enriched on the surface. A slight difference compared to the as-received state can also be seen in SEM studies as very few small rectangular particulates appear.

After annealing at 600 °C the surface appearance changed considerably. The rectangular particulates appear all over the powder particle surface especially in the interdendritic areas, where the content of elements with strong oxide affinity as vanadium and chromium is higher. Taking the XPS results into account it becomes clear that they must be chromium rich oxides, due to the fact that the chromium content is strongly increased on the surface and still in the oxidic state. Simultaneously, the iron oxide is mainly reduced indicating that probably it acted as the source of oxygen during heat-treatment to form the chromium oxides. This is also proved by the fact that the oxygen content stays on the same level on the outermost surface. The oxides do not only cover a big area on the surface, they also grow in size as can be seen by the chemical state of chromium, since it is not fully metallic any more after 50 nm of etching. The fraction of metallic manganese is also lower in etch depths over 10 nm compared to the state after annealing at 500 °C. Thus, the iron oxide layer is reduced in favor of more stable chromium and manganese oxides. The metallic part of chromium that can be measured is probably a signal from chromium in the steel matrix that is free of oxides now. Vanadium shows a shift in the binding energy to lower energies. According to vanadium oxide studies of Hryha et al. [38], vanadium undergoes a stepwise reduction process from $V_2O_5 \rightarrow VO_2 \rightarrow V_2O_3 \rightarrow VO \rightarrow V$. The binding energies of 515.95 eV and 515.5 eV are related to the presence of vanadium in VO_2 and V_2O_3 .

The content of chromium on the powder surface is decreased after annealing at 700 °C. In return, the content of manganese increases, accompanied by an increase of sulfur on the outermost surface. Probably sulfur and manganese form manganese sulfide (MnS). The binding energy of manganese Mn 2p_{3/2} in MnS is at 640.9 eV [44] and thus overlaps with the peak of manganese in the oxidic state. But the S 2p was found at about 161.9 eV, which is in good accordance with values in literature for sulfur in MnS at 162.1 eV.

At larger etch depths manganese is still in oxidic state. The same is valid for the signal of silicon which increased after annealing at 700 °C and was found in the Si^{4+} state. Manganese and silicon are known to form stable Mn-Si-oxides [14, 45]. But no information about the binding energy for this type of oxide could be found.

Still, also a lot of chromium is present on the powder surface, assuming formation of

spinel with manganese of the type MnCr_2O_4 . According to the literature, a small satellite peak around 647 eV is visible if this spinel is present [46], which indeed could be found here and thus indicate the presence of MnCr_2O_4 spinels after annealing at 700 °C. Furthermore does the appearance of the particulates change to a more spherical shape, which is also an indication for a transformation of the oxide type.

The V 2p_{3/2} peak is composed of at least two peaks. The second one appears at lower binding energies at 513.2 eV. There are two possible chemical compounds associated to that energy. Firstly, there is a further reduced state of vanadium oxides (VO). According to [19] its binding energy is 512.7 eV for the V 2p_{3/2} peak. Secondly, there is VC which has a binding energy of 513.5 eV [41]. A hint which is the case here can give a look on the narrow scans of carbon. The carbon C 1s peak is composed of two peaks after annealing at 700 °C. The minor peak is located at about 282.8 eV which is quite close to 282.5 eV for carbon in VC carbides measured by Antonik et al. [41]. In multicomponent alloys carbides are never pure, which also shifts the binding energies slightly. This might also be the case here. However, most probably the measured V 2p signal is an overlap of both, VO and VC, and one growing on another. Formation of VO on top of VC has been investigated before [47]. According to reaction calculations performed with HSC Chemistry 7.0 the Gibbs energy ΔG is positive for the reaction



below 1100 °C. Even if the values for ΔG are quite low for the temperatures from 700 °C to 1000 °C the reaction is still not possible from the thermodynamical point of view. However, the equilibrium constant K has a calculated value of $1.238 \cdot 10^{-3}$ for the reaction at 700 °C. According to equation (2.5) this corresponds to a CO partial pressure of $1.238 \cdot 10^{-3}$ bar, which is rather high and possible to reach under the applied conditions. For higher temperatures than 800 °C the partial CO pressure even increases and thus the reaction is getting more likely. The exact calculated values can be found in table 13 in the appendix. Hence, transformation from vanadium oxide VO to vanadium carbides VC is very probable.

Another possible explanation for the shift of the C 1s peak is formation of chromium-rich carbides on the surface. According to the thermodynamic calculations by Thermo-Calc, the type M_{23}C_6 (M stands for metal) is stable at 700 °C. No information about this type could be found, but about the type M_7C_3 , which is favored at 800 °C and above. The signal of the chromium Cr 2p_{3/2} is located at 574.5 eV in Cr_7C_3 and at 574.1 eV in $(\text{Fe,Cr})_7\text{C}_3$. This overlaps with the peak of metallic chromium at 574.3 eV [48]. Thus, information about the carbides is difficult to derive from the chromium signal. But the C 1s peak is located at 283.0 eV for Cr_7C_3 , respectively 283.3 eV for $(\text{Fe,Cr})_7\text{C}_3$. Hence, it is very likely that the

measured carbon peak is composed of both, carbon in vanadium carbide and chromium-rich $M_{23}C_6$, respectively M_7C_3 .

The decrease of the oxygen content on the powder surface after annealing at 800 °C is very distinctive. Simultaneously the content of chromium and manganese decreases strongly, indicating a decrease of chromium and manganese oxides. Manganese has a comparatively high vapor pressure and the vacuum level in the furnace was ultra-high. Thermodynamic calculations and experimental findings of high alloyed Fe-19Mn-18Cr-C-N steels showed a large sublimation of manganese for temperatures above 700 °C in the same experimental set-up as used for this work [14]. Thus, it can be concluded that the same effect occurs for the steel investigated here. The sublimation was not verifiable in the RGA measurement for the X40, but this is not remarkable as manganese is just a trace element and thus the signal might be not strong enough. However, for the Fe-19Mn-18Cr-C-N manganese sublimation has also been observed in RGA in former works [49]. 34 % of chromium on the outermost surface is in the metallic state which shows a reduction of chromium oxides. First reduction processes indicated by RGA start around 800 °C, but a first decent peak cannot be seen before 911 °C. In the TGA the onset of weight loss starts around 1023 °C. But different oxygen partial pressures in each experiment have to be considered. In the furnace attached to the XPS the vacuum pressure was about 10^{-7} mbar, whereas the pressure for the RGA analysis was $<10^{-4}$ mbar and the TGA analysis was performed in flowing argon atmosphere. This means that the temperature intervals of each experiment where the reduction occurs cannot be compared exactly. But it is known that the lower the oxygen partial pressure the lower is the temperature needed to reduce oxides (see figure 4). Hence, in the XPS the oxide reduction must start at much lower temperatures compared to RGA and TGA for the chosen conditions.

Oxide reduction is also visible in the SEM pictures. The surface looks rather clean after annealing at 800 °C. Besides a very few bright particulates, the main particulates found on the surface appeared darker and the EDX measurements showed that they are rich in vanadium. Due to the low oxygen content measured, they are probably vanadium carbides. The peak shifts of V 2p and C 1s to lower binding energies are even more pronounced after annealing at 800 °C, which suggests formation of VC carbides. Additionally, very small particulates were seen in the SEM. The CALPHAD calculations indicate the present of chromium-rich M_7C_3 carbides. But due to their small size this could not be proved by EDX.

In the DTA-plot an endothermic reaction can be seen at 765 °C and a second one at 859 °C. Exactly at the same temperature interval of the second peak a pronounced and rapid shrinkage can be seen in the dilatometry plot. Considering this it can be concluded that the second endothermic peak is related to the transformation of ferrite to austenite, since the face-centered cubic (fcc) crystal lattice of austenite has a denser atomic packing compared to the body-centered cubic (bcc) crystal lattice of the ferrite [4]. The

transformation from ferrite to austenite is also in compliance to the transformation calculated with CALPHAD. There are two possible explanations for the first endothermic peak: The first one is the already shown formation of VC carbides. The as-received powder of the steel grade X34CrMoCo3-3-3 was investigated by synchrotron radiation in [50]. It is shown that the as-received powder consists mainly of martensite and some retained austenite. But no carbides were found. It is very likely that it is the same case for the X40 powder due to the comparable chemical composition. Some segregation was found in the cross-sections of the X40 powder but no clearly visible carbides. Thus, the carbide precipitation must take place during the heat treatment. But due to the high affinity of vanadium to carbon, the precipitation should start at lower temperatures [4]. This is also indicated by the CALPHAD calculations. Therefore, it is likely that the VC precipitation starts at lower temperatures and cannot be seen in the DTA, probably because the heat effect is too low. On the other hand, the VC precipitation on the powder particle surface takes place somewhere between 600 °C and 800 °C. Hence, when the oxide reduction takes place the vanadium carbide formation is also enabled on the surface. The thermodynamic calculations with CALPHAD show that between 780 °C and 810 °C the chromium rich $M_{23}C_6$ carbides transform into carbides of the type M_7C_3 . This consists very well to the first measured DTA peak. The $M_{23}C_6$ carbides form also at low temperatures and were probably also not detectable in the DTA plot.

Annealing at 900 °C leads to a mostly oxide free surface indicated by the low oxygen content and the metallic state of iron and chromium. Manganese and silicon cannot be detected anymore. Thus, most of the oxides are reduced and the surface is quite clean. These reduction processes can be related to the peaks seen in the TGA measurements and the first double peak of CO in the RGA measurements. These peaks appear at higher temperatures as 900 °C, but this can be explained by the different vacuum conditions as mentioned above. The TGA measurements show a pronounced weight loss of the powder which is related to the formation and emission of mainly CO gas measured in RGA, which indicates direct carbothermal reduction processes taking place. The measurements show that the reduction process is divided into two steps, meaning either two different kinds of oxides get reduced at different temperature intervals or one peak is related to the reduction of surface oxides and the other one to reduction of inner oxides.

Amongst other things the degassing behavior of different powder particle sizes of plain carbon steel Fe-0.5% C was studied in [43]. It was shown that the finer the particle size the more pronounced is the first peak and it is shifted to slightly higher temperatures. This can be explained by the larger surface area of finer powder, leading to larger content of iron oxides in the iron oxide layer. Exactly the same degassing behavior was found for the different powder size fractions of the powder studied here in the TGA measurements. This leads to the conclusion that the oxide reduction on the surface occurs in two steps and the second reduction peak is related to inner oxides and thermodynamically stable surface

oxides on the powder surface. Considering this discovery it can be concluded that also the vanadium oxides are probably reduced, respectively transformed to vanadium carbides. Chromium-rich carbides were not found, which is in accordance with the CALPHAD calculations, since only a very low amount is stable at this temperature.

Remarkable is the high sulfur content on the surface after annealing at 900 °C. It is still found in the S^{2-} state, indicating its present in sulfides. To investigate the thermochemical stability of possible sulfide compounds, Ellingham diagrams were calculated with the software HSC Chemistry 7.0. In figure 58 a plot of the most stable sulfides for each metal is shown. The lower the Gibbs energy ΔG the more stable is a compound.

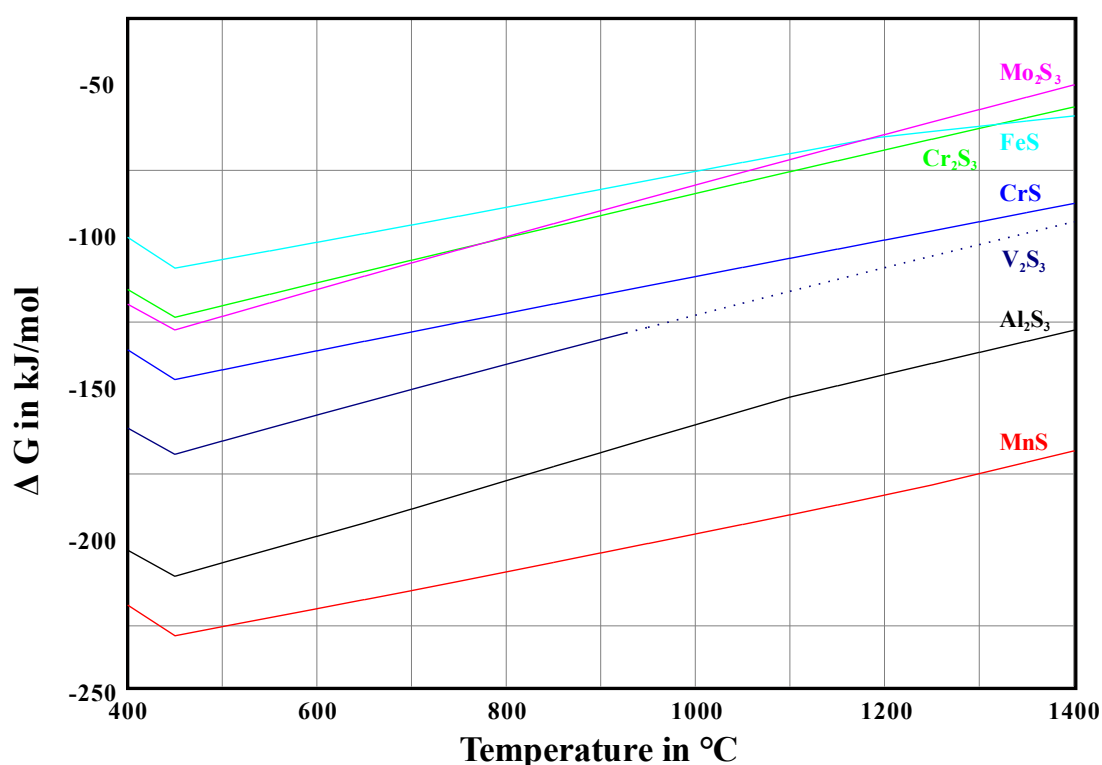


Figure 58: Ellingham diagram of the most stable iron, chromium, molybdenum, vanadium, aluminum and manganese sulfides, calculated with HSC Chemistry 7.0; dashed line means the values are extrapolated

Hence, manganese sulfide (MnS) is by far the most stable possible sulfide. However, since manganese is not present anymore after annealing at 900 °C, manganese sulfides are not a reasonable explanation for strong enrichment of over 8 at.-% sulfur on the outermost surface. Aluminum sulfides (Al₂S₃) are the second most stable possible sulfide. But the Al 2s peak was found at 120.9 eV. According to [51] its binding energy for Al₂S₃ is located at 119.8 eV. Furthermore, the appearance of aluminum seems to be related to aluminum nitrides as will be shown later and sulfur was not found in the EDX analysis of the aluminum particulates after annealing at 1000 °C. Vanadium sulfide (V₂S₃) is the third most stable possible compound. But vanadium is not enriched on the surface after annealing at 900 °C. This does not mean that no V₂S₃ is formed at all, but it can also not explain the strong enrichment of sulfur. The existence of V₂S₃ could not be proved by XPS

because no information about the binding energies could be found. Besides sulfur, chromium is strongly enriched on the surface and after slightly ion etching the content of both elements decreases extensively and CrS is the third most stable sulfide according to the thermochemical calculations. Only information about the binding energy of Cr_2S_3 could be found. This compound is also stable according to the calculations but has a higher Gibbs energy than CrS. The binding energy of the Cr 2p_{3/2} peak in chromium sulfite (Cr_2S_3) is located at 575.6 eV for [52]. This binding energy overlaps with the oxidic peak of chromium, but no shoulder can be seen in this peaks. The S 2p peak in Cr_2S_3 is located at 162.7 eV which agrees very well with the peak at higher energies in the sulfur spectra.

In the end it cannot finally be concluded which compound sulfur forms on the powder particle surface. The presence of a double peak indicates sulfur being present in two different chemical states and thus maybe two different compounds. Since it is strongly enriched on the surface and its content decreases to $\frac{1}{4}$ after slight ion etching, it is very likely that it forms a thin sulfide layer on the powder surface. Furthermore, no particulates rich in sulfide have been found in the EDX studies.

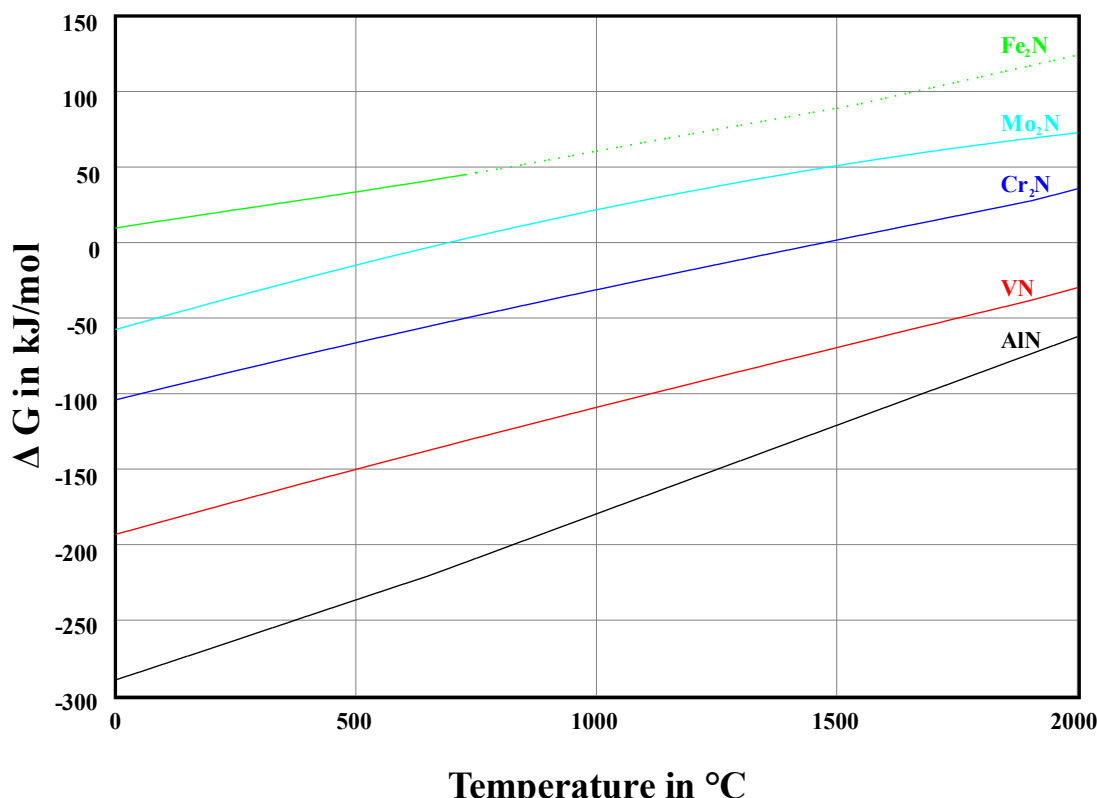


Figure 59: Ellingham diagram of the most stable iron, chromium, molybdenum, vanadium and aluminum nitrides, calculated with HSC Chemistry 7.0; dashed line means the values are extrapolated

Annealing at 1000°C leads to the formation of aluminum- rich particulates on the powder surface. In addition, the content of nitrogen is strongly increased. The Ellingham diagram for possible nitride compounds shows the high stability of AlN (see figure 59).

Questionable is the source of origin of aluminum. The shape of the particulates indicates that they grow out of the powder particle itself. The initial content of aluminum in the powder is not known, so this hypothesis cannot be validated. The second possible source can be the heating element used in the UHV furnace. It is made of the material “Kanthal A-1” which is a FeCrAl-alloy. But no such contaminations when using this filament have been observed before.

The RGA plot shows evolution of N₂ gas for temperatures above 1100 °C. The measured nitrogen peak N 1s is located at 397.6 eV for elevated temperatures. Thermodynamic calculations with CALPHAD showed that nitrogen is bound in VC when no aluminum is present and form vanadium carbonitrides. No information about the binding energy of nitrogen in that kind of compound could be found, but in vanadium nitride (VN) it is at about 397.3 eV [53] and thus also indicates that nitrogen is present in the vanadium carbonitrides. Since the solubility of nitrogen in steels is rather low it forms N₂ and evaporates when the nitrides dissolve [54].

Finally, the feasibility of vacuum annealing of X40 powder will be discussed. As the formation of sintering necks takes place at contact points of plain metallic surfaces, previous reduction of the oxide layer covering the powder particle surface is mandatory to achieve a good metallic bonding between the powder particles. It was shown in this work that the powder particles are covered by a heterogeneous oxide in the as-received state. This leads to a weakening of the former inter-particle boundaries after HIP processing if no previous heat treatment was performed, as previous studies showed [1, 2]. As soon as diffusion is enabled at elevated temperatures, a progressive mass transport of strong oxide forming elements occurs towards the powder particle surface and leads to a growth of more stable oxides, e.g. MnCr₂O₄ spinels. These in turn means transformation of the iron oxide layer and leads to a main reduction of iron after annealing for 1h at 600 °C and a complete reduction after annealing at 700 °C. However, the oxide particulates are homogenously distributed and cover big parts of the powder surface and thus will be enclosed inside the sintering necks if the material would be sintered in this condition. Finally they would remain in the sintered material and eventually weaken it. Consequently, an annealing temperature above 700 °C, depending on the vacuum quality, is necessary to reduce the Cr-Mn oxides as well.

The Cr-Mn and partly vanadium oxides are reduced after annealing at 900 °C which leads to a rather clean powder surface. Vanadium rich carbides can be found on the surface, but they are not supposed to have a negative effect. They are rather needed to improve the wear

resistance and restrict grain growth during sintering and heat treatment of the final product. Furthermore, they are not enriched on the surface as the XPS depth profiling showed. But chromium and sulfur are still enriched on the powder particle surface. Sulfur is often added to steels to improve the machinability but it is supposed to form MnS [4]. No information about the influence of chromium sulfides on the mechanical properties of steels could be found. Questionable is if enough manganese is left in the powder bulk to form MnS during the processing subsequent to the vacuum annealing. However, probably the sulfide layer forms particulates during subsequent processing steps as it has been observed for MnS [55] and thus it has no detrimental effect on the mechanical properties. Besides the loss of Mn, also a loss of carbon occurs, due to the carbothermal reduction forming CO / CO₂. The loss of carbon has significant effect on changes of the mechanical properties of tool steels and has to be taken into account when performing vacuum annealing of the X40 powder. To summarize, vacuum annealing of the X40 powder before sintering or HIP processing seems to be feasible if the loss of carbon is considered.

5 Conclusion and future work

In this thesis the as-received surface and changes in the surface chemistry during vacuum heat treatment of the powder metallurgical Hot Work Tool Steel X40CrMoV5-1 were investigated.

The results show that the as-received surface is completely covered by a heterogeneous oxide layer, composed by a homogeneous 7 nm thin iron oxide layer and particulate oxides rich in chromium, manganese, silicon and vanadium. Larger particulates appear during annealing mainly in the interdendritic areas, which are enriched in alloying elements due to segregation. During vacuum annealing the powder particle surface undergoes considerable changes. Annealing at 600 °C reduces main parts of the iron oxide layer. However, this leads to growth of rectangular shaped, chromium-rich oxides with sizes of about 200 nm all over the powder surface. The type of oxides changes to Cr-Mn-oxides by annealing at 700 °C. The chromium and manganese oxides can be reduced by annealing at 900 °C, leading to an oxide free surface probably covered by a sulfide layer, which growth with increasing annealing temperature. Vanadium oxides undergo several transformations with increasing annealing temperature. Also a transformation to vanadium carbides is indicated to start around 700 °C.

Based on the results obtained it can be concluded that vacuum annealing of the X40 powder before consolidation seems to be feasible to reduce surface oxides and thus improve the metallic bonding between the powder particles during subsequent consolidation. But loss of carbon and manganese during annealing has to be considered.

The next step to establish powder metallurgy as a way of production for Hot Work Tool Steels is mechanical testing on consolidated material to show if the oxide reduction leads to an improvement in the mechanical properties. For HWS toughness, impact energy and wear resistance are the key factors for high durability. As wear resistance should not be so much affected by previous oxide reduction, tests can focus on toughness and impact work, i.e. tensile and notch impact tests. Subsequent fractography can give clues about fracture behavior and information concerning presence oxide phases, their composition and distribution on the former inter-particle boundaries.

For the vacuum annealing it has to be taken into account that the majority of industrial furnaces have a lower vacuum level than the ultra-high vacuum applied in this work and thus oxide reduction is shifted to higher temperatures. The loss of carbon can be compensated by either using powder with higher carbon content or by admixing graphite powder to the steel powder.

Concerning the surface chemistry of the investigated steel powder, there are still some questions open. The chemical composition of the oxide particulates could not be conclusively determined by EDX due to their small size. These could be evaluated by Auger Electron Spectroscopy (AES), since it has a considerably better lateral resolution (up to 12 nm) compared to XPS and significantly smaller information volume (couple of nanometers) compared to EDX.

The influence of sulfur on the surface chemistry could also not be clarified due to a lack of information about the binding energies of sulfides. However, sintering experiments do not show any influence of sulfur segregation on the sintering process and resulting mechanical properties.

To determine the origin of the aluminum particulates after annealing at 1000 °C, two factors have to be checked. First of all – the aluminum content in the base powder has to be measured by chemical analysis as this data is not available for the produced powder. Secondly, possibility of contamination of the powder by aluminum during vacuum annealing has to be checked.

References

- [1] T. Schneiders, Neue pulvermetallurgische Werkzeugstähle, Ph.D. Thesis, Ruhr-University Bochum, 2005.
- [2] F. Wendl, Einfluss der Fertigung auf Gefüge und Zähigkeit von Warmarbeitsstählen mit 5% Chrom, Ph.D Thesis, Ruhr-University Bochum: VDI-Verlag, Volume 5, No. 91, 1985.
- [3] R. German, Powder Metallurgy Science, Princeton: Metal Powder Industries Federation, 1994.
- [4] H. Berns and W. Theisen, Ferrous Materials - Steel and Cast Iron, Springer-Verlag, 2008.
- [5] R. German, Powder metallurgy and particulate materials processing: The processes, materials, products, properties and applications, Metal Powder Industries Federation, 2005.
- [6] Deutsches Institut für Normung e.V. (DIN), ISO 4957 - Tool Steels, Beuth-Verlag, 2001.
- [7] D. Broek, Elementary Engineering Fracture Mechanics, Delft University of Technology, Netherlands: Noordhoff International Publishing, 1974.
- [8] W. Schatt und K.-P. Wieters, Powder metallurgy: processing and materials, Shrewsbury, U.K.: European Metallurgy Association, 1997.
- [9] A. Weddeling, Surface Analysis of Austenitic Fe-18Cr-19Mn-C-N Powder, Bachelor Thesis, Chalmers University of Technology, Gothenburg, Sweden, 2011.
- [10] M. Hansen und K. Anderko, Constitution of binary alloys, New-York: McGraw-Hill, 1958.
- [11] W. Schatt, Sintervorgänge: Grundlagen, Düsseldorf: VDI-Verlag, 1992.
- [12] D. Stöver, Pulvermetallurgie, Ruhr-University Bochum: Script, 2010.

- [13] A. Weddeling, K. Zumsande, E. Hryha, S. Huth, L. Nyborg und S. Weber, „Characterization of High-Mn-Cr Austenitic Steel Powder Fe-19Mn-18Cr-C-N,“ *EuroPM Barcelona, Proceedings, Vol. 2*, pp. 15-20, 2011.
- [14] K. Zumsande, A. Weddeling, E. Hryha, S. Huth, L. Nyborg, S. Weber, N. Krasokha und W. Theisen, „Characterization of the surface of Fe-19Mn-18Cr-C-N during heat treatment in a high vacuum - An XPS study“.
- [15] P. Beiss, „Sintering atmospheres for PM steels,“ *Höganäs Chair in Powder Metallurgy, Workshop "Sintering Atmospheres"*, 1999.
- [16] D. Gaskell, *Introduction to the Thermodynamics of Materials*, New York: Taylor&Francis Group, 2008.
- [17] E. Hryha, E. Dudrova und L. Nyborg, „On-line control of processing atmospheres for proper sintering of oxidation-sensitive PM steels,“ *Journal of Materials Processing Technology, Vol. 212*, pp. 977-987, 2012.
- [18] D. Chasoglou, „Effect of Sintering Atmosphere on the Transformation of Surface Oxides during Sintering of Chromium Alloyed Steel,“ *Powder Metallurgy Progress, Vol. 9, Nr. 3*, pp. 141-155, 2009.
- [19] E. Hryha, C. Gierl, L. Nyborg, H. Danninger und E. Dudrova, „Surface composition of the steel powders pre-alloyed with manganese,“ *Applied Surface Science Vol. 256, Issue 12*, pp. 3946-3961, 2010.
- [20] E. Bayer und H. Seilstorfer, „Pulvermetallurgisch durch heißisostatisches Pressen hergestellter Warmarbeitsstahl X40 CrMoV5 1,“ *Archiv für Eisenhüttenwesen, Vol. 55, Nr. 4*, pp. 169 - 176, 1984.
- [21] A. Oppenkowski, *Zähigkeit von pulvermetallurgischen Werkzeugstählen und Metal Matrix Composites*, Diploma Thesis, Lehrstuhl Werkstofftechnik, Ruhr-University Bochum, 2007.
- [22] H. Berns, *Hartlegierungen und Hartverbundwerkstoffe*, Berlin: Springer Verlag, 1998.
- [23] Deutsches Institut für Normung (DIN) e.V., *DIN EN 10027-1 - Designation systems for steels*, Berlin: Beuth-Verlag, 2005.
- [24] Deutsches Institut für Normung e.V. (DIN), *DIN ISO 4497 - Metallpulver - Bestimmung der Teilchengrößen durch Trockensiebung*, Berlin: Beuth-Verlag,

1991.

- [25] Deutsches Institut für Normung e.V. (DIN), DIN 66165 - Siebanalyse, Berlin: Beuth-Verlag, 1987.
- [26] J. F. Moulder, W. F. Stickle, P. E. Sobol und K. D. Bomben, Handbook of X-Ray Photoelectron Spectroscopy, Minnesota: Perkin-Elmer Corporation, 1992.
- [27] J. F. Watts und J. Wolstenholme, An introduction to surface analysis in XPS and AES, Chichester: J. Wiley, 2003.
- [28] A. Klein, Grundlagen der Röntgenphotoelektronenspektroskopie, Leibnitz Universität Hannover: Script, 2008.
- [29] L. Reimer, Scanning Electron Microscopy: Physics of Image Formation and Microanalysis, Berlin: Springer-Verlag, 1998.
- [30] J. I. Goldstein, Scanning electron microscopy and x-ray microanalysis: a text for biologists, materials scientists, and geologists, New York: Plenum Press, 1992.
- [31] M. E. Brown, Handbook of Thermal Analysis and Calorimetry - Volume 1: Principles and Practice, Amsterdam: Elsevier Science B.V., 1998.
- [32] N. Krasokha, Einfluss der Sinteratmosphäre auf das Verdichtungsverhalten hochlegierte PM-Stähle, Ph.D Thesis, Ruhr-University Bochum, 2012.
- [33] J.-C. Zhao, Methods for Phase Diagram Determination, Elsevier Science, 2007.
- [34] H. L. Lukas, S. G. Fries und B. Sundman, Computational Thermodynamics: The Calphad Method, New York: Cambridge University Press, 2007.
- [35] N. Saunders und A. P. Miodownik, CALPHAD (Calculation of Phase Diagrams): A Comprehensive Guide, Oxford and New York: Pergamon, 1998.
- [36] S. Pingfang und B. Sundman, TCC Thermo-Calc Software User's Guide Version 3.0, Thermo-Calc Software AB.
- [37] Thermo-Calc Software AB: TCFE6 - TCS Steels/Fe-Alloys Database, Version 6.2.
- [38] E. Hryha, E. Rutquist und L. Nyborg, „Stoichiometric vanadium oxides studied by XPS,“ *Surface and Interface Analysis, Vol. 44*, pp. 1022-1025, 2012.

- [39] L. Nyborg, A. Nylund und I. Olefjord, „Thickness Determination of Oxide Layers on Spherically-shaped Metal Powders by ESCA,“ *Surface and Interface Analysis, Vol. 12*, pp. 110-114, 1988.
- [40] R. Nyholm und N. Mårtensson, „Core level binding energies for the elements Zr-Te ($Z=40-52$),“ *Journal of Physics C: Solid State Physics, Vol. 13*, pp. 279-284, 1980.
- [41] M. Antonik, R. Lad und T. Christensen, „Clean Surface and Oxidation Behavior of Vanadium Carbide, VC0.75(100),“ *Surface and Interface Analysis*, pp. 681-686, 1996.
- [42] H. Danninger, X. Chen und B. Lindquist, „Oxygen Removal during Sintering of Steels Prepared from Cr-Mo and Mo Prealloyed Steels,“ *Materials Science Forum, Vols. 534-536*, pp. 577-580, 2007.
- [43] H. Danninger, C. Gierl, S. Kremel, G. Leitner, K. Jaenicke-Roessler und Y. Yu, „Degassing and Deoxidation Processing during Sintering of unalloyed and alloyed PM Steels,“ *Powder Metallurgy Progress, Vol. 2, No. 3*, pp. 125-140, 2002.
- [44] B. R. Strohmeier und D. M. Hercules, „Surface Spectroscopic Characterization of Mn/Al₂O₃ Catalysts,“ *Journal of Physical Chemie, Vol. 88*, pp. 4922-4929, 1984.
- [45] R. Oro, M. Campos, E. Hryha, L. Nyborg und J. Torralba, „Surface Analysis at Different Sintering Stages of Steel Compacts with Mn and Si,“ *European Powder Metallurgy Association, editor. Proceeding of EuroPM 2011 Congress & Exhibition, Vol. 1*, pp. 113-118, 2011.
- [46] G. Alleen, S. Harris und J. Jutson, „A Study of a Number of mixed Transition Metal Oxide Spinels using X-Ray Photoelectron Spectroscopy,“ *Applied Surface Science, Vol. 37*, pp. 111-134, 1989.
- [47] D. Gozzi, M. Montozzi und P. Cignini, „Oxidation kinetics of refractory carbides at low oxygen partial pressures,“ *Solid State Ionics, Vol 123, Elsevier*, pp. 11-18, 1999.
- [48] M. Detroye, F. Reniers, C. Buess-Hermann und J. Vereecken, „AES–XPS study of chromium carbides and chromium iron carbides,“ *Applied Surface Science*,

Vols. 144-145, pp. 78-82, 1999.

- [49] T. Albayram, „Einfluss der Stickstoffatmosphäre auf das Verdichtungsverhalten von hochlegierten PM-Stählen,“ *Bachelor Thesis, Lehrstuhl Werkstofftechnik, Ruhr-University Bochum, 2012.*
- [50] M. Gras, „Untersuchung des Einflusses der Pulverkorngröße auf die Phasenverteilung gasverdünster Pulver mit Synchrotron-Strahlung,“ *Semesterarbeit, Lehrstuhl Werkstofftechnik, Ruhr-University Bochum, 2012.*
- [51] G. E. McGuire, G. K. Schweitzer und T. A. Carlson, „Stud of Core Electron Binding Energies in Some Group IIIa, Vb, and VIb Compounds,“ *Inorganic Chemistry, Vol. 12, No. 10, pp. 2450 - 2453, 1973.*
- [52] E. Agostinell, C. Battistoni, D. Fiorani, G. Mattocono und M. Nogues, „An XPS Study of the electronic Structure of the $Zn(x)Cd(1-x)Cr_2X_4$ ($X=S,Se$) Spinel System,“ *Journal of Physics and Chemistry of Solids, Vol. 50, No. 3, pp. 269-272, 1989.*
- [53] A. V. Naumkin, A. Kraut-Vass, S. W. Gaarenstroom und C. J. Powell, „NIST X-ray Photoelectron Spectroscopy Database - Database 20, Version 4.1,“ 23 05 2013. [Online]. Available: <http://srdata.nist.gov/xps/>.
- [54] V. G. Gavriljuk und H. Berns, „High Nitrogen Steels - Structure, Properties, Manufacture, Applications,“ *Springer Verlag, 1999.*
- [55] E. Hryha, E. Dudrova und L. Nyborg, „Critical Aspects of Alloying of Sintered Steels with Manganese,“ *Metallurgical and Materials Transactions A, Vol 41A, pp. 2880-2897, 2010.*
- [56] D. Chasoglou, „Surface Interactions During Sintering of Chromium-alloyed PM Steels in Different Atmospheres,“ *Proceeding of World PM 2010: Powder Metallurgy World Congress & Exhibition 2010, pp. 3-12, 2010.*
- [57] X.-R. Yu, F. Liu, Z.-Y. Wang und Y. Chen, „Auger Parameters for Sulfur-containing Compounds using a mixed Aluminum-Silver Excitation Source,“ *Journal of Electron Spectroscopy and Related Phenomena, Vol. 50, pp. 159-166, 1990.*
- [58] K.-H. Schwalbe, „On the influence of Microstructure on Crack Propagation Mechanisms and Fracture Toughness of metallic materials,“ *Engineering Fracture Mechanics, Vol. 9, pp. 795-832, 1977.*

- [59] H. Karlsson, L. Nyborg und O. Bergman, „Surface Interactions during Sintering of Wateratomised Pre-alloyed Steel Powder,“ *Euro PM2004 - Sintered Steels*, pp. 23-28, 2004.
- [60] H. Karlsson, L. Nyborg und S. Berg, „Surface chemical analysis of prealloyed water atomised steel powder, Vol. 48,“ *Powder Metallurgy*, pp. 51-58, 2005.
- [61] D. Chasoglou, Surface Chemical Characteristics of Chromium-alloyed Steel Powder and the Role of Process Parameters during Sintering, Ph.D. Thesis, Chalmers University of Technology, Gothenburg, Sweden, 2012.
- [62] C. Powell, „Recommended Auger parameters for 42 elemental solids,“ *Journal of Electron Spectroscopy and Related Phenomena*, Vol. 185, Nr. 1, pp. 1-3, 2012.

Appendix

A.1 Tables

Table 4: Particle size distribution of the X40

Sieve fraction in μm	<25	25-36	36-63	63-100	100-150	150-200	>200
Wt.-%	3.6	3.2	11.8	48.2	21.3	6.5	5.4

Table 5: Chemical composition of the powder surface of the X40 in the as-received state; powder mounted on aluminum plate

Etch. depth / Element	Fe	Cr	Mo	V	Mn	C	O	S	N
As-received	15.58	0.79	0.23	0.64	2.26	25.13	53.59	1.14	0.63
1 nm	35.76	1.76	0.28	1.02	2.07	5.15	54.26	0.70	0.00
3 nm	37.89	3.43	0.41	1.00	1.66	3.06	51.88	0.67	0.00
4 nm	38.56	4.54	0.46	1.02	1.50	3.45	49.58	0.89	0.00
5 nm	37.38	6.28	0.62	1.01	1.45	4.87	47.26	1.13	0.00
7.5 nm	45.86	7.65	0.89	0.94	1.26	4.74	37.76	0.90	0.00
10 nm	63.17	6.17	1.40	0.79	0.85	4.11	23.39	0.00	0.00
20 nm	75.38	5.45	1.75	0.79	0.43	5.29	10.91	0.00	0.00
50 nm	80.79	5.37	1.7	0.92	0.28	3.74	7.21	0.00	0.00

Table 6: Chemical composition of the powder surface of the X40 in the as-received state; powder mounted on carbon tape

Etch. depth / Element	Fe	Cr	Mo	V	Mn	C	O	S	N
As-received	12.54	0.68	0.26	0.62	2.01	34.84	47.13	1.35	0.57
1 nm	24.86	1.28	0.23	0.77	1.83	24.98	45.51	0.54	0.00
3 nm	32.01	2.65	0.33	0.80	1.50	18.83	43.40	0.48	0.00
4 nm	32.61	3.98	0.45	0.86	1.57	18.13	41.64	0.76	0.00
5 nm	33.83	5.32	0.58	1.01	1.60	16.81	40.10	0.75	0.00
7.5 nm	38.44	6.55	0.93	0.98	1.16	18.49	32.46	0.99	0.00
10 nm	51.90	4.88	1.24	0.70	0.89	20.09	19.70	0.60	0.00
20 nm	60.79	4.53	1.48	0.72	0.36	20.28	11.49	0.34	0.00
50 nm	69.57	4.51	1.30	0.68	0.31	15.15	8.48	0.00	0.00

Table 7: Chemical composition of the powder surface of the X40 after annealing at 500 °C; powder mounted on copper plate

Etch. depth / Element	Fe	Cr	Mo	V	Mn	C	O	S	N	Si
As-annealed	24.36	4.68	0.31	1.78	1.83	15.77	47.42	1.63	0.7	1.51
1 nm	25.22	4.43	0.26	1.65	1.51	14.85	48.42	1.9	0.72	1.04
3 nm	31.21	6.62	0.53	2.28	1.59	4.06	51.92	0.97	0.00	0.82
4 nm	35.19	6.9	0.52	1.91	1.55	3.56	48.5	1.07	0.00	0.79
5 nm	36	8.2	0.73	1.76	1.77	3.69	45.87	1.19	0.00	0.8
7.5 nm	46.16	8.63	1.17	1.79	1.38	3.93	34.73	1.19	0.00	1.02
10 nm	60.92	6.47	1.53	1.48	1.09	5.52	22.21	0.78	0.00	0.00
20 nm	75.28	5.46	1.86	1.43	0.43	5.41	10.13	0.00	0.00	0.00
50 nm	79.51	5.31	1.54	1.27	0.31	5.26	6.81	0.00	0.00	0.00

Table 8: Chemical composition of the powder surface of the X40 after annealing at 600 °C; powder mounted on copper plate

Etch. depth / Element	Fe	Cr	Mo	V	Mn	C	O	S	N	Si
As-annealed	5.60	26.43	0.36	4.08	2.47	9.00	48.20	2.88	0.00	0.99
1 nm	8.20	24.90	0.34	4.48	2.99	3.68	52.95	1.10	0.11	1.25
3 nm	15.58	22.55	0.54	4.12	2.71	3.64	47.87	1.15	0.34	1.52
4 nm	21.52	21.34	0.68	3.81	2.37	3.44	43.79	1.21	0.39	1.44
5 nm	28.59	19.51	0.79	3.39	2.24	3.67	39.72	1.02	0.17	0.92
7.5 nm	45.96	14.88	1.23	2.42	1.46	3.15	29.21	0.63	0.21	0.84
10 nm	57.83	10.64	1.33	1.79	0.99	3.75	22.44	0.38	0.18	0.67
20 nm	72.73	5.79	1.11	0.95	0.59	3.73	14.98	0.00	0.13	0.00
50 nm	77.08	4.87	1.10	1.08	0.29	3.54	12.04	0.00	0.00	0.00

Table 9: Chemical composition of the powder surface of the X40 after annealing at 700 °C; powder mounted on copper plate

Etch. depth / Element	Fe	Cr	Mo	V	Mn	C	O	S	N	Si
As-annealed	3.03	14.18	0.39	4.98	16.92	10.82	42.14	4.16	0.46	2.92
1 nm	3.98	17.20	0.38	5.35	14.31	5.19	47.83	1.63	0.5	3.64
3 nm	9.43	15.70	0.71	6.11	12.3	4.56	44.89	1.09	0.67	4.53
4 nm	14.44	15.26	0.89	5.95	11.18	4.49	41.5	1.03	0.5	4.78
5 nm	19.71	14.37	1.16	6.17	9.94	5.56	37.81	1.15	0.31	3.82
7.5 nm	35.75	12.35	1.71	5.04	7.19	5.71	27.87	0.82	0.29	3.26
10 nm	50.49	10.48	2.02	4.15	4.86	4.99	20.61	0.62	0.2	1.58

20 nm	72.00	6.99	1.74	1.97	2.01	3.50	11.13	0.39	0.00	0.26
50 nm	82.97	5.69	1.24	0.96	0.76	2.46	5.91	0.00	0.00	0.00

Table 10: Chemical composition of the powder surface of the X40 after annealing at 800 °C; powder mounted on copper plate

Etch. depth / Element	Fe	Cr	Mo	V	Mn	C	O	S	N	Si
As-annealed	30.20	11.84	0.55	5.83	7.50	7.19	28.16	4.54	0.81	3.36
1 nm	35.70	11.51	0.73	6.11	6.63	5.34	29.73	1.09	0.84	2.31
3 nm	41.68	10.69	1.04	7.38	4.39	6.24	24.15	0.88	1.06	2.50
4 nm	44.20	9.97	1.25	7.99	3.66	6.29	22.22	0.51	1.24	2.67
5 nm	46.72	9.48	1.38	8.26	3.11	7.83	19.38	0.46	0.90	2.47
7.5 nm	53.93	8.24	1.69	8.60	1.93	7.60	14.75	0.38	1.00	1.88
10 nm	58.97	7.33	1.82	7.88	1.42	8.11	11.91	0.00	0.94	1.62
20 nm	72.41	6.23	1.75	5.73	0.50	6.13	5.90	0.00	0.68	0.66
50 nm	79.73	6.08	1.42	2.71	0.25	4.43	4.68	0.00	0.20	0.50

Table 11: Chemical composition of the powder surface of the X40 after annealing at 900 °C; powder filled in stainless steel container

Etch. depth / Element	Fe	Cr	Mo	V	Mn	C	O	S	N	Si	Al
As-annealed	59.78	9.23	0.89	4.12	0.00	8.68	5.50	8.38	0.32	0.00	3.10
1 nm	66.08	6.24	0.91	4.66	0.00	7.56	8.66	1.95	1.01	0.00	2.94
3 nm	69.41	5.37	0.99	4.67	0.00	7.26	8.82	1.58	0.66	0.00	1.33
4 nm	70.77	5.56	1.18	5.02	0.00	6.66	8.09	1.47	0.50	0.00	0.75
5 nm	72.62	4.95	1.12	4.95	0.00	7.17	8.11	0.99	0.09	0.00	0.00
7.5 nm	72.37	5.40	1.16	4.69	0.00	6.82	8.48	0.55	0.52	0.00	0.00
10 nm	74.07	5.14	1.28	5.04	0.00	6.37	6.84	0.67	0.58	0.00	0.00
20 nm	75.46	4.92	1.41	4.77	0.00	6.23	6.61	0.00	0.60	0.00	0.00
50 nm	77.78	4.80	1.36	3.20	0.00	4.43	7.30	0.00	1.12	0.00	0.00

Table 12: Chemical composition of the powder surface of the X40 after annealing at 1000 °C; powder filled in stainless steel container

Etch. depth / Element	Fe	Cr	Mo	V	Mn	C	O	S	N	Si	Al
As-annealed	58.11	11.02	0.69	2.31	0.00	8.70	2.17	8.46	3.61	0.00	4.93
1 nm	68.14	6.80	0.79	2.22	0.00	6.09	6.88	1.86	2.78	0.00	4.45
3 nm	71.33	5.71	0.8	2.24	0.00	5.18	8.03	0.87	2.65	0.00	3.20
4 nm	72.04	5.27	0.79	2.24	0.00	5.28	8.54	0.78	2.24	0.00	2.82

5 nm	72.64	5.11	0.78	2.45	0.00	4.76	8.96	0.00	2.52	0.00	2.78
7.5 nm	73.16	5.08	0.88	2.42	0.00	4.98	8.4	0.00	2.41	0.00	2.67
10 nm	72.58	5.33	1.04	2.25	0.00	5.01	8.99	0.00	2.59	0.00	2.21
20 nm	73.49	5.25	0.93	2.44	0.00	4.37	8.12	0.00	3.02	0.00	2.39
50 nm	76.31	5.10	1.11	2.34	0.00	3.79	7.61	0.00	2.06	0.00	1.68

Table 13: Calculated state variables for the reaction $\text{VO} + 2\text{C} = \text{VC} + \text{CO}(\text{g})$ with HSC Chemistry 7.0

Temperatur in °C	ΔH in kJ	ΔS in J/K	ΔG in kJ	K
0	220.232	174.120	172.671	9.487E-034
100	220.549	175.202	155.173	1.891E-022
200	219.926	173.759	137.712	6.246E-016
300	218.652	171.332	120.453	1.051E-011
400	216.914	168.546	103.457	9.361E-009
500	214.849	165.691	86.746	1.377E-006
600	212.554	162.901	70.317	6.210E-005
700	210.091	160.232	54.161	1.238E-003
800	207.504	157.702	38.266	1.372E-002
900	204.822	155.314	22.616	9.839E-002
1000	202.072	153.065	7.198	5.066E-001
1100	199.272	150.947	-8.001	2.016E+000
1200	196.428	148.948	-22.995	6.538E+000
1300	193.551	147.059	-37.795	1.799E+001
1400	190.647	145.269	-52.410	4.329E+001

A.2 Figures

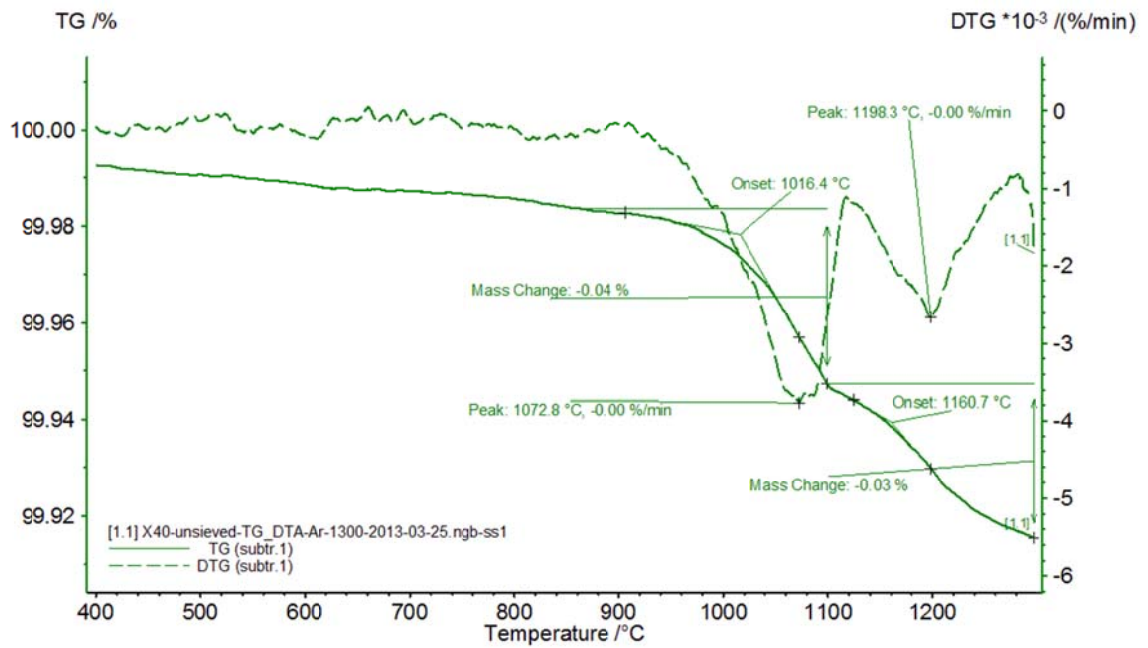


Figure 60: TGA and DTG evaluation of the unsieved powder in flowing argon atmosphere

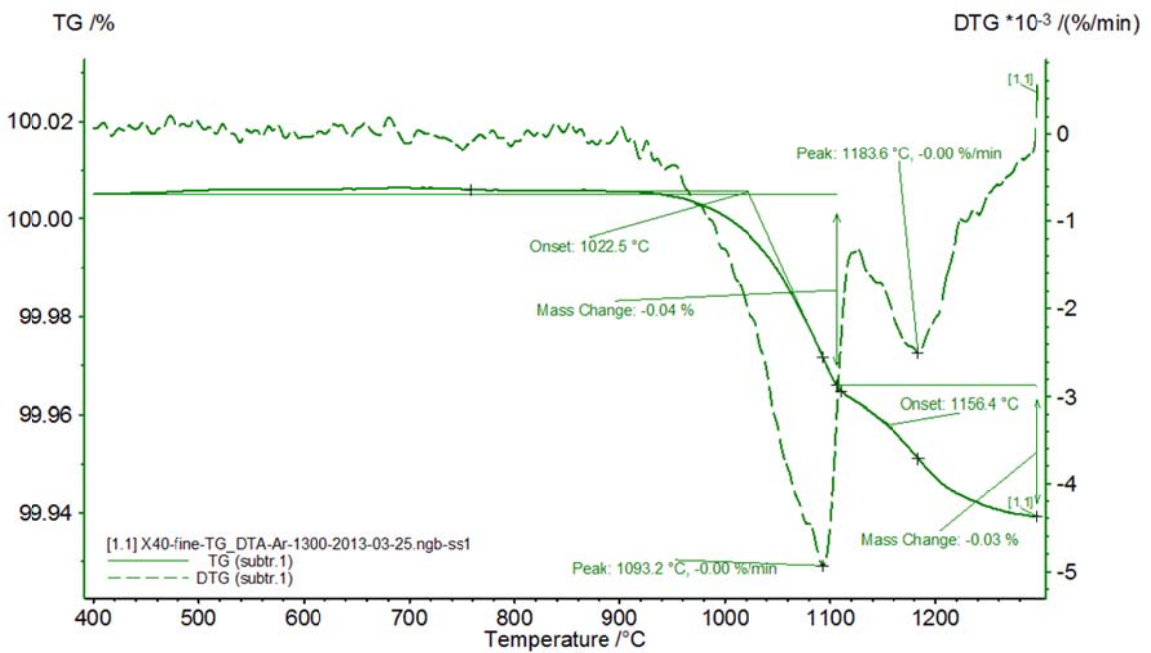


Figure 61: TGA and DTG evaluation of the fine powder fraction (36 - 63 μm) in flowing argon atmosphere

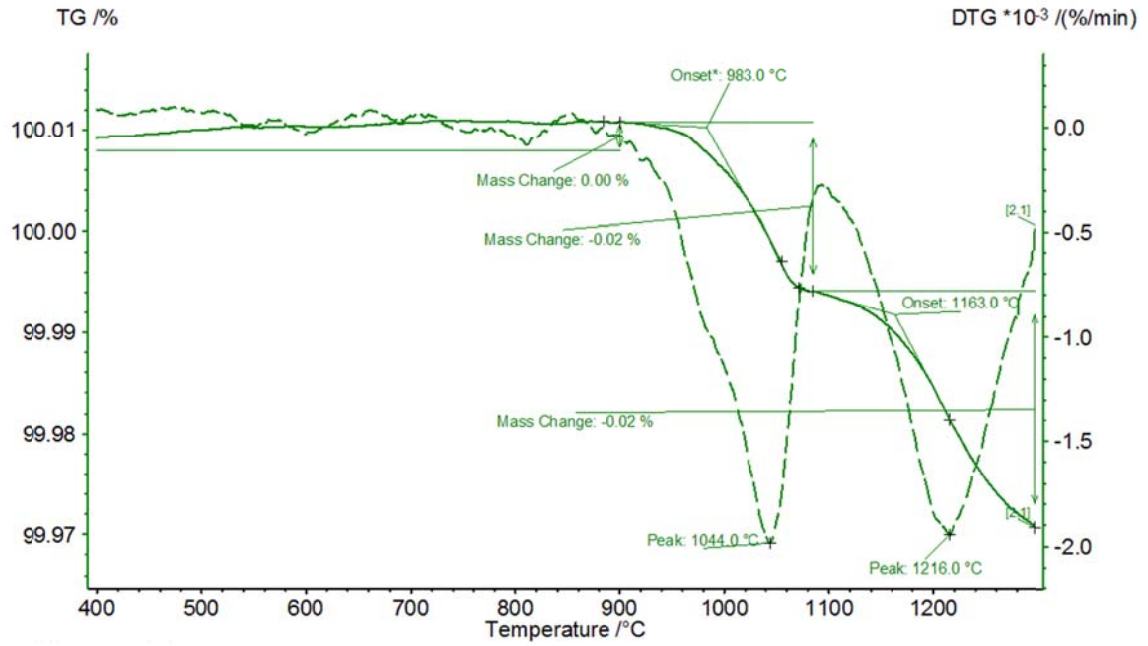


Figure 62: TGA and DTG evaluation of the coarse powder fraction (100 - 150 μm) in flowing argon atmosphere

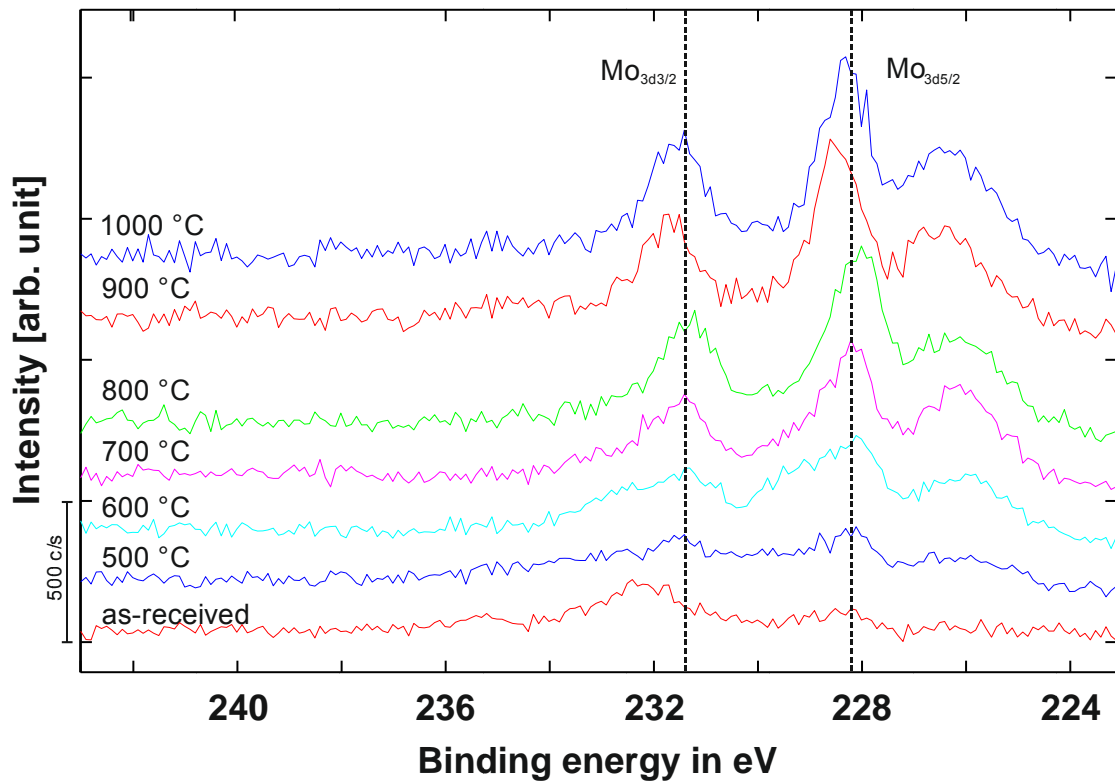


Figure 63: High resolution narrow scan of the molybdenum Mo 3d peak in the as-annealed state at different heat treatment temperatures in vacuum

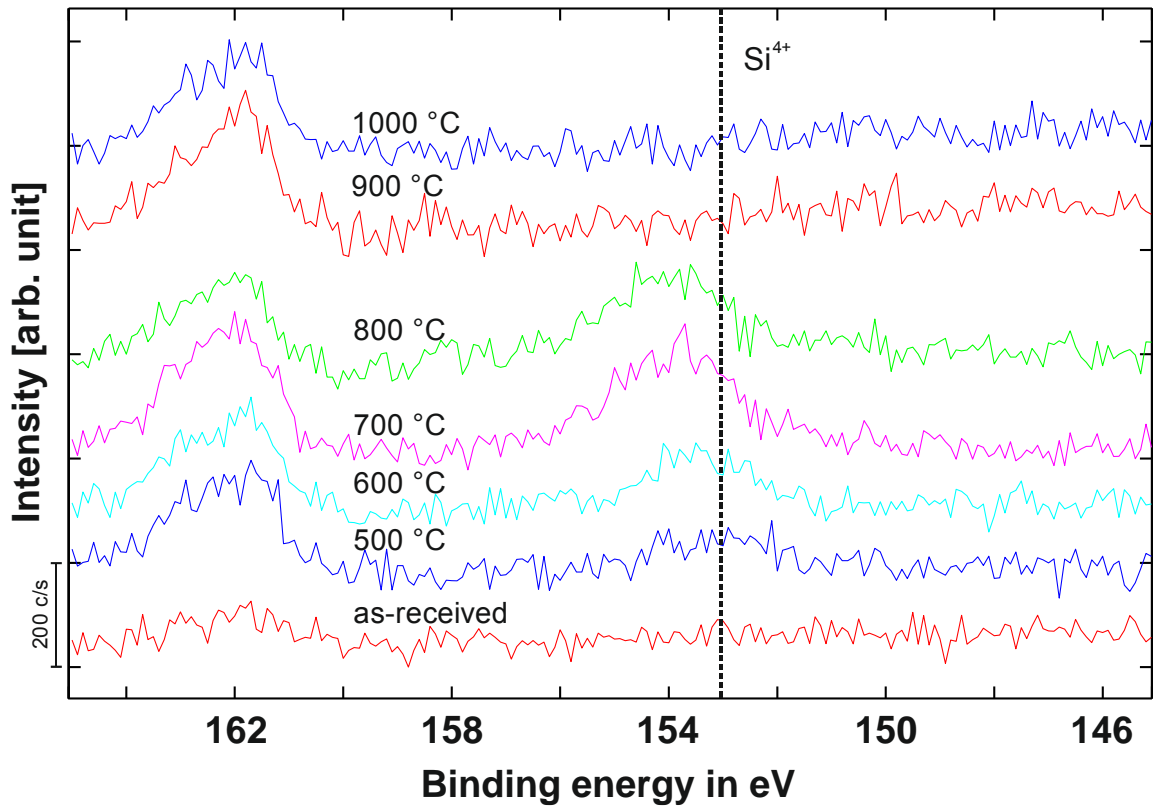


Figure 64: High resolution narrow scan of the silicon Si 2s peak at 1 nm etch depth and different heat treatment temperatures in vacuum

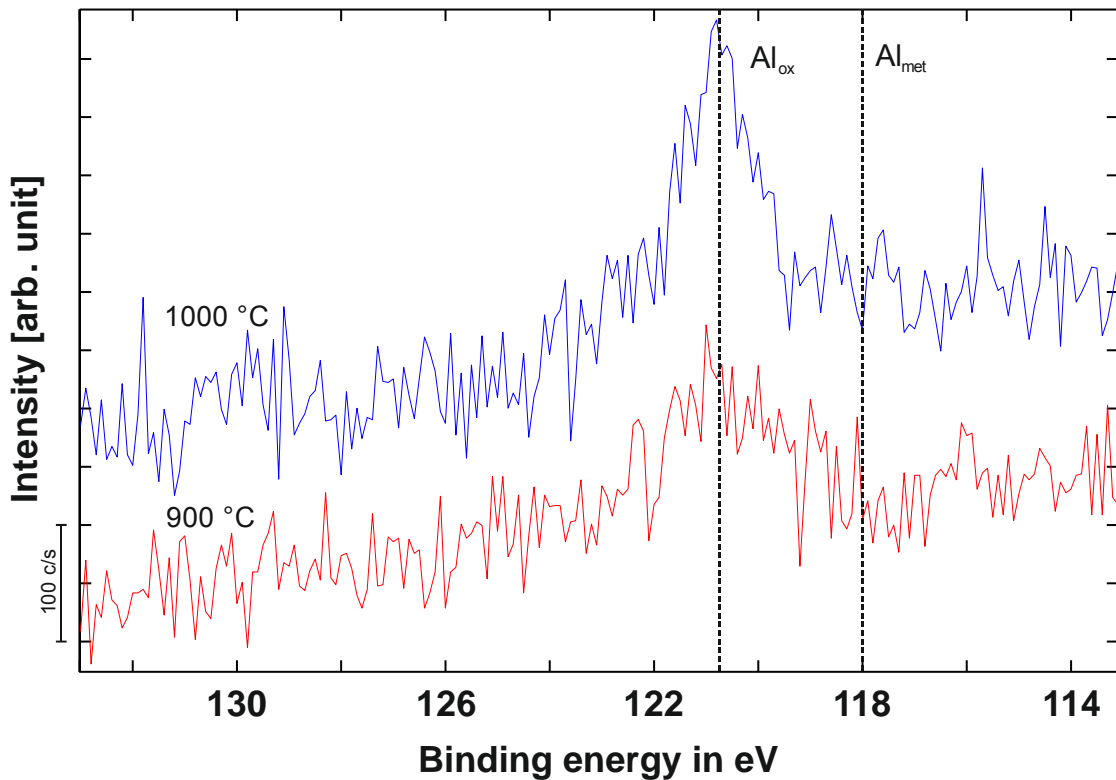


Figure 65: High resolution narrow scan of the aluminum Al 2s peak in as-annealed state at different heat treatment temperatures in vacuum

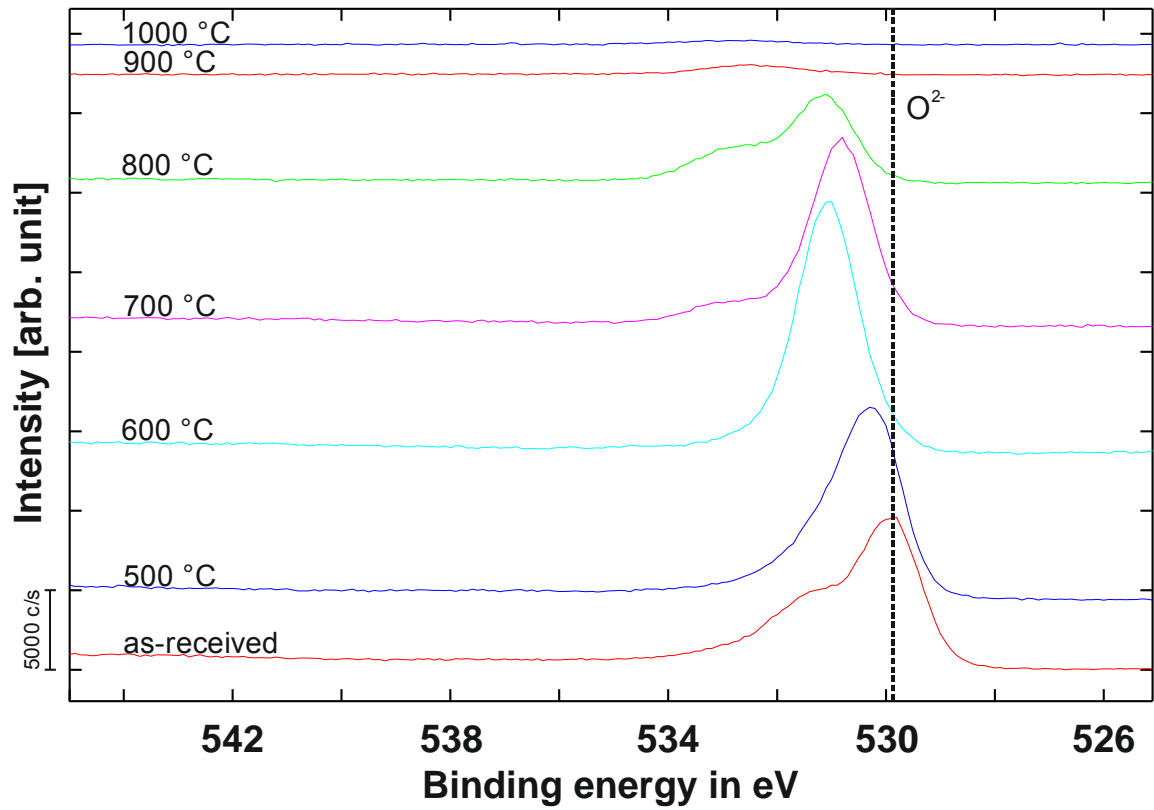


Figure 66: High resolution narrow scan of the oxygen O 1s peak in as-annealed state at different heat treatment temperatures in vacuum